UNIVERSITY OF CALIFORNIA
RIVERSIDE

Spin and Charge Transport in 2D Materials and Magnetic Insulator/Metal Heterostructures

A Dissertation submitted in partial satisfaction
of the requirements for the degree of

Doctor of Philosophy

in

Materials Science & Engineering

by

Walid Amamou

March 2017

Dissertation Committee:
Dr. Ludwig Bartels, Chairperson
Dr. Roland Kawakami
Dr. Jing Shi

The Dissertation of Walid Amamou is approved:

_____

_____

_____

Committee Chairperson

University of California, Riverside

ACKNOWLEDGMENTS

First and foremost, I would like to thank my research advisor Pr. Roland K Kawakami for giving me the opportunity to work on such cutting edge research projects. I learned from you how to become a scientist and how to be a team player in a research environment. You were very supportive from the beginning in every challenge I've faced and had to step up multiple times for me. I am forever grateful. A special thanks to my collaborators at University of Minnesota: Pr. Paul Crowell, Gordon Stecklein and Pr. Steve Koester. It was a privilege for me to work with such remarkable scientists. I learned so much from our biweekly meetings. I also would like to thank the "older" generation that I overlapped with: Adrian Swartz, Wei Han, Kathleen McCreary, Jared Wong, Hua Wen and Pat Odenthal. You were all very helpful and supportive from the beginning.

I am thankful to my lab mates: Igor Pinchuk, Adam Ahmed, Dante O'Hara, Tiancong Zhu, Kelly Yunqiu Luo, Beth Bushong, Jinsong Xu, Michael Newburger, Dongying Wang, Guanzhong Wu, Simranjeet Singh, Jyoti Katoch, Jeremiah van Baren and Takahiro Takeuchi. I very much enjoyed working with all of you and hanging out outside the lab for lunches and drinks. I want to thank my friends at Riverside: Rameez Samnakay, Serol Turkyilmaz, Alfred Jiang and Meir Shachar for the enjoyable days at Riverside. Finally, I am forever indebted to my parents for supporting me throughout my journey. Thank you.

ABSTRACT OF THE DISSERTATION

Spin and Charge Transport in 2D Materials and Magnetic Insulator/Metal Heterostructures

by

Walid Amamou

Doctor of Philosophy, Graduate Program in Materials Science and Engineering
University of California, Riverside, March 2017
Dr. Ludwig Bartels, Chairperson

Spintronic devices are very promising for future information storage, logic operations and computation and have the potential to replace current CMOS technology approaching the scaling limit. In particular, the generation and manipulation of spin current enables the integration of storage and logic within the same circuit for more powerful computing architectures. In this thesis, we examine the manipulation of spins in 2D materials such as graphene and metal/magnetic insulator heterostructures. In particular, we investigate the feasibility for achieving magnetization switching of a nanomagnet using graphene as a nonmagnetic channel material for All Spin Logic Device applications. Using *in-situ* MBE deposition of nanomagnet on graphene spin valve, we demonstrate the presence of an interfacial spin dephasing at the interface between the graphene and the nanomagnet. By introducing a Cu spacer between the nanomagnet and graphene, we demonstrate that this interfacial effect is related to an exchange interaction between the

spin current and the disordered magnetic moment of the nanomagnet in the first monolayer. In addition to the newly discovered interfacial spin relaxation effect, the extracted contact resistance area product of the nanomagnet/graphene interface is relatively high on the order of $1\Omega\mu m^2$. In practice, reducing the contact resistance will be as important as eliminating the interfacial relaxation in order to achieve magnetization switching.

Furthermore, we examine spin manipulation in a nonmagnetic Pt using an internal magnetic exchange field produced by the adjacent magnetic insulator $CoFe_2O_4$ grown by MBE. Here, we report the observation of a strong magnetic proximity effect of Pt deposited on top of a perpendicular magnetic anisotropy (PMA) inverse spinel material Cobalt Ferrite (CFO, $CoFe_2O_4$). The CFO was grown by MBE and its magnetization was characterized by Vibrating Sample Magnetometry (VSM) demonstrating the strong out of plane magnetic anisotropy of this material. The anomalous Hall measurement on a Pt/CFO Hall bar exhibits a strong non-linear background around the saturation of the out of plane CFO magnetization. After subtraction of the Ordinary Hall Effect (OHE), we extract a strongly hysteretic anomalous Hall voltage that indicates that Pt acquired the magnetization properties of the CFO and has become ferromagnetic due to the proximity effects.

TABLE OF CONTENTS

List of Figures

Chapter 1: Introduction

1.1 Spintronics:

Spintronics, also known as spin electronics is a relatively new research field that utilizes the electron's spin degree of freedom in addition to its charge to store information and perform logic operations. The electron spin is a quantum mechanical property that represents the intrinsic angular momentum carried by the electron. Classically, it represents the spinning of the electron around its own axis known as magnetic moment.

Until the discovery of the giant magnetoresistance (GMR) by Albert Fert and Peter Grunberg in the late of 1980 [1, 2], state of the art memory devices relied only on the macroscopic manifestation of a spin, that is the magnetization of a magnetic core, to store information without exploiting the microscopic spin degree of freedom. The integration of the GMR effect in hard disks and read heads greatly increased the density of stored information from 1 to 600 Gbit/in.^{2} in 2007 [3] for which Albert Fert and Peter Grunberg were awarded the 2007 Nobel Prize in Physics. The GMR effect is based on the spin dependent conduction of the electrons inside ferromagnetic thin films.

Before discussing the GMR effect, it is important to introduce the basics of ferromagnetism. Ferromagnetism in metals can be described in the framework of the Stoner-Wohlfarth-Slater model (SWS) proposed in 1948 to explain the measured broken Bohr magneton in ferromagnetic metals [4]. In the simple band model shown in Figure 1.1a, the density of states in 3d ferromagnets are represented by two semi-circles (density of states for an electron gas) for spin up and spin down separated by Δ that corresponds to

the energy of band splitting arising from the exchange interaction. For example in Ni, the exchange splitting Δ = 0.3 eV while for Fe it is 2 eV. The area beneath the Fermi level corresponds to the number of spin up (down) electrons given by $N^{\uparrow(\downarrow)} = \int_{-\infty}^{Ef} N_{\uparrow(\downarrow)} dE$. Given the imbalance of spin up versus spin down, a spontaneous magnetization emerges due to the difference in the density of states and is given by $M = \mu_b (N_\uparrow - N_\downarrow)$.

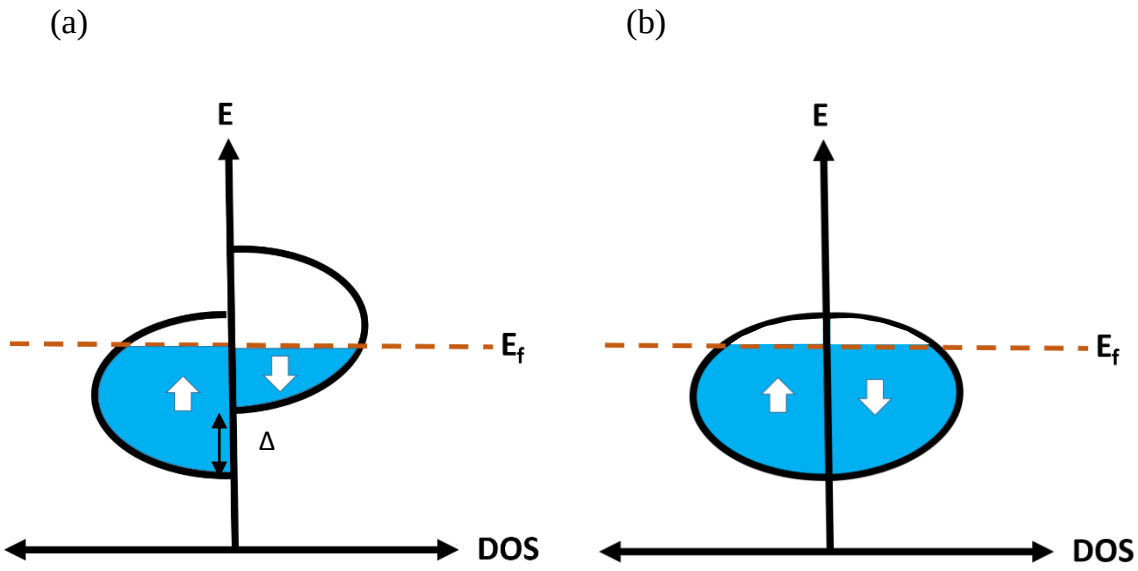

Figure 1.1 Density of states of a ferromagnet (a) showing the spin splitting Δ (b) Density of states of nonmagnetic material

The band splitting is only allowed if and only if the total kinetic (KE) and potential energy (PE) change $\Delta E = \Delta E_{KE} + \Delta E_{PE} < 0$. The exchange integral also known as the Stoner parameter which represents the strength of the exchange electronic correlation is given by: $I = 2\Delta \frac{N}{N_\uparrow - N_\downarrow}$. This magnetic exchange interaction is caused by the overlap of the atomic wave function and is a direct consequence of Pauli exclusion principle. The Stoner

condition is given by I D (E_F) > 1. High density of states at the Fermi level and large exchange interaction are required in order to achieve ferromagnetism. In Figure 1.2 we show I D (E_F) for several materials.

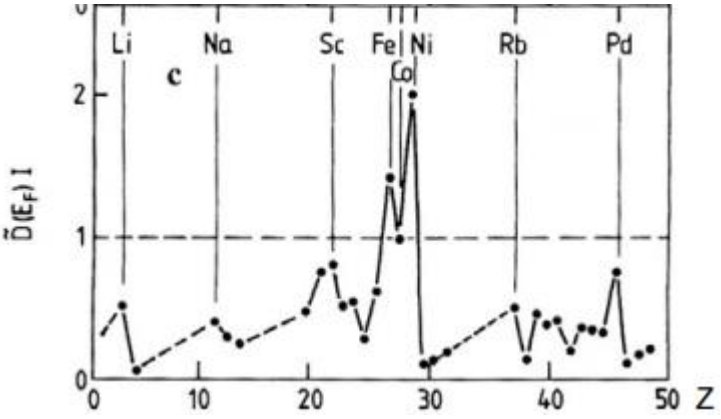

Figure 1.2. Stoner Criteria for different materials

Only Fe, Co and Ni pass the Stoner criteria of ferromagnetism. It is worth noting that Pd is very close to fulfill the Stoner condition with I D (E_F) = 0.8 and can be pushed to the magnetic state by inducing magnetic exchange field at the interface with an adjacent magnetic material. This phenomena is known as magnetic proximity effect and will be discussed in detail in Chapter 5.

The presence of the GMR effect has been anticipated since 1968 when Albert Fert compared the resistivity of Ni ($Co_{1-x}Rh_x$) and Ni ($Au_{1-x}Co_x$) [5-7]. He observed that the resistivity of the Ni ($Co_{1-x}Rh_x$) was higher than Ni ($Au_{1-x}Co_x$). This phenomena has been explained in terms of spin dependent conduction channels where Co impurities scatter strongly spin down electrons and Rh scatters the spin up electrons resulting in an enhanced resistivity for Ni ($Co_{1-x}Rh_x$). One the other hand, the Ni ($Au_{1-x}Co_x$) has only spin down

scattering channels arising from Co impurities leaving the spin up channel open, resulting in a lower resistivity. The idea of GMR is to control the high/low resistance state by replacing the Co and Rh impurities with magnetic layers for which the magnetization can be switched between parallel and antiparallel states. However, the distance between the two magnetic layers needs to be smaller than the mean free path (several nanometers) in order to observe such a magnetoresistive effect [3]. The deposition technique at that time was not well advanced to engineer such fine structure. Twenty years later, with the progress in thin film deposition using molecular beam epitaxy (MBE), Albert Fert discovered a very large magnetoresistance effect of 85% in Fe/Cr superlattices [1] shown in Figure 1.3 (a). The high resistance state at zero field corresponds to the antiparallel configuration (Figure 1.3 (c)) of the two iron layers while the parallel configuration, obtained by applying a magnetic field, results in a lower resistance as shown in Figure 1.3 (b).

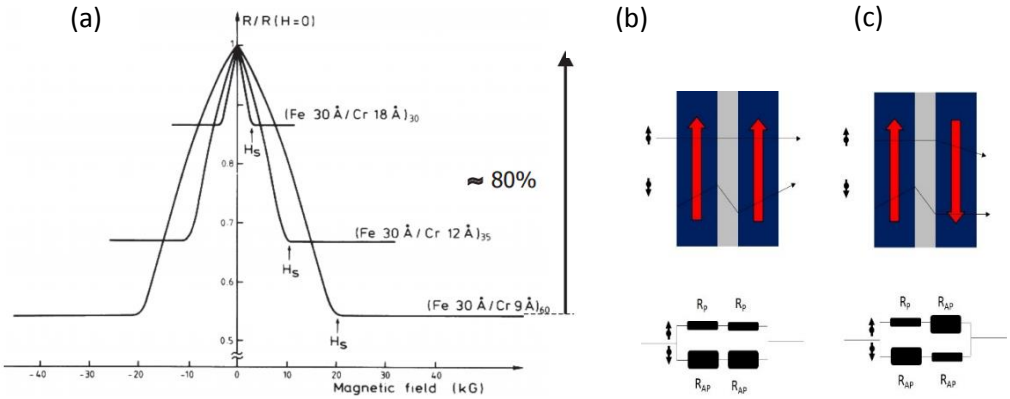

Figure 1.3. (a) Giant Magntoresistance (GMR) in Fe/Cr superlattices (b) Schematic of the GMR effect for two ferromagnets in the parallel configuration and (c) antiparallel configuration

The antiferromagnetic state is achieved using the RKKY coupling between the two iron layers through a very thin (1nm) nonmagnetic Cr layer.

The RKKY theory states that the coupling between the two ferromagnetic layers separated by a nonmagnetic layer is given by the exchange Hamiltonian $H_{exchange} = - J (\vec{M}_1 \vec{M}_2)$ where $\vec{M}_1$ and $\vec{M}_2$ are the magnetization of the magnetic layers and J is the exchange coupling coefficient proportional to $[\cos (2k_m d) - \frac{1}{2K_m d}\sin (2k_m d)]$ with k_m the wave vector and *d* the thickness of the nonmagnetic layer. In order to minimize the energy of the system, the coupling is ferromagnetic for J>0 whereas for J<0 it is antiferromagnetic. The coupling between Co/Cu multilayers was found to oscillate in sign and magnitude between ferromagnetic and antiferromagnetic states as function of the distance between the two layers, confirming the prediction of the RKKY theory Figure 1.4.

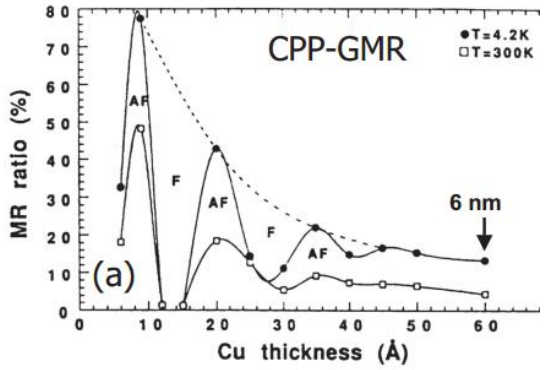

Figure 1.4. MR ratio with Cu nonmagnetic layer thickness

The GMR effect can be understood in terms of spin dependent conduction channels as shown in Figure 1.3 (b). The resistance of each ferromagnetic layer is described by two parallel resistors R_p and R_{ap} corresponding to magnetization parallel and antiparallel to the

incoming spins with $R_P < R_{AP}$. For example in Figure 1.3(b), spin up (down) will experience less (more) scattering in the parallel (antiparallel) configuration and the low resistance state is given by $R_{parallel} = \frac{R_P R_{AP}}{R_P + R_{AP}}$. On the other hand, in Figure 1.3(c) both spin up and spin down experience strong scattering and the high resistance is given by $R_{Antiparallel} = \frac{R_P + R_{AP}}{2}$. The MR ratio is given by:

$$MR = \frac{R_{Antiparallel} - R_{Parallel}}{2} \quad (1)$$

The pioneering work of Albert Fert on the GMR effect laid the foundation for the fascinating field of Spintronics. The GMR effect has been widely used to sense the magnetic field encoded in domain walls in hard drive applications and in automotive industry [3]. The GMR has also been used for magnetic random access memory (MRAM) applications to store information but with limited success. The low MR ratio was the main obstacle for achieving low read and write cycle time which makes GMR not very attractive for RAM applications [8]. An important breakthrough in MRAM applications was achieved with the discovery of Magnetic Tunnel Junction (MTJ) [9]. MTJs are made of two ferromagnetic electrodes separated by a thin tunnel barrier as shown in Figure 1.5(a). The spin transport across the junction is based on the spin dependent tunneling probabilities. The TMR originates from the different density of states in the spin subbands of the two ferromagnetic materials. Since the tunneling process preserves the spin orientation, electrons can only tunnel to a subband with the same spin orientation as shown in Figure 1.5 (b).

(a) (b)

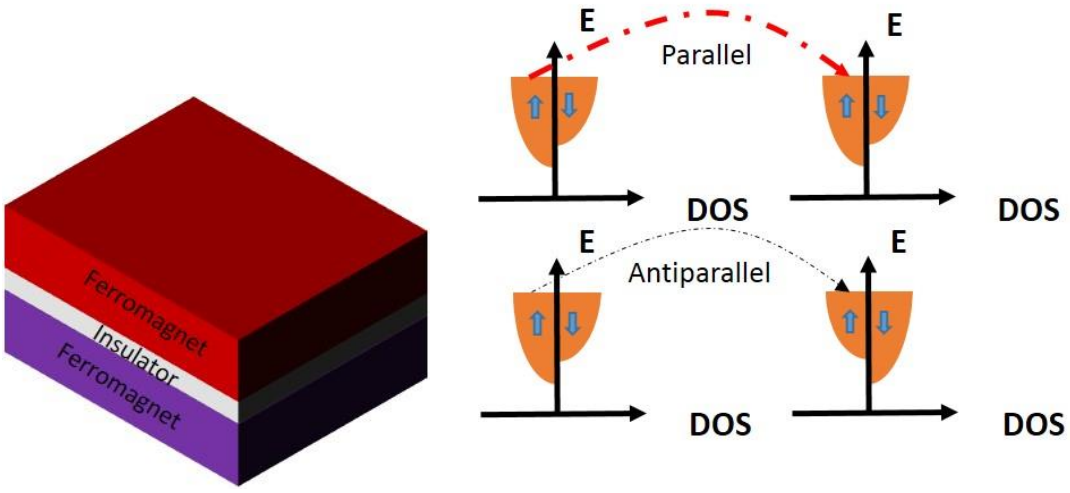

Figure 1.5. (a) Magnetic Tunnel Junction (MTJ) device (b) Tunneling process for parallel (red dashed curve) and antiparallel configuration (black dashed curve)

In the parallel configuration, there are more states available for spin up to tunnel to compared to spin down giving a high conduction state. However, in the antiparallel case, the spin subbands are switched and there are less states available for spin up to tunnel to which will result in a low conduction state. When the magnetization of the two ferromagnets are parallel to each other, it is highly likely that spins will tunnel through the barrier. If the magnetizations are antiparallel, the tunneling probability becomes low. In 2004, a TMR of 200 % has been achieved with MgO tunnel barriers at room temperature [10, 11] and a record TMR of 1800 % [12] has been obtained in 2003 using $La_{2/3}Sr_{1/3}MnO_3$ electrodes but with low Curie temperature of 350 K.

Another spin transport geometry is the lateral spin valve. This geometry offers the possibility to realize spin transistors [13] by manipulating spins inside the channel material. A spin FET is made of a ferromagnetic injector (source), spin channel material, a

ferromagnetic detector (drain) and a gate to manipulate spins by application of an electric field using the Rashba spin orbit coupling to break the inversion symmetry of the spin channel material as shown in Figure 1.6. At zero gate voltage, the spin orientation inside the spin channel material is conserved as they reach the detector, generating a low resistance state ("0") shown in Figure 1.6 (a).

(a) (b)

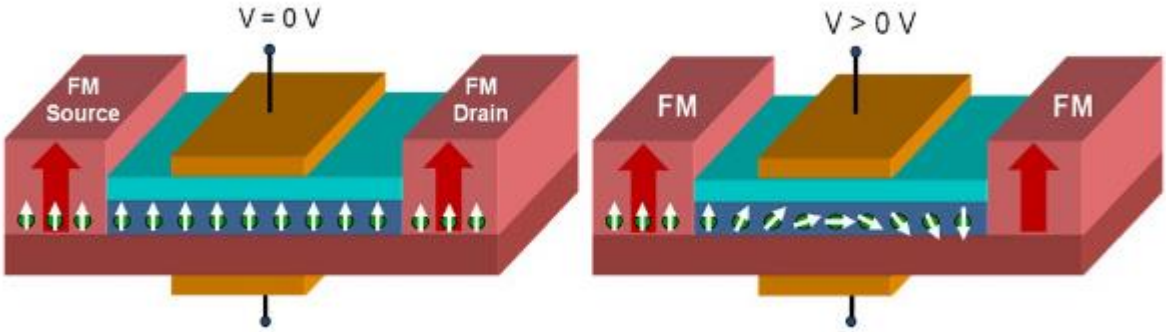

Figure 1.6. (a) Spin transistor in the parallel configuration V = 0V and (b) antiparallel configuration V > 0 V

However, as we start applying an electric field, the spins will precess and become antiparallel to the detector magnetization as shown in Figure 1.6 (b), generating a high resistance state ("1").

Let us now discuss the physics underlying spin injection, spin transport inside the channel material and spin detection. The two current model in a ferromagnet implies the presence of two different conductivity for each spin subband denoted by $\sigma_{\uparrow}$ and $\sigma_{\downarrow}$. The overall conductivities is then equal to $\sigma_F = \sigma_{\uparrow} + \sigma_{\downarrow}$. Since the conductivity of the majority spins (spin up) is higher than minority spin (spin down), we define:

$$\sigma_{\uparrow} = \alpha_F \sigma_F \quad \text{and} \quad \sigma_{\downarrow} = (1-\alpha_F)\sigma_F \qquad (2)$$

with $0 \leq \alpha_F \leq 1$ accounting for the asymmetry of the conduction inside the ferromagnet. If we apply a charge current along the ferromagnet, Ohm's law states:

$\frac{\partial \mu}{\partial x} = -\frac{e}{\sigma} j$ where $\mu_{FM} = \alpha_F \mu_{\uparrow} + (1-\alpha_F)\mu_{\downarrow}$ is the chemical potential and j is the current density. In the case of a nonmagnetic material, since $\mu_{\uparrow}$ and $\mu_{\downarrow}$ are equal, the chemical potential is $\mu_{NM} = \frac{1}{2}(\mu_{\uparrow} + \mu_{\downarrow})$. In Figure 1.7 shows the chemical potential in a FM adjacent to NM under an applied bias. Due to the large number of majority electrons with spin up compared to minority spin down electrons, the spin up chemical potential $\mu_{\uparrow}$ is energetically higher than $\mu_{\downarrow}$. Close to the interface, the different conductivity of spin up and down results in a different slope in the chemical potential profile. Given that the average chemical potential in the FM lies higher than the middle of $\mu_{\uparrow}$ and $\mu_{\downarrow}$ and the chemical potential in the NM has equal $\mu_{\uparrow}$ and $\mu_{\downarrow}$, a discontinuity in the chemical potential μ_{FM} and μ_{NM} at the interface builds up.

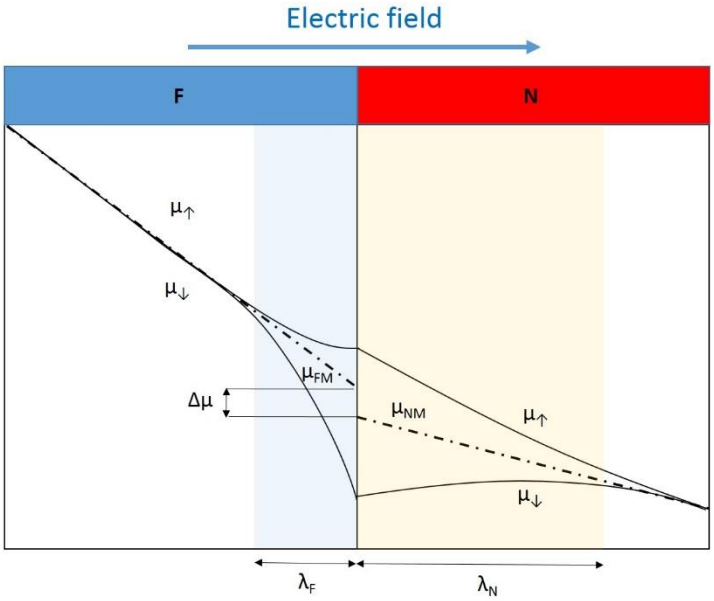

Figure 1.7. Spin accumulation profile at the ferromagnet (F)/nonmagnet (N) interface under an applied bias

At the interface, the spin dependent chemical potentials $\mu_\uparrow$ and $\mu_\downarrow$ are continuous between the two materials. Away from the interface, the spin chemical potential decays exponentially with a characteristic length $\lambda_{F(N)}$ commonly known as the spin diffusion length and equal $\lambda_{F(N)} = \sqrt{D_{F(N)}\tau_{F(N)}}$ where D is the diffusion coefficient and τ is the spin lifetime. In the NM material, spin up will flow to the right hand side and spin down will flow to the left, creating a "spin current" $J_s = J_\uparrow - J_\downarrow$. After few spin diffusion lengths, the spin chemical potential will approach the average chemical potential in the NM material and the spin current will equal to zero. In the FM material, the spin diffusion is accompanied by drift since there is an electric field applied. The spin accumulation in the NM material is probed by placing another ferromagnetic electrode, referred as a detector, at a distance comparable to the spin diffusion length of the NM material. A spin

accumulation builds up at the detector and results in a positive non-local voltage V_p. The continuity of spin accumulation at the interface requires the alignment of $\mu_{\uparrow FM}$ with $\mu_{\uparrow NM}$ allowing us to probe the spin up accumulation. As we switch the magnetization of the detector from parallel to the injector to antiparallel, we start probing spin down $\mu_{\downarrow NM}$ as opposed to $\mu_{\uparrow NM}$ resulting in a negative non-local voltage V_{AP}. The non-local MR is defined as $MR = \frac{V_P - V_{AP}}{I_{inj}}$ where I_{inj} is the injected current. The first successful demonstration of spin injection and detection in lateral spin valve was done by Johnson and Silsbee [14] in 1985 shown in Figure 1.8.

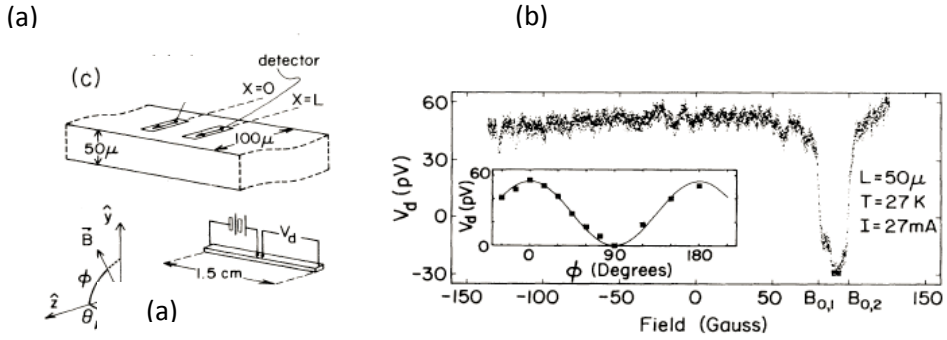

Figure 1.8. (a) Non-local spin valve geometry (b) Non-local MR measurement and Hanle angular dependence (inset)

The injector and detector are made of Py bridged by a 50 μm single crystal Aluminum bar. In their seminal work, they used a non-local measurement scheme shown in Figure 1.8 (a) that consists of separating out the current injection loop from the voltage detection referred to as the 4-terminal geometry. This geometry allows to prevents any spurious effects in the measurement arising from charge transport such as Anisotropic Magnetoresistance (AMR). By sweeping the magnetic field along the easy axis of the Py

electrodes from negative values to positive, they observe a sudden jump in the non-local voltage shown in Figure 1.8 (b) demonstrating the first successful non-local spin transport. The theory of non-local spin transport has been developed by Takahashi and Maekawa in a paper published in 2003 [15]. The non-local magnetoresistance is given by:

$$R_{NL} = \pm \frac{R_N e^{-\frac{L}{\lambda_N}} \prod_{i=1}^{2} \left(\frac{P_J \frac{R_i}{R_N}}{1 - P_J^2} + \frac{P_F \frac{R_F}{R_N}}{1 - P_F^2} \right)}{\prod_{i=1}^{2} \left(1 + \frac{2\frac{R_i}{R_N}}{1 - P_J^2} + \frac{2\frac{R_F}{R_N}}{1 - P_F^2} - e^{-2\frac{L}{\lambda_N}} \right)} \quad (3)$$

where $R_N = \frac{\rho \lambda_N}{W}$ is the spin resistance of the nonmagnetic channel, $R_F = \frac{\rho \lambda_F}{A}$ is the spin resistance of the ferromagnetic material, R_i is the contact resistance of the injector and detector, P_J is the spin injection efficiency and P_F is the spin polarization of the feromagnet.

In a later paper published in 2002, Jedema et al. [16] optimized the experiment by shrinking down the device dimensions from μm to the nm range and observed a strong signal in the mΩ range with clear MR switching. The spin lifetime was extracted using the non-local Hanle spin precession measurement. Here, an out-of-plane magnetic field is applied causing the spins to precess as they diffuse toward the detector resulting in the non-local Hanle curve shown in Figure 1.9. At zero field, the spin polarization is parallel to the detector magnetization producing a positive non-local voltage. As the out-of-plane magnetic field $B_\perp$ is increased, the spin population starts precessing around the magnetic field axis and the spin orientation acquires an angle of $\pi/2$ relative to the detector magnetization. The measured non-local voltage then drops to zero since the detector is not sensitive to the perpendicular spin polarization.

As we further increase $B_\perp$, the average spin orientation acquire an angle of π relative to the detector producing a negative non-local voltage. At high $B_\perp$, the entire injected spin population dephases and the net spin polarization becomes zero resulting in a suppression of the non-local signal. In order to extract the spin lifetime, the Hanle curve shown in Figure 1.9 is fitted using the Bloch equation:

$$R_{NL} = S\int_0^\infty \frac{e^{-L^2/4Dt}}{\sqrt{4\pi Dt}}\cos(\omega t)e^{-\frac{t}{\tau}}\,dt \qquad (4)$$

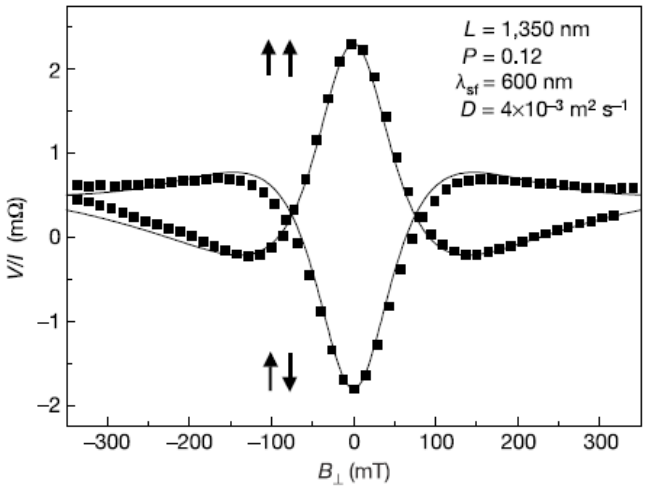

Figure 1.9. Non-local Hanle measurement for the parallel and antiparallel configuration

with $\omega = 2\pi g\frac{\mu_B}{h}B_\perp$, S is the amplitude, D is the diffusion coefficient and τ is the spin lifetime.

The free fitting parameters are τ, D and S. The extracted spin diffusion length for the Al channel was $\lambda_{Al} = 600\ nm$ with D = 4 x 10^{-3} m^2/s.

1.2 Graphene spintronics:

Graphene is a two-dimensional material made of carbon atoms arranged in a honeycomb structure with sp^2 bonding. It was isolated for the first time in 2004 by Novoselov and Geim [16] using mechanical exfoliation for which they were awarded the 2010 Nobel Prize for this important discovery. The discovery of graphene has launched the search for other van der Waals materials that resulted in the discovery of a plethora of new 2D materials [17].

The graphene lattice consists of two sublattices A and B as shown in Figure 1.10. A carbon atom in the A (B) sublattice is covalently bonded to 3 nearest neighbor carbon atoms in the B (A) sublattice.

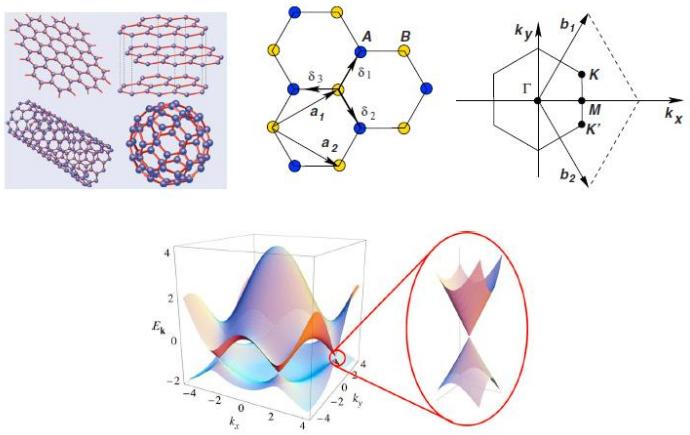

Figure 1.10. Graphene crystal lattice showing A and B sublattices and band structure of graphene.

The band structure of graphene can be derived using the tight binding model and the dispersion relationship is given by:

$$E(k) = \pm\frac{h}{2\pi}\frac{3ta}{2k}k = \pm v_f k \qquad (5)$$

The linear dispersion at the K and K' points implies that electrons in graphene are massless acquiring a fermi velocity up to $V_F = 10^6$ m/s. Around the K and K' points, the bands form a cone commonly known as Dirac cone. Graphene does not have a bandgap therefore it is considered as a semimetal. The carrier type can be tuned from electrons to holes by moving the Fermi level across the top and bottom Dirac cone. Due to its high Fermi velocity, graphene exhibits high mobility exceeding 500,000 cm^2/Vs [18-22]. In addition to its excellent electronic properties, graphene is very promising as a non-magnetic channel material for spin transport. Graphene has a low spin orbit coupling due to the low Z factor of C that makes up graphene and weak hyperfine coupling [23-26]. The high mobility combined with low spin orbit coupling and weak hyperfine coupling makes graphene a promising material for spin transport. Theoretically, the spin lifetime in graphene is expected to be in the microsecond range as calculated in ref [27]. The first report of non-local spin transport in graphene was demonstrated by Tombros et al in 2007 [28]. The device shown in Figure 1.11 is made of Co/Al_2O_3 injector and detector deposited on single layer graphene. The role of the Al_2O_3 tunnel barrier is to circumvent the spin absorption from the contact commonly known as "conductivity mismatch problem". Due to the low spin resistance $R_S = \lambda\rho/A$ of the ferromagnetic contact relative to the graphene spin resistance, the injected spin current will flow back to the ferromagnetic contact instead of diffusing into the graphene channel resulting in low spin injection efficiency.

(a) (b)

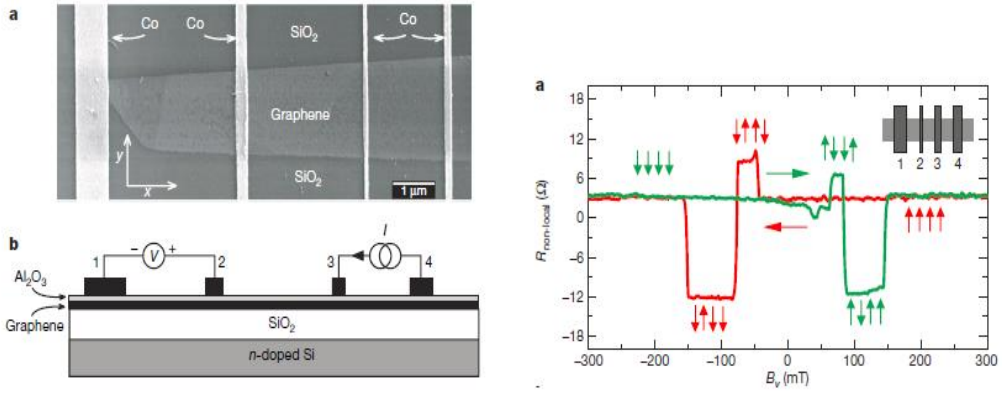

Figure 1.11. Graphene non-local spin valve with Al_2O_3 barrier (a) Graphene spin valve SEM picture and non-local measurement geometry (b) Non-local MR measurement

The Al_2O_3 barrier provides high contact resistance R_c preventing the backflow of spins [29]. The spin injection occurs by tunneling through the Al_2O_3 barrier. A non-local MR of 12 Ω was measured and the extracted spin lifetime from the Hanle measurement was in the range of 100 ps giving a spin diffusion length of 1 – 2 µm. The discrepancy between the theoretical, in the microseconds range, and the experimental spin lifetime was quite puzzling. Later in 2010, Wei Han studied the effect of tunneling contact on the spin lifetime and spin injection efficiency [30 – 32]. It was shown that a spin lifetime up to 1 ns and spin injection efficiency of 30% were achieved using a pinhole free MgO with TiO_2 seeding layer grown by MBE. The spin lifetime for ohmic, pinhole and tunneling contact were studied as shown in Figure 1.12. It was shown that the spin lifetime for Ohmic and pinhole contact were limited to 80-200 ps. On the other hand, for tunneling contact the spin lifetime increased to 771 ps.

(a) (b) (c)

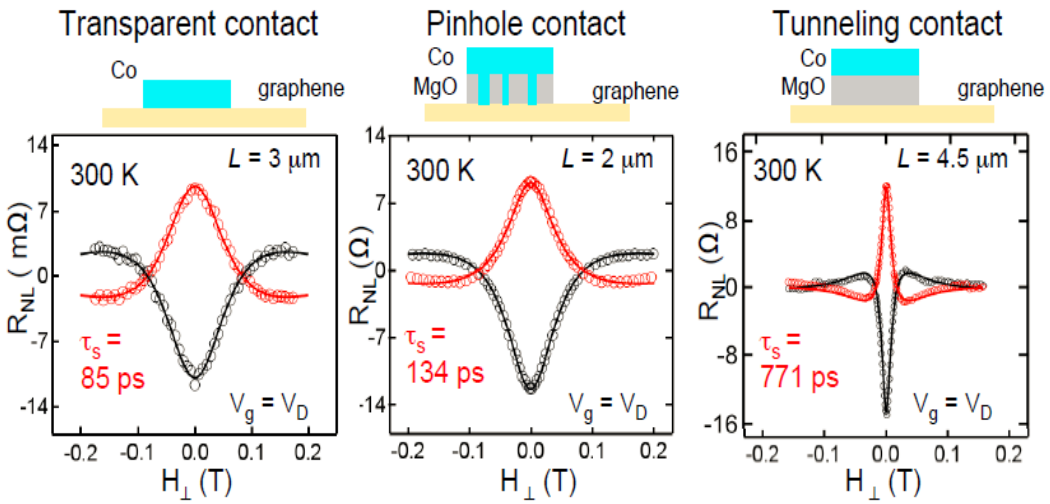

Figure 1.12. (a) Non-local Hanle for transparent contact (b) pinhole contact and (c) tunneling contact.

This elegant study demonstrates that the contact is the bottleneck for achieving high spin lifetime. Although the contact resistance of the pinhole contacts was considerably higher than the graphene spin resistance, thus preventing any back flow of spins, the spin lifetime was still short. This result hints to the presence of an additional spin dephasing under the contact other than spin absorption. Spin dephasing such as fringe field at the ferromagnet/graphene interface and orbital hybridization are likely responsible of the observed short spin lifetimes. Indeed, in 2016,through a systematic study of transparent, pinhole and tunneling contacts using Al_2O_3 and MgO [33], I demonstrated the presence of an extra spin dephasing other than spin absorption by comparing the spin lifetime obtained

from the traditional Bloch equation and the modified version that takes in account the contact resistance. This specific study will be discussed in detail in Chapter 4 of this thesis.

Away from the contact, the main source of spin relaxation in graphene are Elliot Yafet (EY) [35, 36], D'yakonov Perel (DP) [37] and resonant scattering mechanisms [38]. The EY spin relaxation is a process where spin flips direction (Figure 1.13 a) during a scattering from charged impurities, adatoms, edge roughness or ripples in the graphene channel. The spin flip probability is directly proportional to momentum scattering probability. The more momentum scattering, the higher the probability of spin flip. Therefore, in the EY mechanism, the spin lifetime $\tau_s \propto \tau_m$ where τ_m is the momentum scattering time.

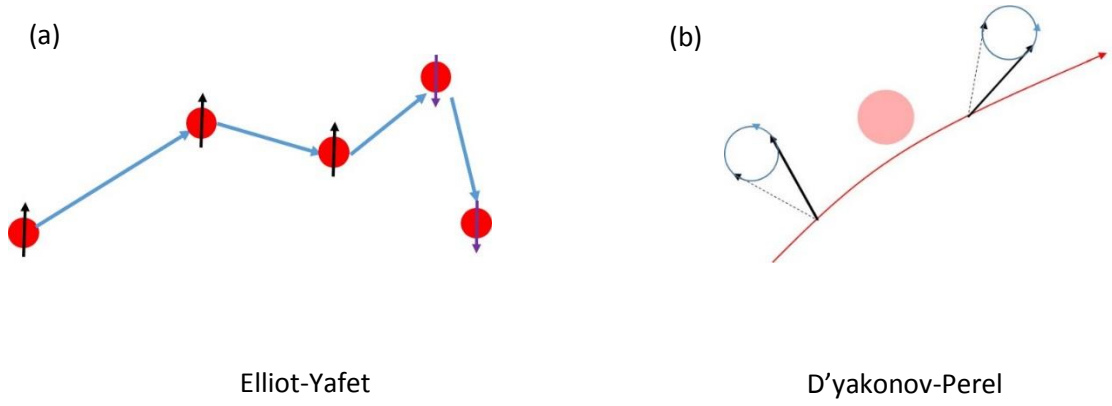

Figure 1.13. (a) Elliot-Yafet mechanism (EY) (b) D'yakonov-Perel mechanism

The DP spin relaxation is described by spin precession around random spin orbit fields resulting from the lack of inversion symmetry. In general, spin orbit fields will cause dephasing of the spin polarization that depends on the momentum k. However, as the electron experience inelastic scattering, its spin precess around random spin orbit fields

resulting in a decrease of spin relaxation due to shorter spin precession time. The more momentum scattering the spin experience, the less the spin relaxation. The relationship between spin relaxation time and momentum scattering time is given by:

$$\tau_s \propto \frac{1}{\tau_p} \qquad (6)$$

Through systematic gate dependence study of the spin lifetime in SLG and BLG, Han et al [31] investigated the relationship between the momentum relaxation time and spin lifetime and concluded that EY mechanism is dominant in SLG while the DP mechanism is relevant in MLG. However, subsequent studies found no correlation between the spin lifetime and the momentum relaxation time in SLG and BLG ruling out EY and DP as the only spin relaxation mechanisms in SLG and MLG. It is worth noting that the EY and DP mechanisms give a spin relaxation time τ_s on the order of μs. This is still three orders of magnitude higher than the experimental values in the ns range. A new spin relaxation mechanism based on resonant scattering with magnetic moments has been proposed to explain the short spin lifetime. At the resonance energy, the electron will spend a considerable amount of time circling around the magnetic moment. As the electron exits the magnetic moment site, its spin direction will have equal probability for pointing up or down. Averaging over an ensemble of resonant energies, the spin lifetime is predicted to be in the hundreds of ps for 1 ppm of magnetic moments. In general, the dominant spin relaxation mechanism remains a controversial topic in the graphene spintronics community. A breakthrough in the field of graphene spintronics was the enhancement of the spin lifetime to 12 ns (Figure 1.14) and an increase of spin diffusion up to 30.5 μm at room temperature achieved by the Beschoten group [39]. This accomplishment was

achieved by fabricating Co/Mgo electrodes on Si/SiO_2 and the subsequent dry transfer of a graphene-hBN stack on top of the electrodes.

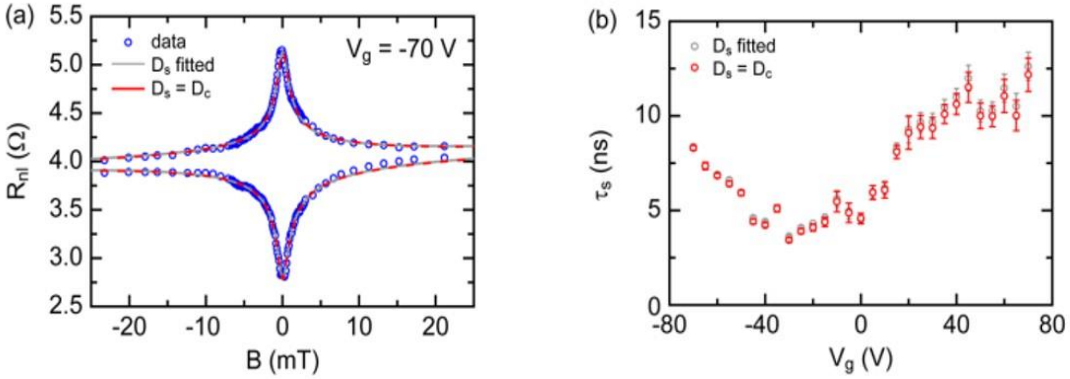

Figure 1.14. (a) Non-local Hanle for the parallel and antiparallel configuration (b) Gate dependence of the spin lifetime

In this way, the graphene does not get exposed to any resist during the device fabrication process and the surface remains pristine. The authors show that using large hBN flake was the key to obtain large spin lifetimes as it prevents the ingress of solvent along the hBN/graphene interface. It is worth noting that they used MgO barrier with pinholes suggesting that contact spin relaxation is still significant in their experiment. Nevertheless, the spin lifetime obtained was record high. This suggests that further enhancement of spin lifetime is possible by optimizing the contact.

1.3 Magnetic Proximity Effect:

Magnetic Proximity Effect (MPE) is a process where a nonmagnetic material acquires a spin polarization due to coupling with another magnetic film. There are two types of MPE that can produce interfacial spin polarization: Static MPE and non-

equilibrium MPE. While the former has been widely investigated, the non-equilibrium MPE has been discovered only few years ago and a theory based on Spin Hall Magnetoresistance (SMR) was proposed to explain the aforementioned effect.

1.3.1 Static MPE:

Static MPE is an exchange coupling between the magnetic moments of the FMI and the electronic states of the NM, leading to an effective magnetic exchange field (MEF) experienced by conduction/valence band electrons in the NM and/or induced ferromagnetic ordering of localized d- or f-shell magnetic moments. The first report of magnetic proximity was done in 1969 [41] using the superconducting proximity effect. It has been found that the superconducting transition temperature in Pb-Pd-Fe decreases with decreasing the thickness of Pd indicating that the Pd layer became magnetized when in contact with the Fe. Later, it has been shown that ferromagnetic materials Fe and Co can induce magnetization into a 4d and 5d elements such as Pd and Pt [42-45]. There are two mechanisms that governs the static MPE: One is a short range interfacial effect that depends on the degree of hybridization between the nonmagnetic and magnetic material [46]. The second is a long range exchange coupling that occurs through the RKKY interaction [47-50]. In 2012, Bailey et al [51] observed long range interlayer exchange coupling between Pd and Py through a 3 nm Cu spacer using XMCD measurement and extracted a magnetic exchange field acting on the Pd of 2T.

The ability to induce MPE into a NM material depends heavily on its electronic structure. NM with large density of states and high magnetic susceptibility are more susceptible to acquire spontaneous magnetization as they are close to fulfill the Stoner

criteria. The Stoner criteria is defined as $ID(E_F) > 1$ where I is the exchange energy and $D(E_F)$ is the density of states at the Fermi level. Any material that fulfill this condition will acquire a spin polarization. For example, Pt has $ID(E_F) \approx 0.6$ whereas for Pd $ID(E_F) \approx 0.85$ are very close to fulfilling the Stoner condition. Therefore, a small magnetic exchange field from an adjacent magnetic material will drive the paramagnet to a ferromagnetic state.

The MPE effect is particularly important for low energy consumption spintronics devices. It has been used to fully modulate spins in Graphene/YIG structure [52-54] and induce Zeeman splitting of 2 meV in EuS/graphene corresponding to an interfacial exchange fields as high as 14 T [55]. In addition, out of plane MEF at the WSe_2/EuS interface has been shown to enhance the valley-dependent spin splitting in the WSe_2 layer. This opens the possibility for developing novel low power devices that do not require the application of an external magnetic field. Recently, there was a growing interest for using Ferromagnetic Insulators (FMI) as opposed to ferromagnets to induce magnetic exchange fields to a nonmagnetic material. First, FMIs do not provide a parallel conduction path for the electrical current and therefore most of the charge current will flow through the NM on top, which will result in a low power consumption. Second, the MPE signal will not be obscured by the magnetic property of the underlying magnetic substrate providing a clearer interpretation of the the spin polarization in the NM material only. YIG has been widely used to study the MPE in Pt and more recently in graphene [53] due its low damping. Huang et al [57] demonstrated the magnetic proximity effect in a YIG/Pt system by anomalous Hall effect (AHE) and anisotropic magnetoresistance (AMR) measurement. In a later paper, they measured directly a magnetic moment of $0.054\mu_b$/Pt atom at 300 K using

XMCD [58]. However, Geprags et al [59] denied the presence of magnetic moment in the Pt on YIG grown by Pulsed Layer Deposition (PLD) using XMCD down to the resolution limit of $0.003\mu_b$/atom, while Lu et al. [58] observed a magnetic moment of $0.054\mu_b$/Pt atom using YIG grown by liquid phase epitaxy (LPE). This blatant discrepancy suggests that the interface between the FMI and Pt is the key toward observing MPE, which is tied up closely to the growth process of the FMI/Pt structure.

1.3.2 Non-equilibrium MPE and Spin Hall Magnetoresistance (SMR):

In the non-equilibrium MPE process, the NM acquires a spin polarization by an external stimulus such as charge current, thermal gradient and spin pumping that drives the system out of equilibrium. This is fundamentally different than static MPE where a spontaneous spin polarization emerges in the NM as a result of a magnetic exchange field produced by the underlying magnetic substrate. The most common case of non-equilibrium MPE in the FMI/NM system is based on the Spin Hall Magnetoresistance (SMR) [60]. Due to the high spin orbit coupling (SOC) of the heavy NM material, a longitudinal charge current will produce a transverse spin current by the spin Hall effect as shown in Figure 1.15 (a). The spin to charge coupling is given by:

$$J_s = \theta_{SH} (\sigma \times J_c) \qquad (7)$$

where θ_{SH} is the spin Hall angle, σ is the spin polarization and J_c is the charge current.

The generated spin current will cause spin accumulation at the interface between the FMI/NM that depends on the relative orientation of the FMI magnetization to the spin current polarization. In the perpendicular configuration (Figure 1.15. b) $\sigma \perp$ M, the spin current will get absorbed by the FMI in the form of spin transfer torque.

(a) (b)

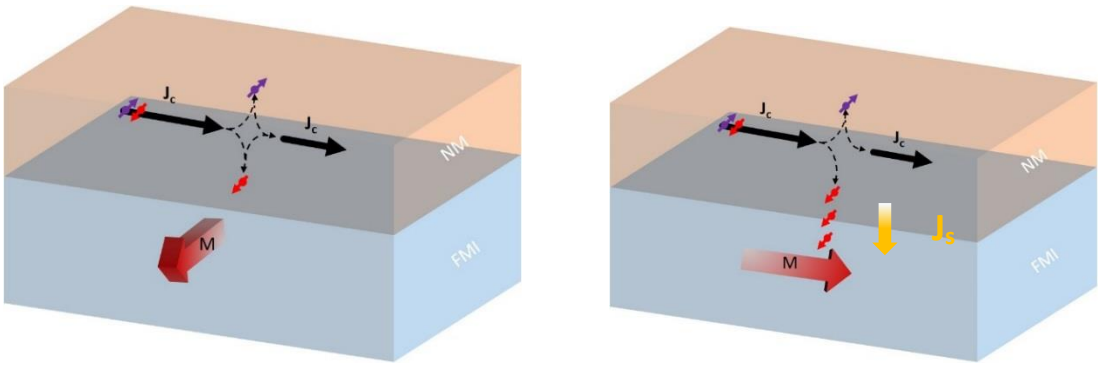

Figure 1.15. (a) Spin Hall Magnetoresistance (SMR) in the parallel configuration (low resistance state) (b) Spin Hall Magnetoresistance (SMR) in the perpendicular configuration (high resistance state)

However, in the case of $\vec{\sigma}$ // $\vec{M}$ (Figure 1.15. a), the spin current will get reflected at the interface and converted to charge current by the Inverse Spin Hall Effect (ISHE) as shown in Figure 1.15 (b).

Therefore the measured longitudinal resistance of the Pt film depends on the orientation of $\vec{\sigma}$ relative to $\vec{M}$. A high resistance state is obtained for the perpendicular orientation while a lower resistance state is obtained for the parallel configuration. The spin current density at the magnetic interface is given by the spin mixing conductance and the spin accumulation as follows:

$$J_s = G_r\, M \times (M \times \mu_s) + G_i(M \times \mu_s) \qquad (8)$$

In the SMR theory published by Bauer et al [60], the change in the longitudinal resistivity is given by:

$$\rho_{xx} = \rho + \Delta\rho_0 + \Delta\rho_1 (1-\mathbf{m}^2_y),\ \rho_{xy} = -\Delta\rho_1 \mathbf{m}_x \mathbf{m}_y + \Delta\rho_2 \mathbf{m}_z \qquad (9)$$

where $\mathbf{m}_x$, $\mathbf{m}_y$ and $\mathbf{m}_z$ are components of the magnetization unit vector in the FMI. The transverse resistivity contribution $\Delta\rho_2$ stems from the imaginary part of the spin mixing conductance G_i. This effect is related to the out of plane exchange field from the FMI acting on the pure spin current generated by the SHE. The spin current at the interface undergoes spin precession as it reflects back producing an AHE-like signal given by equation (15). The SMR coefficients $\Delta\rho_1$ and $\Delta\rho_2$ are related to G_r and G_i by:

$$\frac{\Delta\rho_1}{\rho} = \theta_{SH} \frac{\lambda}{d_N} \frac{2\lambda G_r tanh^2 \frac{d_N}{2\lambda}}{\sigma + 2\lambda G_r \coth\frac{d_N}{\lambda}},\ \frac{\Delta\rho_2}{\rho} = \frac{2\lambda^2 \theta_{SH}{}^2}{d_N} \frac{\sigma G_i tanh^2 \frac{d_N}{2\lambda}}{(\sigma + 2\lambda G_r \coth\frac{d_N}{\lambda})^2} \qquad (10)$$

When the magnetization m_z is non zero, the imaginary part of the spin mixing conductance produces an additional transverse contribution. As we will see in Chapter 5 of this thesis, this effect can obscure the MPE AHE signal and make the interpretation of the static MPE characterized by AHE difficult. In order to electrically detect the static MPE signal we perform anomalous Hall and anisotropic magnetoresistance measurement.

1.3.3 Spin Hall Effect:

The Spin Hall Effect (SHE) is the generation of pure spin current transverse to an applied charge current. The origin of the SHE dates back to 1929 when Mott first studied the scattering of an unpolarized beam of electron from a heavy gold nuclei in vacuum referred as the double scattering experiment. Due to the spin orbit coupling of the heavy

nuclei, a perpendicular beam with spin polarization normal to the scattering plane was produced.

In a paper published by D'yakonov and Perel in 1971 [62], the SHE was theoretically represented as an asymmetric spin dependent scattering that produces edge spin accumulation of opposite spin polarization. This edge spin accumulation can induce efficient magnetization switching to an adjacent ferromagnet by Spin Torque Switching as demonstrated by Ralph group using Tantalum [63]. The first direct measurement of SHE was done Kato, et al [64] in 2004 where they used Magnetic Optic Kerr Effect (MOKE) to map out the spin accumulation at the edges of GaAs as shown in Figure 1.16. There are three mechanisms that produce the SHE: skew, side jump and intrinsic mechanisms. The skew scattering represents the asymmetrical spin dependent scattering of conduction electrons in the presence of spin orbit coupling at charged impurity sites. In the reference frame of the electron, the charged impurity will act as a moving charge that produces a magnetic field by relativistic effects.

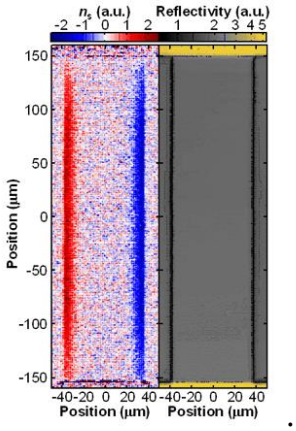

Figure 1.16. Spin Hall accumulation measured by MOKE in GaAs

This will deflect the electrons in opposite direction with respect to their spin polarization as shown in Figure 1.17 (a).

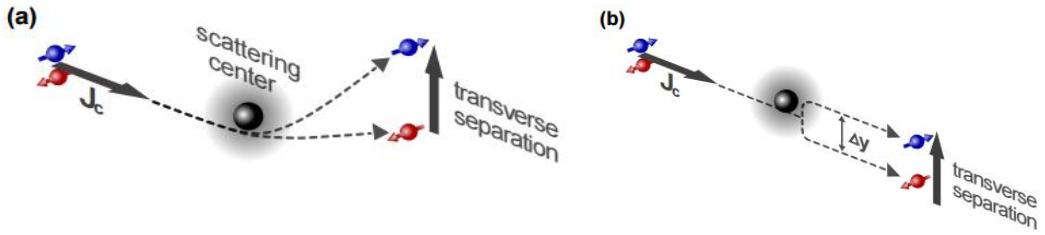

Figure 1.17. (a) Skew scattering mechanism (b) Side jump mechansim

This phenomena is referred as spin orbit coupling (SOC). The Hamiltonian of the SOC is given by:

$$H_{SO} = -\frac{2\pi\lambda^2}{4h}\,[p \times \nabla V(r)].\sigma \qquad (11)$$

where $\lambda = \frac{h}{2\pi\, mc}$ is the Compton wavelength of the electron, p is the momentum, V is potential around the impurity and σ is the spin polarization. The skew scattering conductivity is linearly proportional to the charge conductivity by:

$$\sigma_{SS}^{SHE} = 10^{-3}\,\frac{\sigma_c}{1+\gamma\tau} \qquad (12)$$

where σ_c is the charge conductivity, γ is the spin Coulomb drag coefficient and τ is the momentum relaxation time.

The side jump mechanism was proposed by Berger [65] where electron wave packets traveling in the x direction scattered by a central potential at the impurity site in the presence of spin orbit coupling, experience an abrupt jump in the y direction depending

on their spin orientation as shown in Figure 1.17 (b). The side jump conductivity is related to the charge conductivity by:

$$\sigma_{SJ}^{SHE} = \frac{-4\pi e^2}{h} n\lambda_c^2 \qquad (13)$$

Which mechanism is more dominant? The interplay between the skew scattering and side jump mechanism depends on the mobility of the material. While skew scattering is proportional to the mobility of the material, the side jump is independent of it. Therefore, increasing the mobility will increase the skew scattering contribution.

Finally, the intrinsic mechanism does not depend on the presence of impurities inside the NM material. Instead it originates from the spin dependent band structure of the material and more specifically from the Berry phase. The Berry phase plays a very important role in the anomalous Hall effect and will be discussed in the next section.

Overall the spin hall conductivity is the sum of the skew scattering, side jump and intrinsic contribution: $\sigma^{SHE} = \sigma_{intrinsic}^{SHE} + \sigma_{SS}^{SHE} + \sigma_{SJ}^{SHE}$

The efficiency of charge to spin conversion is given by the ratio of the spin hall conductivity σ^{SHE} and the charge conductivity σ_c usually referred as the spin hall angle $\theta_{SH} = \frac{\sigma^{SHE}}{\sigma_c}$.

The relationship between the induced spin current and charge current is given by:

$$\overrightarrow{J_s} = \theta_{SH}\left(\frac{-h}{4\pi e}\right)\overrightarrow{J_q} \times \vec{s} \qquad (14)$$

where $\overrightarrow{J_q}$ is the charge current and $\vec{s}$ is the spin polarization.

1.3.4 Anomalous Hall Effect:

The anomalous Hall effect (AHE) originates from the same mechanism as the Spin Hall Effect except that the conductor has a net spin polarization due to the exchange splitting in the 3d bands. Electrons in ferromagnets experience asymmetric spin dependent scattering, a consequence of the spin orbit coupling. Due to the higher density of states of the majority spin compared to the minority spins, the spin dependent scattering will produce an accumulation of majority electrons at one edge and minority electrons at the opposite edge of the ferromagnet resulting in a net measurable voltage as shown in Figure 1.18. The spin polarization inside a ferromagnet (majority and minority spins) will depend on its magnetization. This will result in a measured voltage that depends on the magnetization of the ferromagnet. According to Noziers and Lewiners [66] the anomalous Hall current is given by:

$$\overrightarrow{J_{AHE}} = 2ne^2\lambda_{SOC}\,\vec{E}\times\vec{S} \qquad (15)$$

where n is the carrier density, λ_{SOC} is the spin orbit coupling constant, E is the electric field and S is the spin polarization. According to equation (15), an out of plane spin polarization S is required in order to get an anomalous Hall current transverse, in the y direction, to the longitudinal electric field $\vec{E}$. Therefore, in a typical AHE measurement, an out of plane magnetic field is applied in order to magnetize the ferromagnet out of plane and measure a transverse AHE voltage as shown in Figure 1.18.

Overall the Hall voltage in a ferromagnet is a superposition of the ordinary Hall effect and a term that depends on the out of plane magnetization that is the anomalous Hall effect and given by:

$$\rho_H = R_{Hall} H_z + R_S M_z \quad (16)$$

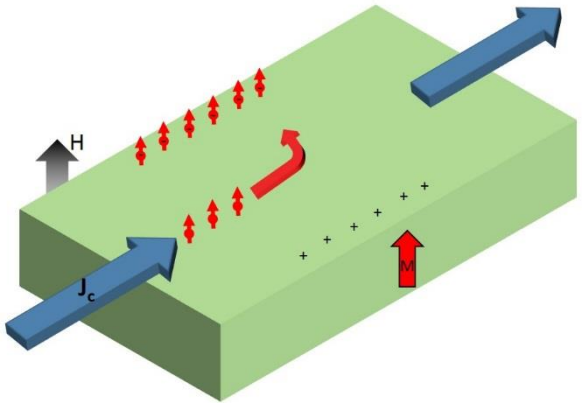

Figure 1.18. Anomalous Hall Effect (AHE)

where R_{Hall} is the Hall coefficient, H_z is the out of plane applied field, R_S is the anomalous Hall resistance and M_Z is the magnetization of the ferromagnet. Equation (16) implies that in addition to the linear dependence of the ordinary Hall Effect, the Hall voltage will depend on the magnetization and shares a profile that follows the magnetization of the ferromagnet. For example the Hall resistance of a Ni film saturates at high field and has a clear hysteresis shape that mirrors the magnetization of the Ni film. Current understanding of the AHE in ferromagnets is based on three different mechanisms: skew scattering, side jump and intrinsic mechanism that is based on the Berry phase in the momentum space. The Berry phase is a geometrical phase that emerges from the Bloch equation describing electrons in a periodic crystal. Let us define the wave function $u_{nq}(r) = e^{-iqr}\ \omega_{nq}\ (r)$ that satisfies the periodic boundary conditions in a periodic crystal $u_{nq}(r + a) = u_{nq}(r)$ as stated by the Bloch theorem. If we force the momentum of the wave function to vary in a

closed loop *C* in the momentum space, for example by applying an electric field that sweeps the momentum q along the Brillouin Zone (BZ), the phase picked up by the wave function after circling the BZ will be given by:

$$\gamma_n = \int_{BZ} dq \ \ < u_n(q)\big|\, i\nabla_q \big| u_n(q) > \quad (17)$$

This Berry phase is usually associated to the Berry curvature by:

$$b_n\,(q) = \nabla_q \ \times < u_n(q)\big|\, i\nabla_q \big| u_n(q) > \ (18)$$

Using Schrodinger equation, the electronic velocity is given by: $v = \frac{2\pi\ dE_n(q)}{h\ dq} - \frac{2\pi E}{h} \times$ $b_n\,(q)$ where E is the electric field and E_n is the energy of the band n.

Usually the Berry curvature $b_n\,(q)$, referred as the intrinsic spin orbit coupling, will vanish if the system preserves time reversal and inversion symmetry after integrating q along the BZ. However, in the case of a ferromagnet, the time reversal symmetry is broken due to the presence of finite magnetization, therefore giving a non-zero Berry curvature that produces an additional transverse velocity. This additional velocity is usually referred as the anomalous Hall velocity. Non-magnetic materials also can exhibit a non-zero Berry curvature if the inversion symmetry is broken. Overall, the AHE effect will allow us to characterize MPE in a nonmagnetic material by subtracting the ordinary Hall from the Hall voltage.

1.3.5 Anisotropic magnetoresistance:

AMR describes the change in the resistance of a ferromagnetic film that depends on the magnetization direction. The resistance is high when the magnetization $\vec{M}$ is parallel to the charge current direction and low for M transverse to the charge current. In a

simplistic picture, this effect arises from the spin orbit coupling that results in different scattering cross section undergone by the conduction electrons for different magnetization direction $\vec{M}$. The shape of the atomic orbitals depends on the total angular momentum that contains the spin angular momentum. As the magnetization direction rotates from transverse to in plane, the orbitals follows the reorientation of the spin angular momentum due to the spin orbit coupling. When the magnetic field is transverse, the orbitals lie in plane as shown in Figure 1.19 (a) resulting in a low scattering cross section for the conduction electron.

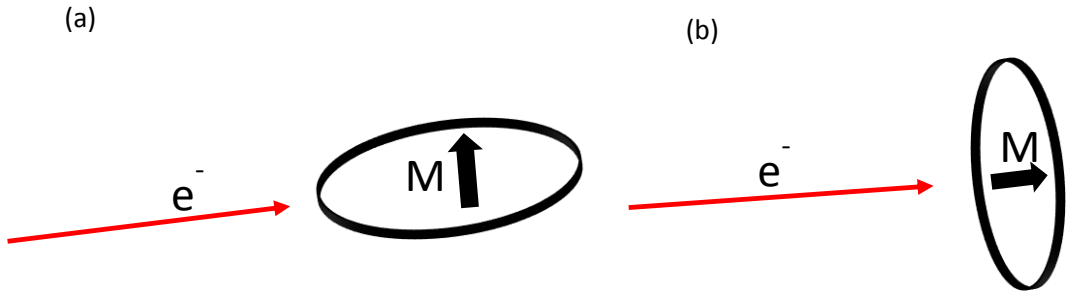

Figure 1.19. (a) Anisotropic Magnetoresistance (AMR) with magnetization perpendicular to the charge current and (b) parallel to the charge current

However, as the magnetic field rotates to the in plane direction, the atomic orbitals become perpendicular to the charge current as shown in Figure 1.19 (b), resulting in an increase of the scattering cross sectional area. Therefore, for transverse magnetization, the resistance is low while for the in-plane magnetization the resistance is high. The resistance for the in-plane and transverse magnetization directions are given by:

$$\rho_{in-plane} = \rho_{\perp} + (\rho_{//} - \rho_{\perp})\, cos^2(\theta) \qquad (20)$$

$$\rho_{transverse} = \frac{(\rho_{//} - \rho_{\perp})}{2} sin^2(\theta) \qquad (21)$$

Where $\rho_{//}$ is the resistivity for $\vec{M}$ parallel to the charge current, $\rho_{\perp}$ is the resistivity for $\vec{M}$ transverse to the charge current and θ is the angle between the magnetization $\vec{M}$ and the charge current. The AMR ratio is given by: $\frac{\Delta\rho}{\rho_0} = \frac{\rho_{//} - \rho_{\perp}}{\rho_0}$

Typically the size the AMR ratio in ferromagnets is 1-2% and gets larger at low temperatures. In Figure 1.20 we show the AMR curve of a Permalloy film. The AMR effect is manifested only if there is a ferromagnetic ordering in the material. In order to understand the effect of AMR on the scattering of conduction electron, we have to employ the two current model and add the spin orbit coupling.

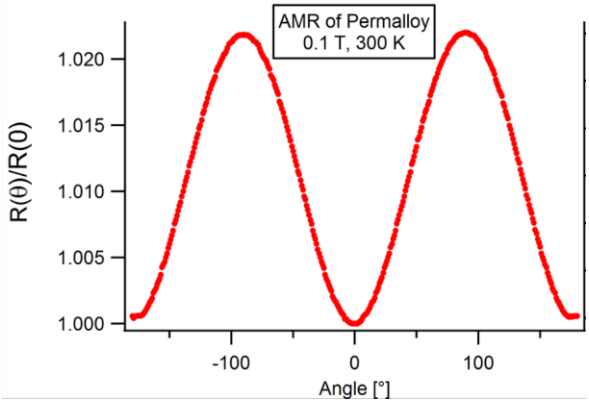

Figure 1.20. (a) AMR of Py film at room temperature

In 3d transition metal, the density of states of spin up electrons is higher than spin down. As shown in Figure 1.1, at the Fermi level all the spin down states are occupied while there are plenty of spin up states available. In ferromagnets, the 4s electrons are responsible of the electric conduction, therefore the resistivity is governed by the scattering of the 4s electrons to the 3d states. It is worthwhile to note that the 4s-3d exchange prohibits

spin flip. Since there are more empty states in the 3d spin up band compared to the spin down, most of the 4s electrons will then scatter to the 3d spin up band. This will result in a two conduction channels for spin and spin down electrons. The effect of spin orbit coupling is to intermix the 3d spin up states with 3d spin down states.

AMR is powerful tool to probe spontaneous magnetization acquired by MPE in nonmagnetic material and will be used to characterize the MPE is FMI/NM system as it will be discussed in Chapter 5.

1.4 Conclusion:

In summary, I have introduced the field of spintronics, starting by focusing on the fundamentals of ferromagnetism to the pioneering work of Albert Fert on GMR. Next, I introduced the fascinating field of graphene spintronics and explained the interplay between different spin relaxation mechanisms in graphene and discussed the different routes to enhance the spin lifetime. This will serve as necessary background information for Chapter 3 where I present my results on the interfacial spin relaxation and spin absorption by a nanomagnet and in Chapter 4 where I demonstrate the presence of an additional contact induced spin relaxation. Furthermore, I introduced the concept of magnetic proximity effect and the different magnetotransport measurement to characterize the MPE. This will be relevant for Chapter 5 where I discuss the MPE in $CoFe_2O_4$/Pt system.

This thesis is organized as follows: In Chapter 2 I discuss the experimental methods of the device fabrication, characterization and measurement techniques. Next, in Chapter 3, I present my work on the investigation of the interfacial spin relaxation and spin

absorption by a nanomagnet in graphene. Next, in Chapter 4 I present my results on the discovery of an additional contact induced spin relaxation in graphene. Chapter 5 presents the first demonstration of MPE in the $CoFe_2O_4$ characterized by AHE, AMR and SMR. Finally, in Chapter 6 I present my results on the growth and transfer of epitaxial 2D semiconductor germanane.

References

1. M. N. Baibich, J. M. Broto, A. Fert, F. N. Van Dau, F. Petroff, P. Etienne, G. Creuzet, A. Friederich, and J. Chazelas, Physical Review Letters 61, 2472 (1988).
2. G. Binasch, P. Gr¨unberg, F. Saurenbach, W. Zinn, et al., Physical Review B 39, 4828 (1989).
3. A. Fert, Reviews of Modern Physics 80, 1517 (2008).
4. J. Stohr and H. C. Siegmann, Magnetism: from fundamentals to nanoscale dynamics, vol. 15 (Springer Heidelberg, 2006).
5. Fert, A., and I. A. Campbell, Phys. Rev. Lett.21, 1190, (1968).
6. Fert, A., and I. A. Campbell, J. Phys. (France) 32, C1-46, (1971).
7. Fert, A., and I. A. Campbell , J. Phys. F: Met. Phys. 6 , 849, (1976).
8. E. Hirota, H. Sakakima, K. Inomata, Giant Magneto-Resistance Devices (Springer, 2002)
9. M. Julliere, Physics Letters A 54, 225 (1975).
10. S. Yuasa, T. Nagahama, A. Fukushima, Y. Suzuki, and K. Ando, Nature Materials 3, 868 (2004).
11. S. S. P. Parkin, C. Kaiser, A. Panchula, P. M. Rice, B. Hughes, M. Samant, and S. H.Yang, Nature Materials 3, 862 (2004).
12. Bowen, M., M. Bibes, A. Barthélémy, J.-P. Contour, A. Anane, Y. Lemaitre, and A. Fert, 2003, Appl. Phys. Lett.82 , 233.
13. S. Datta and B. Das, Applied Physics Letters 56, 665 (1990).
14. M. Johnson and R. H. Silsbee, Physical Review Letters 55, 1790 (1985).
15. S. Takahashi and S. Maekawa, Physical Review B 67, 052409 (2003).
16. F. J. Jedema, H. B. Heersche, A. T. Filip, J. J. Baselmans, B. J. vanWees, et al., Nature 416, 713 (2002).
17. K. S. Novoselov, A. K. Geim, S. V. Morozov, D. Jiang, Y. Zhang, S. V. Dubonos, I. V.Grigorieva, and A. A. Firsov, Science 306, 666 (2004).
18. K. S. Novoselov, A. Mishchenko, A. Carvalho, A. H. Castro Neto, Science 353, 6298 (2016).
19. K. I. Bolotin, F. Ghahari, M. D. Shulman, H. L. Stormer, and P. Kim, Nature 462, 196 (2009).
20. X. Du, I. Skachko, A. Barker, and E. Y. Andrei, Nature Nanotechnology 3, 491 (2008).

21. K. I. Bolotin, K. J. Sikes, Z. Jiang, M. Klima, G. Fudenberg, J. Hone, P. Kim, and H. L. Stormer, Solid State Communications 146, 351 (2008).
22. C. R. Dean, A. F. Young, I. Meric, C. Lee, L. Wang, S. Sorgenfrei, K. Watanabe, T. Taniguchi, P. Kim, K. L. Shepard, et al., Nature Nanotechnology 5, 722 (2010).
23. A. S. Mayorov, R. V. Gorbachev, S. V. Morozov, L. Britnell, R. Jalil, L. A. Ponomarenko, P. Blake, K. S. Novoselov, K. Watanabe, T. Taniguchi, et al., Nano Letters 11, 2396 (2011).
24. D. Huertas-Hernando, F. Guinea, and A. Brataas, Physical Review B 74, 155426 (2006).
25. H. Min, J. E. Hill, N. A. Sinitsyn, B. R. Sahu, L. Kleinman, and A. H. MacDonald, Physical Review B 74, 165310 (2006).
26. Y. Yao, F. Ye, X. L. Qi, S. C. Zhang, and Z. Fang, Physical Review B 75, 041401(R) (2007).
27. S. Chen, Q. Wu, C. Mishra, J. Kang, H. Zhang, K. Cho, W. Cai, A. A. Balandin, and R. S. Ruoff, Nature Materials (2012).
28. D. Pesin and A. H. MacDonald,Nat. Mater.11, 409 (2012).
29. N. Tombros, C. Jozsa, M. Popinciuc, H. T. Jonkman, and B. J. van Wees, Nature 448, 571 (2007).
30. G. Schmidt, D. Ferrand, L. W. Molenkamp, A. T. Flip and B. J. van Wees, Physical Review B 62, R4790 (R) (2000).
31. W. H. Wang, K. Pi, Y. Li, Y. F. Chiang, P. Wei, J. Shi, and R. K. Kawakami, Physical Review B 77, 020402 (2008).
32. W. Han, K. Pi, K. M. McCreary, Y. Li, J. J. I. Wong, A. G. Swartz, and R. K. Kawakami, Physical Review Letters 105, 167202 (2010).
33. W. Han, Ph.D. thesis, University of California, Riverside (2012).
34. W. Amamou, Z. Lin, J. van Baren, S. Turkyilmaz, J. Shi, and R. K. Kawakami, APL Mater. 4, 032503 (2016)
35. W. Han, R. K. Kawakami, M. Gmitra, J. Fabian, Nature Nanotechnology. 9, 794-807 (2014).
36. Elliott, R. J, Phys. Rev.96, 266–279 (1954).
37. Yafet, Y. in Solid State Physics Vol. 14 (eds Seitz F. & Turnbull, D.) 1–98 (Academic, 1963).
38. Dyakonov, M. I. & Perel, V. I, Sov. Phys. Solid State 13, 3023–3026 (1972).

39. D. Kochan, M. Gmitra and J. Fabian, Physical Review Letters 112, 116602 (2014).
40. M. Dro¨gler et al, Nano Letters 16 (6), pp 3533-3539 (2016).
41. J.J. Hauser, Phys. Rev. 187, 580 (1969).
42. E.P. Wohlfarth, J. Phys. Chem. Solids 1, 35 (1956).
43. J. Crangle, Phil. Mag. 5, 335 (1960).
44. S. Ruegg, G. Schutz, P. Fischer, R. Wienke, W.B. Zeper, and H. Ebert, J. Appl. Phys. 69, 5655 (1991).
45. S.K. Saha, V.S. Stepanyuk, and J. Kirschner, Phys. Lett. A 378, 3642 (2014).
46. B.N. Cox, R.A. Tahir-Kheli, and R.J. Elliott, Phys. Rev. B 20, 2864 (1979).
47. M.A. Ruderman, and C. Kittel, Phys. Rev. 96, 99 (1954).
48. T. Kasuya, Prog. Theor. Phys. 16, 45 (1956).
49. K. Yosida, Phys. Rev. 106, 893 (1957).
50. S. Blugel, B. Drittler, R. Zeller, and P.H. Dederichs, Appl. Phys. A 49, 547 (1989).
51. W. E. Bailey, A. Ghosh, S. Auffret, E. Gautier, U. Ebels, F. Wilhelm, and A. Rogalev, Physical Review B 86, 144403 (2012).
52. S. Singh, J. Katoch, T. Zhu, K. Meng, T. Liu, J. T. Brangham, F. Y. Yang, M. Flatte and R. K. Kawakami, arXiv: 1610. 08017 (2016).
53. Z. Wang, C. Tang, R. Sachs, Y. Barlas, and J. Shi, Phys. Rev. Lett. 114, 016603 (2015).
54. J. C. Leutenantsmeyer, A. A. Kaverzin, M. Wojtaszek and B. J. van Wees, 2D Materials, 4. 014001 (2016).
55. P. Wei et al., Nature Materials. 10, 1038 (2016).
56. C. Zhao et al., arXiv 1610. 10, 1038 (2016).
57. S. Y. Huang, X. Fan, D. Qu, Y. P. Chen, W. G. Wang, J. Wu, T. Y. Chen, J. Q. Xiao and C. L. Chien, Phys. Rev. Lett. 109, 107204 (2012).
58. Y. M. Lu, Y. Choi, C. M. Ortega, X. M. Cheng, J. W. Cai, S. Y. Huang, L. Sun and C. L. Chien, Phys. Rev. Lett. 110, 147207 (2013).
59. S. Geprägs, S. Meyer, S. Altmannshofer, M. Opel, F. Wilhelm, A. Rogalev, R. Gross, and S. T. B. Goennenwein, Appl. Phys. Lett. 101, 262407 (2012)

60. Y. Chen, S. Takahashi, H. Nakayama, M. Athammer, S. T. B. Goennenwein, E. Saitoh and G. E. W. Bauer, Physical Review B 87, 144411 (2013).
61. Mott, N. F., Proc. R. Soc. A 124, 425 (1929).
62. Dyakonov, M., and V. I. Perel, Zh. Eksp. Teor. Fiz. 13, 657 (1971).
63. L. Liu, C. Pai, H. W. Tseng, D. C. Ralph and R. A. Buhrman, Science 6081, pp 555-558 (2012).
64. Y.K. Kato, R.C. Myers, A.C. Gossard, D.D. Awschalom, Science, 306, 1910 (2004).
65. L. Berger, Physical. Review. B 2, 4559 (1970).
66. P. Nozieres, and C. Lewiner, J. Phys. (Paris) 34, 901 (1973).

Chapter 2: Experimental Methods

Introduction:

In this chapter I discuss the device fabrication technique of graphene spin valves, $CoFe_2O_4$/ Pt Hall bars and germanane photoconductivity devices. In addition, I present the different measurement techniques used throughout this thesis to characterize spin, charge transport and magnetic properties.

2.1 Graphene spin valve fabrication:

The studies discussed in Chapter 3 and 4 use graphene spin valve devices to investigate the interfacial spin relaxation, spin absorption and contact induced spin relaxation. The device fabrication procedure is outlined below.

2.1.1 Substrate preparation:

The graphene used for the spin transport studies is exfoliated onto SiO_2/Si substrate. The SiO_2 is obtained by thermal oxidation of Si that produces 300 nm SiO_2. The SiO_2 was purchased from University Wafers. The Si/SiO_2 wafers are cleaved approximately to about 10 mm x 10 mm samples. The samples are cleaned in three steps:

- Ultrasonic cleaning in a bath of Acetone for 15 min (repeat twice)
- Ultrasonic cleaning in IPA for 15 min
- Blow dry the samples and anneal at 150 ℃ for 30 min

2.1.2 Graphene exfoliation:

The graphene used for these studies was exfoliated from a Highly Oriented Pyrolytic Graphite (HOPG) purchased from SPI supplies. First, drape scotch tape on the

HOPG surface gently and apply pressure uniformly on the surface and peel off the scotch tape carefully. Second, secure the scotch tape on a glass slide. Third, place another scotch tape on top of the previous one and apply pressure very gently uniformly. Too much pressure will crack the graphite pieces resulting in small graphene pieces, while very low pressure will result in no graphene deposition. Fourth, peel off gently, fold and peel until the color of the graphite area on the scotch tape become light grey. Finally, place the scotch tape on the SiO_2 wafer and gently apply pressure with a flat tweezer uniformly then peel off carefully. After exfoliation, inspect the sample surface with an optical microscope until identification of a suitable graphene flake. Below is the optical microscope picture of graphene with multiple thicknesses.

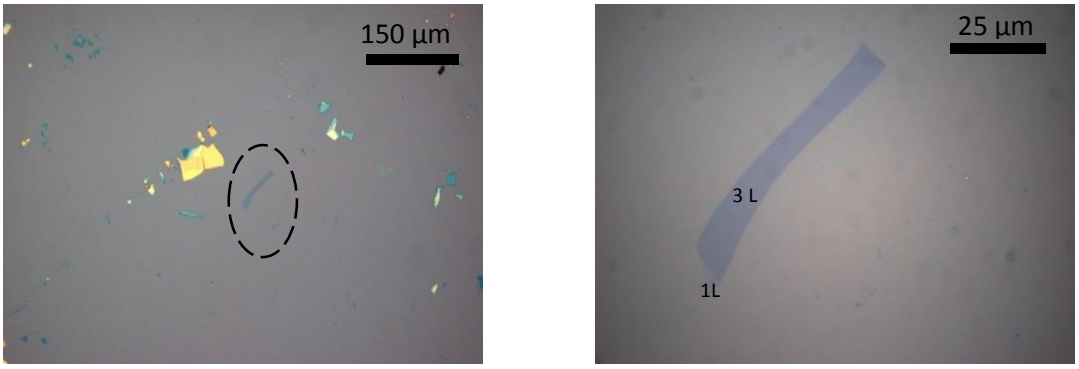

Figure 2.1. Microscope image of graphene on SiO_2

2.1.3 Alignment marks:

E-beam lithography is used to define the metallic electrodes for electrical contact. In order to locate the graphene flake on the wafer, we write alignment marks that consists of 4 matrices of 1 mm x 1 mm each made of crosses separated by 50 µm and numbers

separated by 500 μm. In order to locate the graphene in the matrix, we need to identify the closest number to the graphene flake and measure the distance between the graphene and the number using the crosses as shown in Figure 2.2.

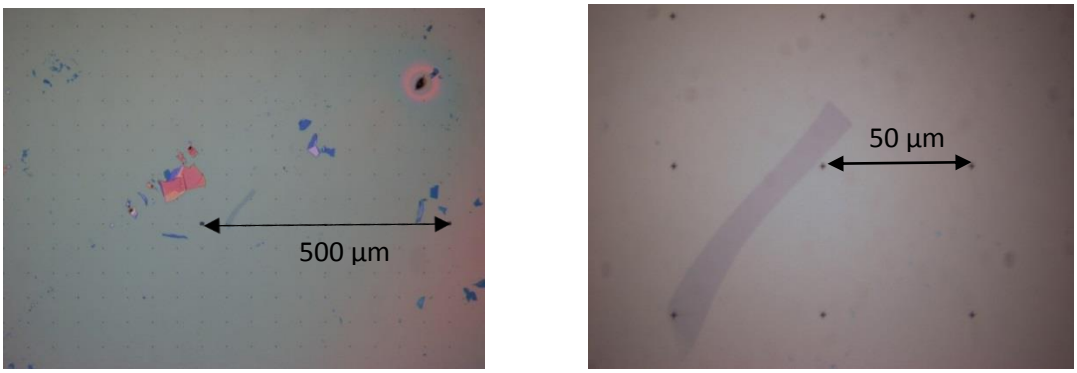

Figure 2.2 Microscope image of alignment marks

The steps to write alignment marks are described below:

- First, spin coat MMA at 3000 rpm for 45 seconds and bake at 150℃ for 2 min
- Second, spin coat PMMA at 3000 rpm for 45 seconds and bake at 170 C for 5 min
- Make a scratch on the top corner of the sample and deposit gold nanoparticles (100 nm diameter) using a syringe. The gold nanoparticles will allow to optimize the focus of the electron beam for writing the alignment marks later
- Load the sample to the e-beam lithography machine and correct the stigmation and focus by focusing on the gold nanoparticles.
- Once focused, write the alignment marks as designed in the CAD file.
- Unload the sample and develop in MIBK: IPA 1:3 for 1m20s and submerge in IPA for 1m and finally rinse in water for 20 s then blow and dry with nitrogen gas.

2.1.4 Writing the electrodes:

First, microscope pictures of the flake at 10x and 60x are taken and uploaded to the CAD software. Next, electrodes with specific dimensions are designed using the CAD software with the correct distances and features. After design, we create an NPGS file that communicates with the e-beam machine to write the electrodes. Next, we load the sample to the SEM, locate the flake using the alignment marks and write the electrodes. The pattern is then developed using the previous recipe.

2.1.5 Tunneling contacts deposition:

Due to the conductance mismatch between the Co and Graphene, tunneling contact for spin injection and detection are used. Below we describe the tunnel contact fabrication:

2.1.5.1 Co/SrO tunneling contact:

For the study in Chapter 3, SrO/Co masking layer are used to inject and detect spins. The tunnel contacts are grown inside a molecular beam epitaxy (MBE) chamber at 1×10^{-10} T. The growth recipe is described below:

- Leak molecular oxygen O_2 at 3×10^{-7} T
- First, grow 0.55 nm Sr at 9° angle (Figure 2.3 (a))
- Second, grow 2.11 nm Sr at 0° angle (Figure 2.3 (a))
- Third, oxidize for 3h at 3×10^{-7} T
- Grow 60 nm Co at 7° angle and cap with aluminum

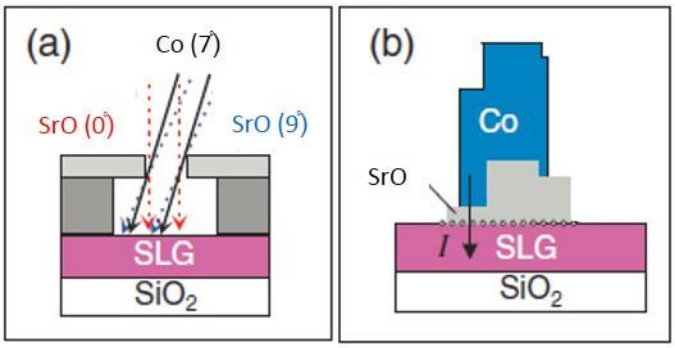

Figure 2.3 (a) Angular growth of SrO tunnel barrier and Co (b) Schematic of the current injection path

2.1.5.2 Co/MgO tunneling contact:

In Chapter 4, we use MgO/TiO_2 and Al_2O_3 tunneling contacts to study the contact induced spin relaxation. The MgO/TiO_2 are grown as follows:

- Grow 0.14 nm of Ti at 0° and 9° (Figure 2.4 (a))
- Leak in molecular O_2 at 3×10^{-7} T for 30 min
- Deposit 3 nm MgO at 0° and 0.8 nm at 9 °
- Third, oxidize for 3h at 3×10^{-7} T
- Grow 90 nm Co at 7° angle and cap with aluminum

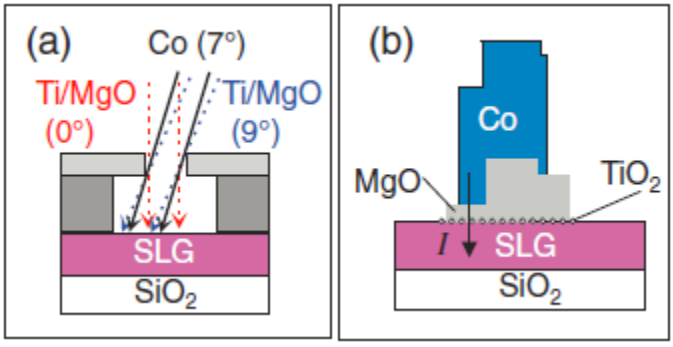

Figure 2.4 (a) Angular growth of Ti/MgO tunnel barrier and Co (b) Schematic of the current injection path

2.1.5.3 Co/Al_2O_3 tunneling contact:

- Sputter 0.7 nm of Al blanket on top of graphene
- Oxidize in molecular oxygen at atmospheric pressure
- Define the electrodes with e-beam lithography
- Grow 80 nm Co at 0° using MBE
- Cap with e-beam evaporated Al_2O_3

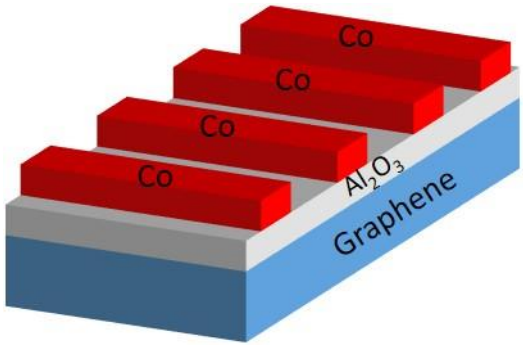

Figure 2.5 Schematic of graphene spin valve with Al_2O_3 tunnel barrier

2.1.6 Lift-off:

After evaporation of the tunnel contacts, the device is immersed in PG Remover at 70° C for 1h, then submerged in IPA for 2 min and blow dried using nitrogen gas.

2.1.7 Graphene spin valve electrical measurement:

For all the graphene spin valve measurement a lock-in detection technique was used in order to obtain the best signal to noise ratio. The schematic of the measurement is shown in Figure 2.6. A current source Keithley 6221 is used to apply an AC charge current at a

frequency of 11 Hz and is referenced to a 7265 Lock-In amplifier. The voltage is amplified using SR-560 and fed to the Lock-In for voltage measurement. The gate voltage is applied to a Si back gate using a Keithley 2400 for gate dependence measurement.

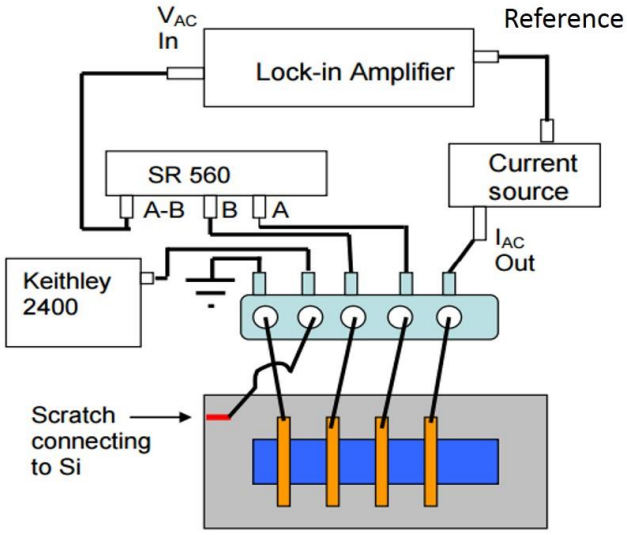

Figure 2.6 Non-local measurement electrical setup

2.2 In-situ MBE chamber:

The study in Chapter 3 is done inside an MBE chamber at 1×10^{-10} T, that has the capability to grow magnetic thin films and perform non-local spin valve measurement at variable temperature ranging from 20 k to 300 k without breaking the vacuum. This unique capability will allow us to investigate the interfacial spin dephasing as it will be discussed in Chapter 3.

First, the spin valve device is placed on a sample paddle as shown in Figure 2.7 (a) and electrical contacts are made by wirebonding the device pads to the 6 Au pads in the paddle. Then, the paddle is mounted on a vacuum puck (Figure 2.7 (b)) and loaded inside

the MBE chamber. Next, the paddle is transferred from the puck to the cryostat inside a small MBE chamber as shown in Figure 2.8. In order to electrically contact the Au pads on the paddle, a set of 6 Au pins are lowered by rotating a key until the pins touch the pads.

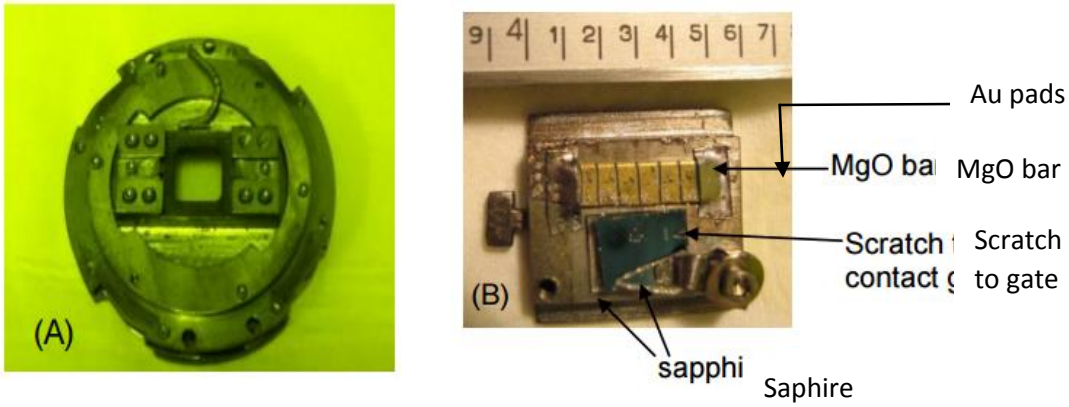

Figure 2.7 (a) In-situ puck (b) Sample paddle with electrical pins

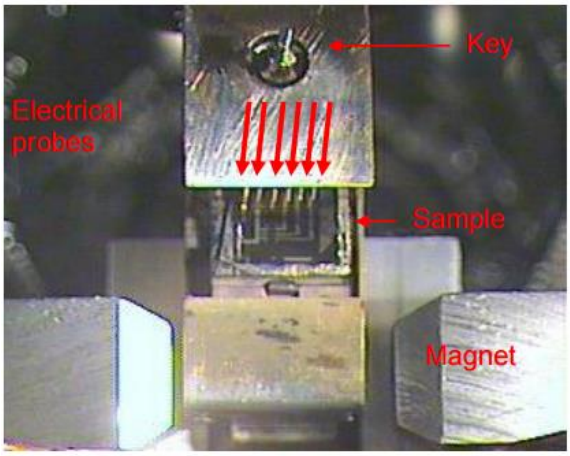

Figure 2.8 In-situ measurement system

For magnetotransport measurement, the magnetic field is applied by lowering the device to the magnet position. In Figure 2.8, we show the two magnetic poles of the magnet. The chamber contains Fe and Cu effusion cells with individual shutters, deposition crystal monitor, sputtering gun, hydrogen cracker and oxygen leak valve.

2.3 Pt/CFO Hall bar fabrication:

In Chapter 5, magnetotransport measurement of Pt/CFO are done using a Hall bar device. The Hall fabrication procedure is described below:

- Spin coat photoresist on top of the film Pt/CFO at 4500 rpm for 45 s and bake for 2 min at 100 ℃.
- Load the sample into a photolithography system
- Expose the pattern with UV light
- Develop the pattern for 1min 20s
- Etch the developed area using Ar ion gas
- Lift off in Acetone at 70℃ for 1h

Below is the Hall bar geometry used for magnetotransport measurement:

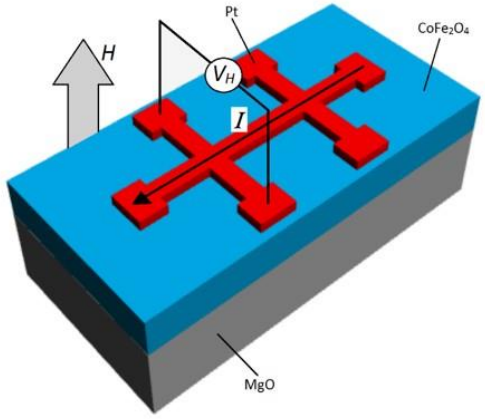

Figure 2.9 Hall bar geometry and electrical connections

2.4 Large area germanane device fabrication:

In Chapter 6, we perform photoconductivity measurement to characterize the band gap and photocurrent on/off ratio of large area germanane. The device fabrication procedure is described below:

- Place a 20 μm diameter wire at the center of the sample
- Cover the edges with Kapton tape leaving only a small portion of the sample exposed
- Evaporate Au/Ti everywhere on the sample
- Peel off the tape and the wire in the middle of the sample

The resulting device will have a 20 μm channel width and Au/Ti pads for wirebond.

Chapter 3: Investigation of Interfacial Spin Relaxation and Spin Absorption in Graphene Spin Valves

Abstract:

We investigate the feasibility for achieving magnetization switching of a nanomagnet using graphene as a nonmagnetic channel material for All Spin Logic (ASL) applications. Using *in-situ* MBE deposition of nanomagnet on graphene spin valve, we demonstrate the presence of an interfacial spin dephasing at the interface between graphene and the nanomagnet. By introducing a Cu spacer between the nanomagnet and graphene, we demonstrate that this interfacial effect is related to an exchange interaction between the spin current and the disordered magnetic moment of the nanomagnet at the interface. In addition to the newly discovered interfacial spin relaxation effect, the extracted contact resistance area product of the nanomagnet/graphene interface is relatively high. In practice, reducing the contact resistance will be as important as eliminating the interfacial relaxation in order to achieve magnetization switching.

3.1 Introduction:

Graphene is a promising material for lateral spin transport due to its low spin orbit coupling and high carrier mobility, leading to long spin diffusion lengths at room temperature [1-3]. The ferromagnet (FM)/graphene interface plays a critical role in lateral spin transport devices, yet the spin-dependent properties of such interfaces are not well understood. It has been established theoretically and experimentally by several groups that the contact at the ferromagnet/graphene interface is the bottleneck for achieving high spin lifetimes and high spin injection efficiency due to spin absorption by the ferromagnetic contact, which is known as the conductivity mismatch problem [4-7]. Early work on graphene spintronics employed high resistance Al_2O_3 barriers with unintentional pinholes to circumvent the conductivity mismatch problem [8]. Although the Al_2O_3 barrier resistance was significantly higher than the graphene spin resistance, the obtained spin lifetimes were still in the low range of hundreds of picoseconds. Later, Han et al [6] achieved tunneling spin injection using pinhole-free Ti-seeded MgO barriers, leading to substantially longer spin lifetimes in the nanosecond range. This suggests that conductance mismatch is not the only source of spin relaxation at the contact. Subsequently, Volmer et al [6] increased the spin lifetime from hundreds of picoseconds to 1 ns in single layer graphene by successive oxidation of a Co/MgO pinhole contact. It was suggested that the oxidation process suppresses the direct contact between Co and graphene by oxidizing the Co layer at the pinholes, which may reduce sp^3 hybridization between the Co and carbon atoms responsible for spin scattering. However, the microscopic origin of such possible interfacial effects remains unclear.

Addressing spin relaxation at FM/graphene junctions is not only important from a fundamental point of view, but also for technological applications such as "All Spin Logic" (ASL) that has been proposed recently by the Datta group [9]. This architecture relies on the magnetization switching of a nanomagnet using spin transfer torque exerted by a pure spin current absorbed by the nanomagnet. This task has been challenging to achieve in graphene. Lin et al [10] have shown spin transfer torque switching in graphene, but it required the assistance of a substantial external magnetic field and relatively high injection current of up to 4.5 mA in multilayer graphene. Later, they were able to decrease the injection current to 4 mA by using transparent contacts to the FM electrode [11]. Nevertheless, the use of such high injection current is detrimental as Joule heating can cause damage to the FM/tunnel barrier contact. Furthermore, using an external magnetic field is not practical for device operation. This contrast between the exceptional spin transport properties of graphene and the low spin transfer torque switching efficiency is quite puzzling. It is therefore of paramount importance to understand interface spin relaxation and spin absorption at the FM/graphene interface.

Motivated by these considerations, we designed *in-situ* spin transport experiment shown in Figure 3.1. A nanomagnetic island is grown on the surface of a graphene spin valve by cryogenic molecular beam epitaxy (MBE) while the spin transport is monitored during the deposition. The presence of the nanomagnet on top of the graphene channel can introduce additional spin-dependent interactions to produce spin scattering and/or spin absorption, which can be quantified by measuring the change of the nonlocal spin transport signal as a function of nanomagnet thickness. Due to the atomic scale precision of MBE

growth, this provides a powerful and systematic method to investigate the spin-dependent properties of FM/graphene interfaces.

Here, we report the discovery of an interfacial spin relaxation process at FM/graphene junctions due to interactions of spin-polarized conduction electrons with interfacial magnetic moments. This interfacial spin relaxation could be either due to a transfer of spin angular momentum from the electron spins in graphene to the interfacial magnetic moments (i.e. interfacial spin transfer torque) or due to depolarization of electron spins in graphene by a fluctuating exchange field [12]. We also observe the expected bulk-like spin absorption associated with spin relaxation in the bulk of the magnetic island. These conclusions are established through *in-situ* spin transport experiments, where a Fe nanomagnet is grown on the interior of a wider multilayer graphene spin valve and produces a rapid decay of nonlocal spin transport signal in the submonolayer regime of Fe thickness. Insertion of an ultrathin Cu layer on graphene prior to Fe deposition provides the key insight on the interfacial origin of the spin relaxation process. In addition, we employ finite element modeling of spin transport to quantify the interfacial spin relaxation, bulk-like spin absorption, and the spin current flowing into the nanomagnet. These results indicate that atomic-scale engineering of the FM/graphene interface is important for achieving efficient spin transfer torque switching of nanomagnets on graphene.

3.2 Experimental methods:

The experiments are conducted in an ultrahigh vacuum (UHV) chamber with the ability to perform *in-situ* spin transport measurements while depositing metallic adatoms onto graphene spin valves held at cryogenic temperatures (~20 K). For the fabrication of

spin valve devices, we exfoliate multilayer graphene flakes onto SiO_2 (300 nm)/Si wafers, where the degenerately doped Si is used as a backgate. The graphene thickness is screened by optical contrast and quantified by atomic force microscopy (AFM). We utilize a single e-beam lithography pattern using bilayer PMMA/MMA resist combined with angle evaporations to define a SrO tunnel barrier and 60 nm thick Co electrodes. The angle evaporation results in a small contact width of ~50 nm between the Co and graphene through a narrow layer of SrO. Subsequently we spin coat the spin valve device with PMMA and perform a soft bake at 50 °C for 2h in order to prevent damaging the Co/SrO electrodes. After the bake, we create an opening in the PMMA for the island deposition by patterning using e-beam lithography and developing in MIBK/IPA for 1m 20s. Immediately after development, the sample is loaded into the UHV chamber to perform the non-local spin transport measurement and growth of the Fe and Cu islands by cryogenic MBE at a pressure of 1×10^{-11} Torr. For island growth, we utilize thermal effusion cells and the growth rate is measured using a quartz crystal monitor. Typical growth rates are 0.04 Å/min for Fe and 0.2 Å/min for Cu. The samples are held at low temperatures (~20 K) during growth in order to inhibit the lateral surface diffusion of the metallic adatoms on graphene. In Figure 3.1 (a) we show the schematic of the final device. The SEM picture of the device after island growth and lift off is shown in Figure 3.2 (b)

(a)

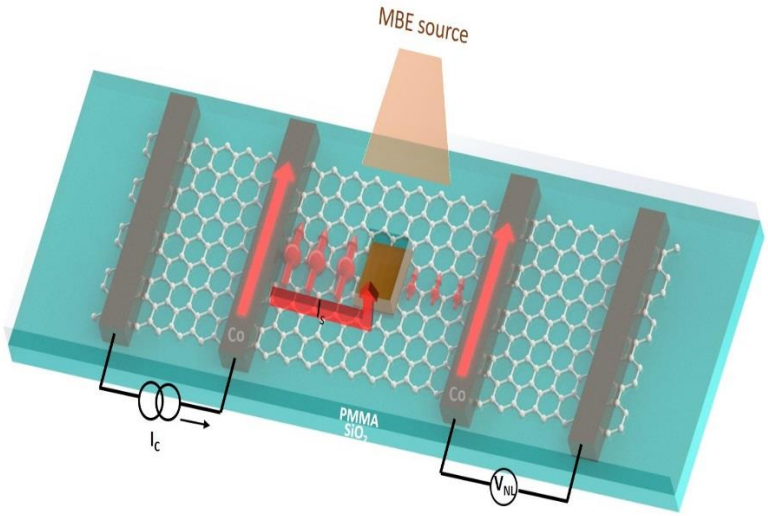

(b)

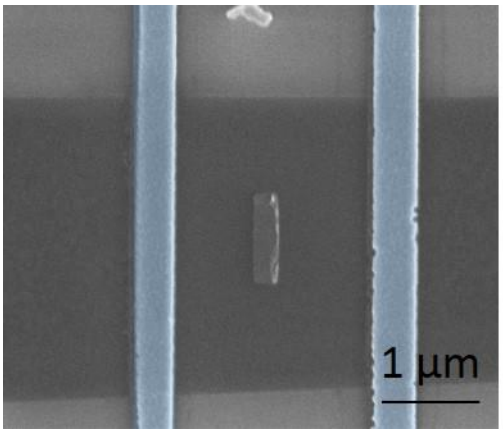

Figure 3.1 (a) Schematic of the the spin absorption device (b) SEM image of the Fe/Gr island and Co/SrO injector and detector

3.3 Results and discussion:

3.3.1 Non-local measurement prior to Fe deposition:

Prior to island deposition, we measure the charge and spin transport characteristics of our multilayer graphene (MLG) spin valve devices. We present data for representative devices which illustrate phenomena observed consistently in a sample set comprised of 4 Fe/graphene and 4 Fe/Cu/graphene island devices. Spin transport measurements are carried out using lock-in detection with an AC injection current of I_{INJ} = 5 μA rms at 11 Hz between contacts E1 and E2 (injector) (see Fig. 3.2a inset). Electron spin density injected at E2 diffuses toward electrode E3 (detector), which generates a nonlocal voltage V_{NL} measured between E3 and E4. For this sample, the width of the graphene is W_{Gr} = 2.5 μm and the spacing between E2 and E3 is L = 1.5 μm. We evaluate spin transport by measuring the non-local voltage as a function of the applied in-plane magnetic field [13]. The non-local magnetoresistance (MR) signal of the pristine graphene is shown in Figure 3.2 (a) for a backgate voltage of V_G = 0 V. We observe a sharp switching corresponding to the transition between parallel and antiparallel configurations of the injector and detector magnetizations. The size of the non-local MR in this particular case is: ΔR_{NL} = 2.75 Ω as shown in Figure 3.2 (a). Next, we perform a non-local Hanle spin precession measurement to extract the spin lifetime and diffusion constant for the MLG. For Hanle measurements, an out of plane magnetic field is ramped while measuring V_{NL} with electrodes in the parallel and antiparallel magnetization states. The Hanle curves obtained for parallel and antiparallel configurations are shown in Figure 3.2 (b). We fit the Hanle curve by

subtracting the corresponding nonlocal voltages in the parallel and antiparallel configurations and using the modified Bloch equation that takes in account the effect of spin absorption by the Co/SrO contacts [14]. Using a three terminal measurement scheme, we determine the contact resistance of the injector and detector to be 85 kΩ and 23 kΩ, respectively. Using these contact resistance values, we fit the Hanle curves and obtain a spin lifetime of τ_s = 551 ps, a diffusion constant of D = 0.0035 m^2/s and a spin injection efficiency α= 11%.

3.1.2 Non-local measurement with Fe deposition:

To investigate the effect of a nanomagnetic Fe island on the spin transport in graphene, we deposit Fe through the PMMA mask to produce the device geometry shown in Figure 3.1 (a).

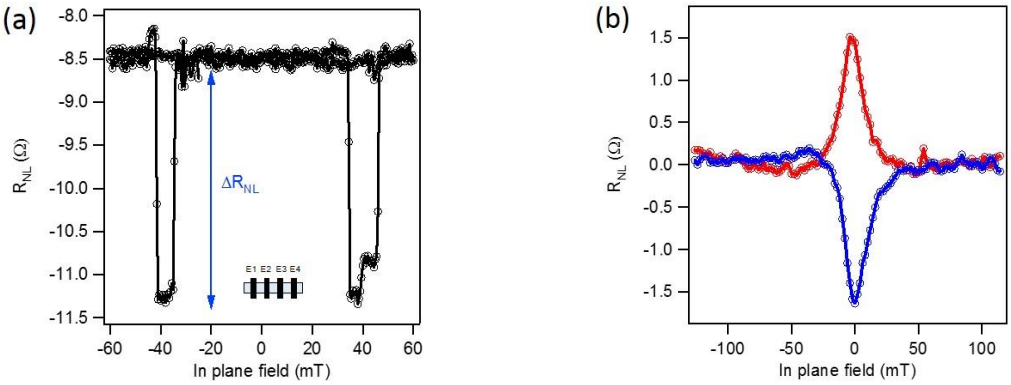

Figure 3.2 (a) Non-local MR and (b) Non-local Hanle for pristine graphene prior to Fe deposition

The width of the Fe island relative to the graphene width plays an important role in determining the spin signal that can be detected. Using a large island size will limit the detected spin signal at the cobalt detector (E3) due to spin absorption and/or dephasing

from the island. For samples A, B, and C, the width of the Fe island is W_{Island} = 560 nm (and length is 200 nm) which is ~30% of the graphene channel width (W_{Gr} = 2.0 μm). For sample D, W_{island}/W_{Gr} is ~90%. Figures 3.3 (a) and 3.3 (b) shows representative nonlocal MR loops and Hanle curves, respectively, for different Fe thicknesses. The initial gate voltage of V_G = 0 V is adjusted slightly (within ± 5V) at each Fe thickness to maintain a constant channel resistance to offset any charge transfer effects that could occur upon metal doping [15, 16]. We observe two striking features. First, the non-local MR decreases by 30% for Fe thicknesses as low as 0.04 Å and continues to decrease, reaching a value of ΔR_{NL}= 0.8 Ω for 23.4 Å of Fe which is 70 % smaller than the spin signal prior to deposition. Second, the Hanle curve becomes broader as the Fe thickness is increased, with the effective spin lifetime decreasing to τ^*_s = 330 ps after 23.4 Å of Fe. The fitted values of the diffusion constant D = 0.003 m^2/s and α = 11% change little compared to the pristine graphene case, which suggests that the decrease of the non-local MR after Fe deposition is due to extra spin induced by the Fe island, as opposed to a change in the spin injection efficiency or graphene conductance.

Figure 3.3 (c) summarizes the decrease of the non-local MR for all Fe thicknesses, where we define $\gamma=\Delta R_{NL}/\Delta R_{Pristine}$, where $\Delta R_{Pristine}$ is the non-local MR of the pristine graphene before any Fe deposition.

(a)

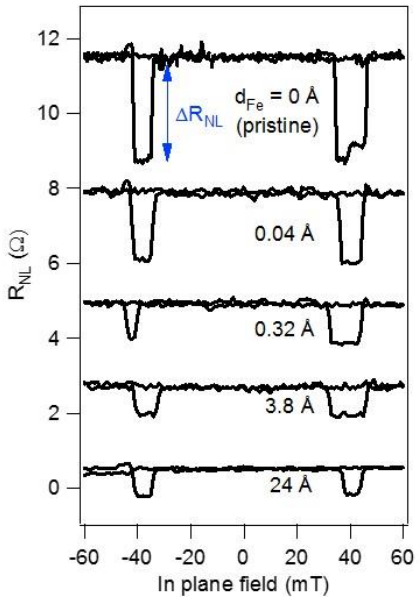

(b)

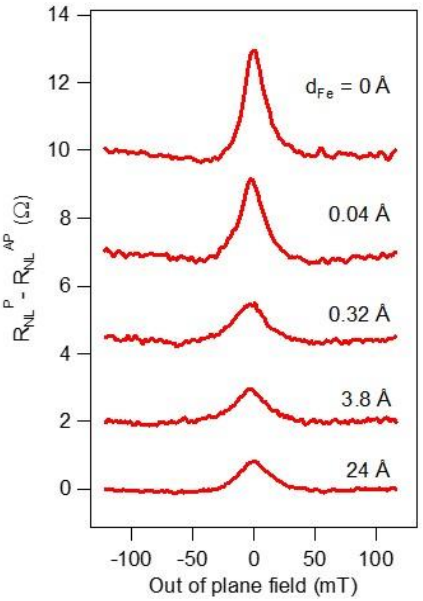

(c)

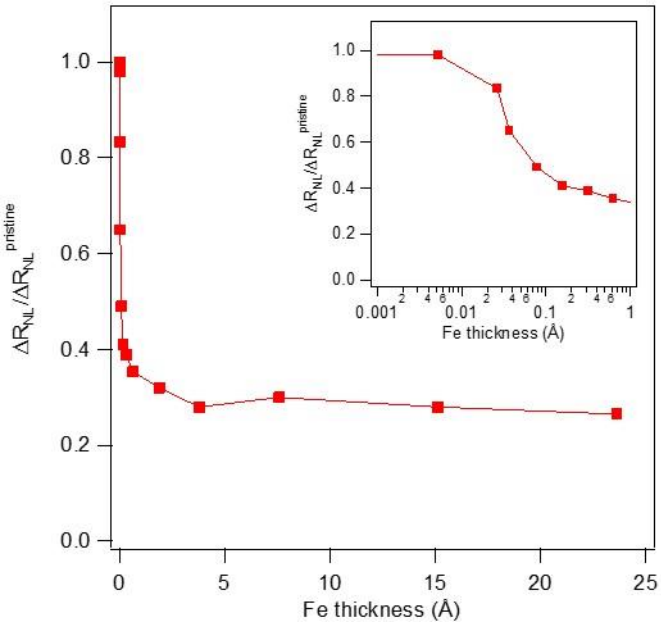

Figure 3.3 (a) Non-local MR for different Fe thickness (b) Non-local Hanle for different Fe thickness (c) Normalized non-local resistance with Fe thickness

We observe two distinct length scales: (i) γ decreases rapidly for Fe thicknesses lower than a monolayer (ML)—we take 1 ML = 1.48 Å, which is the value for (100) oriented Fe, even though the deposited Fe is unlikely to grow layer by layer [17, 18](ii) For high Fe thickness > 1 ML, γ decreases at slower rate. As discussed below, we find that the initial decrease in ΔR_{NL} at thicknesses of less than 1 ML is due to increasing coverage of the island by Fe.

Bulk spin absorption, which is useful for switching a magnetization by spin transfer torque, applies only to magnets with thicknesses greater than or equal to the spin diffusion length [19]. Estimates for the spin diffusion length in Fe vary from 2 nm to 8.5 nm [20, 21]. Since we observe a decrease of ΔR_{NL} at much smaller Fe thicknesses, we conclude that this cannot be due to bulk-like spin absorption by the Fe island, and we therefore suspect an interfacial spin relaxation effect.

Physically, there are a number of possible sources of interfacial spin relaxation including: (i) spin momentum transfer between the spin current and interfacial magnetic moments, (ii) interfacial magnetic moments causing spin dephasing via static or fluctuating exchange fields [12] (i.e. induced magnetism), (iii) sp^3 hybridization between the ferromagnet and C atoms [22-25], (iv) spin relaxation based on SOC induced by the metal overlayer (proximity induced SOC, or SOC of the overlayer) [26]. Of these possibilities, (i) and (ii) are based on magnetism, while the others are not. Our primary goal, therefore, is to understand whether (or not) the interfacial spin relaxation Γ_{int} is related to the magnetic property of the Fe island.

3.1.3 Spin absorption by Cu island:

To address this question, our approach is to insert a thin Cu layer into the Fe/Gr interface. This is an established method for elucidating the role of interface effects in spintronic systems, and we furthermore chose Cu due to its low atomic number and compatibility with our cryogenic molecular beam epitaxy system. To establish the suitability of Cu for our studies, we deposit a 3 nm Cu island on graphene under the same conditions as the Fe experiment, including island/graphene width ratio, graphene thickness and deposition temperature. In Figure 3.4 (a), we show the dependence of the spin signal on the Cu thickness. Interestingly, we observe that the signal remains almost unchanged for very low Cu coverage and even increases slightly. The origin of this increase is not currently understood and is beyond the scope of this study. The spin current remains largely unaffected by the presence of 3 nm of Cu, which allows it to be used to decouple the Fe from the graphene without reducing the spin current. In Figure 4 (a), we show the results for Fe deposited on 3 nm Cu spacer (green curve). We observe two interesting features: First, we still measure a rapid drop at submonolayer thickness but with lower magnitude compared to the Fe/Gr direct contact. Second, we clearly see the slower exponential decay for higher Fe thickness that was otherwise hard to distinguish in the Fe/Gr experiment. The fact that we observe similar rapid decay compared to the Fe/Gr direct contact suggests the possibility that the Fe is directly contacting the graphene through pinholes. Therefore, we performed AFM on the 3 nm Cu spacer shown in Figure 3.4 (b) to verify the presence or the absence of such pinhole structure. Although the AFM shows a rough Cu surface, the

line cut shows no pinholes propagating all the way down do the graphene surface. This observation indicates that the rapid decay in the Fe/Cu/graphene is not related to direct contact between the Fe and graphene through pinholes in the Cu.

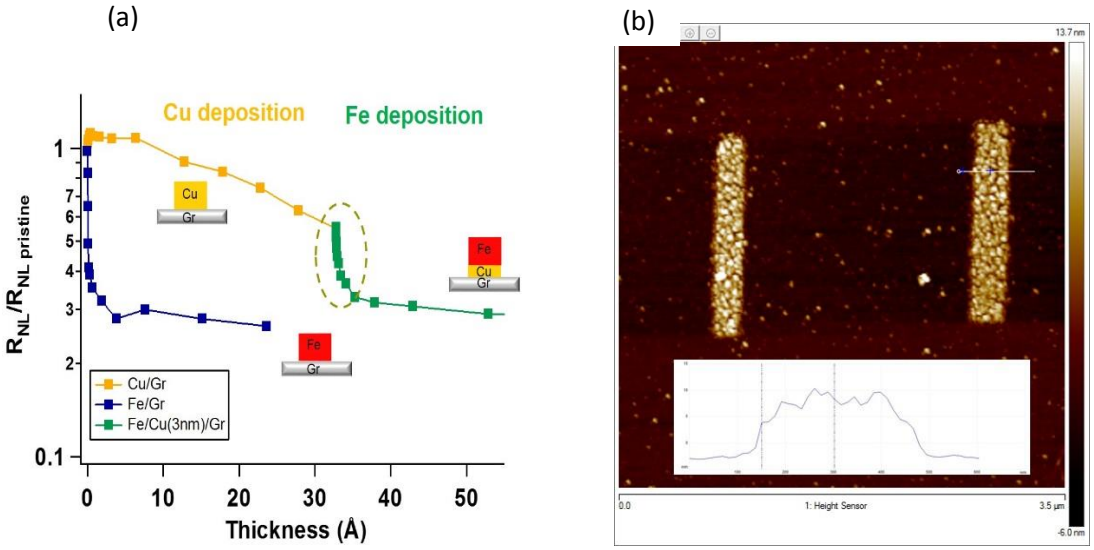

Figure 3.4 (a) Normalized non-local MR for Cu (orange curve), Fe (blue curve) and Fe/Cu (green curve) islands with thickness (b) AFM image of 3 nm Cu

3.1.4 2D Finite element modeling of spin absorption:

We introduce a finite element model in order to quantitatively describe the measured decrease in ΔR_{NL} as a local increase in the spin relaxation rate under the island. A 2-D environment (typically composed of 25 nm x 25 nm cells) shown in Figure 3.5 is used to model the spin accumulation $\vec{S}(x,y)$, which is the spin splitting of the chemical potential $\mu_\uparrow - \mu_\downarrow$ in the three cardinal directions ($i = x,y,z$), throughout the graphene channel. A forward Euler step algorithm with Neumann boundary conditions is used to

evolve the distributed spin accumulation until steady state in accordance with spin diffusion, precession, and relaxation,

$$\frac{\partial \vec{S}}{\partial t} = D\nabla^2\vec{S} - \gamma\vec{B}\times\vec{S} - \frac{\vec{S}}{\tau_s} + \dot{\vec{S}}_0 \qquad (1)$$

where $\gamma = 1.76 \times 10^{-2}$ Oe^{-1}ns^{-1} is the gyromagnetic ratio, $\vec{B}$ is the applied magnetic field, and $\dot{\vec{S}}_0$ is the rate of spin injection.

(a) (b)

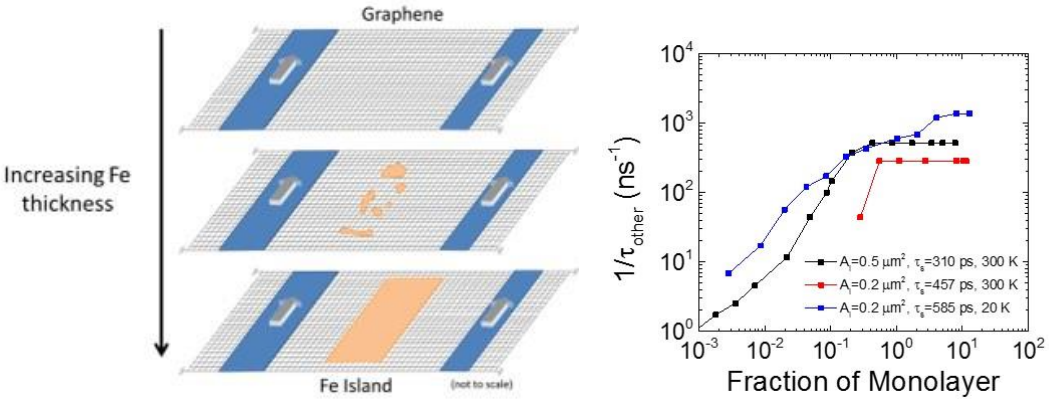

Figure 3.5 (a) Evolution of Fe islands with thickness (b) Relaxation rate extracted using 2D finite element modeling for different thicknesses

This spin injection rate, which is calculated from the known injection charge current density and the fitted value of α, is assumed to be parallel to the injector magnetization and is only nonzero under the injector contact. Spin absorption into the Co contacts is incorporated by locally increasing the spin relaxation rate under the Co contacts by an additional spin relaxation term $\tau^{-1} = R_{sq}\lambda^2/(R_C A\tau_s)$, where $\lambda = \sqrt{D\tau_s}$, R_C is the measured Co/SrO/graphene contact resistance, and A is the contact area. The simulation is compared to experiment by first considering the component of the spin accumulation

parallel to the detector magnetization ($S_y = \vec{S} \cdot \widehat{M}_{det}$), and then calculating the spin valve signal size $(\Delta R_{NL})_{model} = \alpha \langle S_y \rangle_{det} / I$, where I is the injection charge current and $\langle S_y \rangle_{det}$ is the average of S_y in all of the cells underneath the detector contact. The model is verified by confirming that the out-of-plane magnetic field dependence of $(\Delta R_{NL})_{model}$ is consistent with the nonlocal Hanle data measured prior to metal deposition. Next, in only the cells under the island, an additional spin relaxation term τ_{other}^{-1} is included such that the spin relaxation rate is locally increased

$$\tau_s^{-1} \rightarrow \tau_s^{-1} + \tau_{other}^{-1} \qquad (2)$$

For all Fe thicknesses, a value of τ_{other}^{-1} was found that reproduced the measured value of ΔR_{NL}, thus allowing the measured thickness dependence of ΔR_{NL} to be mapped to a thickness-dependent additional local spin relaxation rate τ_{other}^{-1}.

In Figure 3.5 (b) we show the extracted values for the additional local spin relaxation rate τ_{other}^{-1} as a function of Fe thickness. This rate increases linearly with Fe thickness in the submonolayer regime and plateaus at a thickness of ~1 ML of Fe, which we interpret in terms of increasing areal coverage of Fe. The perceived submonolayer thickness dependence is due to the increasing island size at early stages of growth, as observed in previous STM studies [17, 18], such that the fractional filling of a complete atomic layer of Fe can be approximated by the ratio of the measured island thickness (t_{Fe}) to the thickness of 1 ML of Fe (t_{ML}). Thus, the quick decay of the spin signal observed at small Fe thickness can be understood in terms of interfacial spin relaxation and quantified by a single parameter $\Gamma_{int}^{Fe/Gr}$, defined as the additional local spin relaxation rate in graphene

underneath at least 1 ML of Fe. This rate is determined by rescaling the additional local spin relaxation rate in the submonolayer regime to account for incomplete coverage

$$\Gamma_{int}^{Fe/Gr} = \frac{1}{\tau_{other}} / \left[\min\left(\frac{t_{Fe}}{t_{ML}}, 1\right)\right]. \qquad (3)$$

As shown in Figure 3.6, the result of this rescaling is that that the additional local spin relaxation rate in graphene underneath at least 1 ML of Fe is relatively insensitive to Fe thickness, with the result from multiple experiments that $\Gamma_{int}^{Fe/Gr} \approx 10^3$ ns^{-1}.

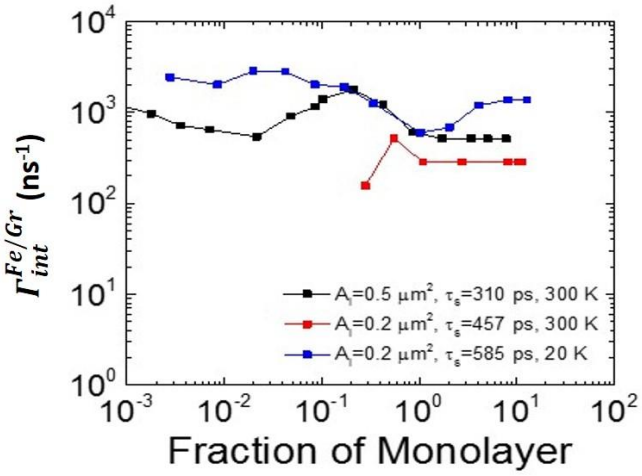

Figure 3.6 Relaxation rate rescaled with island coverage

From these results, a simple physical picture emerges. The interfacial spin relaxation rate of the Fe/graphene junction ($\Gamma_{int}^{Fe/Gr}$) originates from a magnetic interation (options i and/or ii). The Fe/Cu junction also has an interfacial spin relaxation ($\Gamma_{int}^{Fe/Cu}$) which has a lower rate than for the Fe/graphene junction. The slow decay in the Fe/Cu/graphene sample is due to bulk-like spin absorption in the Fe overlayer, and the decay length is given by the spin diffusion length in the Fe. Spin relaxation induced by SOC by sp^3 bonding (option iii) or by proximity-induced SOC (option iv) is ruled out as

the origin of the rapid decay because it cannot explain the rapid decay in the Fe/Cu/graphene sample; adding the Fe does not change the Cu/graphene interface. Therefore, the interfacial spin relaxation has a magnetic origin and could be due to spin momentum transfer or magnetic exchange fields that interact with the spin current. Further studies are required to disentangle these two effects.

3.5 Conclusion:

In conclusion, we report the discovery of an interfacial spin relaxation at the FM/graphene interface probed by pure spin current. Using a Cu spacer between the FM and graphene, we show that the interfacial spin relaxation originates from the interactions of spin-polarized conduction electrons with interfacial magnetic moments. This interfacial spin relaxation could be either due to a transfer of spin angular momentum from the electron spins in graphene to the interfacial magnetic moments (i.e. interfacial spin transfer torque) or due to depolarization of electron spins in graphene by a fluctuating exchange field. Using a 2D finite element modeling, we extracted the relaxation rate under the island associated to the interfacial relaxation.

References

1. W. Han, R. K. Kawakami, M. Gmitra, J. Fabian, Nature Nanotechnology. 9, 794-807 (2014)

2. M. Drögler et al, Nano Letters 16 (6), pp 3533-3539 (2016).

3. J. Ingla-Aynès, M. H. D. Guimares, R. J. Maijernik, P. J. Zomer, and B. J. vanWees, Phys. Rev. B **92**, 201410(R) (2015).

4. W. Amamou, Z. Lin, J. van Baren, S. Turkyilmaz, J. Shi, and R. K. Kawakami, APL Mater. 4, 032503 (2016).

5. H. Idzuchi, Y. Fukuma, S. Takahashi, S. Maekawa, and Y. Otani, Physical Review B **89**, 081308 (2014).

6. W. Han, K. Pi, K. M. McCreary, Y. Li, J. J. I. Wong, A. G. Swartz, and R. K. Kawakami, Phys. Rev. Lett. **105**, 167202 (2010).

7. F. Volmer, M. Drögeler, E. Maynicke, N. von den Driesch, M. L. Boschen, G. Güntherodt, C. Stampfer, and B. Beschoten, Phys. Rev. B **90**, 165403 (2014).

8. N. Tombros, C. Jozsa, M. Popinciuc, H. T. Jonkman, and B. J. van Wees, Nature 448,571 (2007).

9. B. Behin-Aein[1], D. Datta[1], S. Salahuddin and Supriyo Datta, Nature Nanotechnology 5, 266-270 (2010).
10. C. Lin, A. V. Penumatcha, Y. Gao, V. Q. Diep, J. Appenzeller, and Z. Chen, Nanoletters 13, 5177-5181 (2013).

11. C. Lin, Y. Gao, A. V. Penumatcha, V. Q. Diep, J. Appenzeller, and Z. Chen, ACS Nano 8, 3807-3812 (2014).

12. S. Singh, J. Katoch, T. Zhu, K. Meng, T. Liu, J. T. Brangham, F. Y. Yang, M. Flatte and R. K. Kawakami, arXiv: 1610. 08017 (2016).

13. M. Johnson and R. H. Silsbee, Phys. Rev. Lett. **55**, 1790 (1985).

14. E. Sosenko, H. Wei, and V. Aji, Physical Review B **89**, 245436 (2014).

15. K. Pi, Wei Han, K. M. McCreary, A. G. Swartz, Yan Li, and R. K. Kawakami, Physical Review Letters 104, 187201 (2010).

16. K. M. McCreary, K. Pi, and R. K. Kawakami, Applied Physics Letters. 98, 192101 (2011).

17. X. Liu, C. Z. Wang, M. Hupalo, W. Lu, P. A. Thiel, K. M. Ho and M. C. Tringides, Physical Review B 84, 235446 (2011).

18. M. Cattelan. W. Peng, E. Cavaliere, L. Artiglia,A. Barinov, L. T. Roling, M. Favaro, I. Pí, S. Nappini, E. Magnano, F. Bondino, L. Gavioli, S. Agnoli, M. Mavrikakis and G. Granozzi, Nanoscale, 7, 2450-2460 (2015)

19. T. Valet and A. Fert, Physical Review B 48,7099 (1993).

20. J. Bass, and W. P. P. Pratt Jr, J. Phys: Condens Matter 19, 183201 (2007)

21. H. Khylap, From Semi Classical Semiconductor to Novel Spintronics Devices, (Bentham eBooks, 2013).

22. Yu. S. Dedkov and M. Fonin, New Journal of Physics 12, 125004 (2010).

23. P. Lazi, G. M. Sipahi, R. K. Kawakami and I. Zutic, Physical Review B 90, 085429 (2014).

24. A. Dahal, M. Batzill, Nanoscale 6, 2548 (2014).

25. T. Abtew, B. Shih, S. Banerjee and P. Zhang, Nanoscale 5, 1902 (2013).

26. A. M. Shikin, A. G. Rybkin, D. Marchenko, A. A. Rybkina, M. R. Scholz, O. Rader and A. Varykhalov, New Journal of Physics 15, 013016 (2013).

Chapter 4: Contact induced spin relaxation in Graphene spin valves with Al_2O_3 and MgO tunnel barriers

Abstract:

We investigate spin relaxation in graphene by systematically comparing the roles of spin absorption, other contact-induced effects (e.g., fringe fields), and bulk spin relaxation for graphene spin valves with MgO barriers, Al_2O_3 barriers, and transparent contacts. We obtain effective spin lifetimes by fitting the Hanle spin precession data with two models that include or exclude the effect of spin absorption. Results indicate that additional contact-induced spin relaxation other than spin absorption dominates the contact effect. For tunneling contacts, we find reasonable agreement between the two models with median discrepancy of ~20% for MgO and ~10% for Al_2O_3.

4.1 Introduction:

Spin relaxation is one of the most important issues in graphene spintronics. Theoretically, the spin lifetime of graphene is predicted to be on the order of microseconds due to weak spin-orbit coupling [1–6]. Experimentally, however, the measured spin lifetimes typically vary from about a hundred picoseconds to a few nanoseconds [7–15]. This discrepancy of three orders of magnitude represents one of the mysteries of the field. Understanding the origin of this discrepancy between theory and experiment will help close the gap and could lead to graphene materials and devices with exceptionally long spin lifetimes and spin diffusion lengths at room temperature. Central to the investigation of spin relaxation is the role of contacts in graphene spin valves. Experimental studies are based on spin precession measurements in the nonlocal geometry16 and modeling to extract the spin lifetime. In early studies, it was shown that high quality tunnel barriers between the ferromagnetic electrodes and graphene are needed to achieve spin lifetimes in excess of 200 ps [13] but the nature of the contact-related effects producing this enhancement has remained unclear. One contact-related issue is the conductivity mismatch between the ferromagnetic electrode and the graphene, which causes the spins to flow from the graphene into the ferromagnet ("spin absorption") and results in lower effective spin lifetimes [9,17] Other contact effects could include the nature of the interface between the ferromagnet and the graphene such as spin relaxation due to magnetostatic fringe field at

the contact,18 interfacial spin flip scattering [19–21] contact induced band bending, and spin scattering due to the hybridization of the ferromagnet d-orbital with the graphene's π-orbital [22–26]. Therefore, the extracted spin lifetime will include contributions from the "bulk" spin relaxation in graphene (independent of contacts and including intrinsic and extrinsic spin scattering) and contact-induced spin relaxation. Because accurate determination of the bulk spin lifetime is important, it is worthwhile to clarify the role of contacts through systematic experimental studies.

In this Letter, we investigate spin relaxation in graphene by systematically comparing the roles of spin absorption, other contact-induced effects, and bulk spin relaxation. We analyze a set of graphene spin valves with Ti-seeded MgO barriers and utilize two different models of nonlocal Hanle precession to understand the role of spin absorption. Primarily, we find that some form of contact-induced spin relaxation other than spin absorption dominates the contact effect. To understand whether this is specific to MgO barriers or is more general, we develop graphene spin valves with smooth Al_2O_3 barriers and observe similar behavior. Beyond this, we are able to draw several conclusions, which can be described more clearly after discussing the models employed in the analysis.

To analyze Hanle spin precession data, we employ two different models. The first model is a "traditional model" (TM) which does not explicitly take spin absorption into account [27]. The spin accumulation in an applied magnetic field is described by the steady state Bloch equation:

$$D\nabla^2\mu_s - \frac{\mu_s}{\tau_s} + \omega_L \times \mu_s = 0 \qquad (1)$$

where D is the diffusion constant, τ_s is the bulk spin lifetime, μ_s is the spin accumulation, $\omega_L = g\mu_B B/\hbar$ is the Larmor frequency, g is the gyromagnetic factor, μ_B is the Bohr magneton, and B is the magnetic field. For the nonlocal Hanle geometry, this results in a nonlocal signal given by:

$$R_{NL} \propto \pm \int_0^\infty \frac{1}{\sqrt{4\pi D t}} \exp\left[-\frac{L^2}{4Dt}\right] \cos(\omega_L t) \exp(-t/\tau_s)\, dt \quad (2)$$

where L is the separation between spin injector and spin detector. Because the model does not explicitly take contact-induced spin relaxation into account, the fitted spin lifetime, which we denote as τ_{TM}, should be considered as an effective spin lifetime given by:

$$\frac{1}{\tau_{TM}} = \Gamma_{bulk} + \Gamma_{abs} + \Gamma_{other} = \frac{1}{\tau_s} + \frac{1}{\tau_{abs}} + \frac{1}{\tau_{other}} \quad (3)$$

Where Γ_{bulk} is the bulk spin relaxation rate in graphene, Γ_{abs} is the contact-induced spin relaxation rate due to spin absorption, and Γ_{other} is the contact-induced spin relaxation rate from other effects (e.g. fringe fields, etc.).

The second model explicitly takes into account the contact-induced spin relaxation by spin absorption, and we denote such models as "spin absorption models" (SAM) [9, 17, 28, 29] This was first introduced by van Wees and coworkers [9,17], but an analytical solution for the Hanle curve was not found initially. Subsequently, Aji and coworkers [29] derived an analytical solution for the nonlocal Hanle signal, which is given by:

$$R_{NL}^{\pm} = p_1 p_2 R_N f$$

$$f = Re\left(2\left[\sqrt{1+i\omega_L\tau_{SAM}} + \frac{\lambda}{2}\left(\frac{1}{r_1}+\frac{1}{r_2}\right)\right] e^{\left(\frac{L}{\lambda}\right)\sqrt{1+i\omega_L\tau_{SAM}}} + \frac{\lambda^2}{r_1 r_2}\frac{\sinh\left[\left(\frac{L}{\lambda}\right)\sqrt{1+i\omega_L\tau_{SAM}}\right]}{\sqrt{1+i\omega_L\tau_{SAM}}}\right)^{-1} \quad (4)$$

Where τ_{SAM} is the fitted spin lifetime, λ is the spin diffusion length in graphene, and $r_i = \frac{R_F+R_C^i}{R_{SQ}}W$ with $i = 1$ for the injector and $i = 2$ for the detector, R_C is the contact resistance, R_{SQ} is the sheet resistance of graphene, W is the width of the graphene, $R_N = R_{SQ}\,\lambda/W$ is the spin resistance of graphene, $R_F = \rho_{fm}\,\lambda_{fm}/A$ is the spin resistance of the ferromagnet, ρ_{fm} is the resistivity of the ferromagnet, λ_{fm} is the spin diffusion length in the ferromagnet, and A is the junction area. Considering equation (2), the main difference from τ_{TM} is that the effect of spin absorption is explicitly calculated within the model, so the effective spin lifetime consists only of the remaining spin relaxation mechanisms, namely

$$\frac{1}{\tau_{SAM}} = \Gamma_{bulk} + \Gamma_{other} = \frac{1}{\tau_s} + \frac{1}{\tau_{other}} \quad (5)$$

Thus, it is clear that the spin absorption model is more accurate than the traditional model in determining the bulk spin lifetime.

The large difference in spin resistances between graphene (R_N) and the ferromagnet (R_F) will result in rapid flow of spins from graphene to the ferromagnet. The amount of spin absorption can be controlled by introducing a tunnel barrier between the graphene and the ferromagnet. This is especially important for Co electrodes on graphene channel where the spin resistance of the ferromagnet is much less than the spin resistance of graphene, which would produce large spin absorption in the absence of a barrier.

Beyond the van Wees and Aji model, the Otani group introduced an anisotropic term represented by the mixing conductance $G_{\uparrow\downarrow}$ that accounts for different spin absorption

rate for longitudinal and transverse spins. While this anisotropy has been demonstrated in metallic spin valve, in the case of graphene the anisotropic spin absorption is almost the same as the isotropic one (within 4% difference) due to the higher junction resistance relative to the ferromagnet [28]. Therefore, in the case of graphene spin valves this model is equivalent to the van Wees and Aji model (equation 4).

Recently in Idzuchi *et al* [30], the Otani group re-analyzed our Hanle data on graphene spin valves with Ti-seeded MgO barriers using the spin absorption model. It was noticed that τ_{SAM} for four devices approached similar values near 500 ps, independent of the contact resistance-area product ($R_C A$). The interpretation was that the contact-induced effect is primarily due to spin absorption because the τ_{SAM} converges to a constant value representing the bulk spin lifetime (i.e. $\tau_{other} \sim 0$). Taken at face value, this is a good method to analyze spin relaxation: if τ_{SAM} converges to a constant value independent of $R_C A$, this likely represents the bulk spin lifetime; if τ_{SAM} varies and is correlated to $R_C A$, then the contact-induced spin relaxation from other effects (τ_{other}) can be substantial; if τ_{SAM} varies and is uncorrelated to $R_C A$, other dependencies should be explored, such as the dependence on electrode spacing or other relevant parameters.

In our study, we follow this approach to analyze a larger set of graphene spin valves with Ti-seeded MgO barriers and Al_2O_3 barriers. We also compare the effective spin lifetimes from the two models, τ_{TM} and τ_{SAM}, to elucidate the roles of spin absorption, other contact effects, and bulk spin relaxation in determining the overall spin lifetime. Through our studies, we draw the following conclusions: (1) the contact-induced spin relaxation rate from other contact effects, τ_{other}, is substantial, (2) spin absorption is not the

dominant source of spin relaxation, except in some cases with transparent contacts, (3) for tunneling contacts, the ratio τ_{TM}/τ_{SAM} is typically found in the 60% - 90% range with median value of ~80% for MgO barriers and 70% - 100% range with median value of ~90% for Al_2O_3 barriers, (4) simulations provide a guideline for estimating the relative importance of spin absorption in determining the spin lifetime.

4.2 Experimental methods:

To fabricate devices, we exfoliate single layer graphene flakes onto SiO_2 (300 nm)/Si wafers, where the degenerately doped Si is used as a backgate. The graphene thickness is determined by optical contrast and calibrated using Raman spectroscopy. For the Ti-seeded MgO tunnel barrier devices, we utilize a single e-beam lithography pattern using bilayer PMMA/MMA resist combined with angle evaporations to define the MgO barrier and the 80 nm thick Co electrodes. The angle evaporation results in a small contact width of ~50 nm between the Co and graphene. Details of the device fabrication are provided elsewhere [12]. For the Al_2O_3 tunnel barrier devices, we grow aluminum over the entire sample by sputter deposition at a rate of 0.4 Å/s using Ar gas at a pressure of 5 mT and oxidize for 30 min at atmospheric pressure of O_2, following Dlubak *et al.* [31, 32] The resulting Al_2O_3 layer can therefore act as both a tunnel barrier and a protective layer for the graphene. An AFM image of 1 nm of aluminum oxide on top of single layer graphene is shown in Figure 4.1(a). The rms roughness is 0.117 nm and the surface is smooth with no observable pinholes at 1 nm thickness. This suggests that sputtered aluminum with post oxidation could be an excellent tunnel barrier candidate. To check for possible sputtering-

induced defect formation, we perform Raman spectroscopy before and after Al_2O_3 deposition, shown in Figure 4.1(b). We observe the emergence of a relatively small D peak (30% of G peak magnitude), which suggests the presence of fewer sputtering-induced defects in the graphene layer compared to previous studies [31, 32]. Finally, we define Co electrodes with various widths using bilayer PMMA/MMA resist and deposit 80 nm of Co in a molecular beam epitaxy (MBE) chamber with base pressure of 5×10^{-10} Torr. Because this process does not utilize the angle evaporation, the contact width is equal to the electrode width, which typically varies from 150 nm to 500 nm.

4.3 Results:

To characterize the electrical properties of the Al_2O_3 tunnel barrier, we measure gate dependence and three terminal differential contact resistance dV/dI. First, we perform a 4-probe resistance measurement as a function of gate voltage to determine the charge neutrality point and field effect mobility of the graphene. The measurement is performed using lock-in detection with an AC current of 1 μA at 211 Hz injected between contacts E1 and E4 (inset figure 4.1(c)) and voltage detection between E2 and E3. Figure 4.1(c) shows a typical gate dependence curve of graphene with a 1 nm Al_2O_3 overlayer.

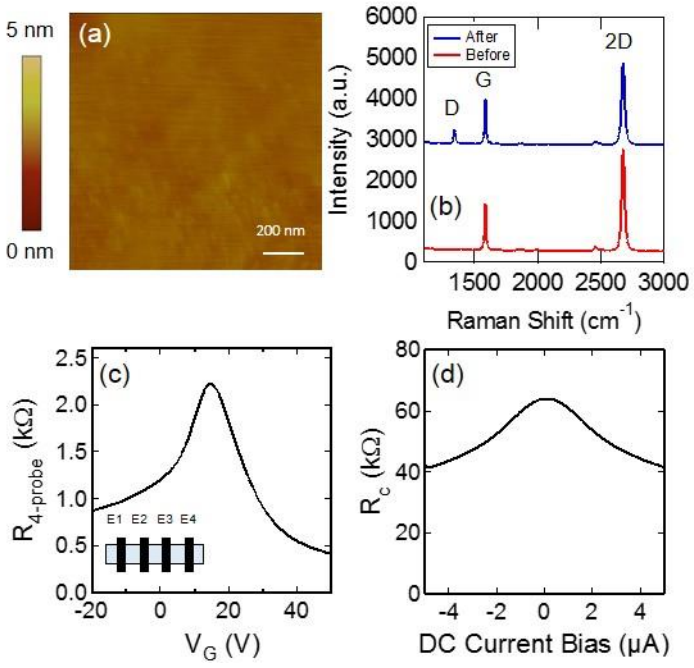

Figure 4.1. (a) AFM image of 1 nm Al_2O_3 on graphene (b) Raman spectroscopy of graphene with 1 nm Al_2O_3 overlayer (c) 4-probes gate dependence of graphene spin valve (d) Three terminal differential contact resistance dVdI of Gr/ Al_2O_3 (e) Contact resistance temperature dependence

We observe a relatively small doping effect with charge neutrality point at V_G = 15 V. The resulting carrier density at zero gate voltage is 1.08×10^{12} cm^{-2} (holes). The electron mobility is extracted from the slope of the gate dependent conductivity σ measured in a range 5-10 V away from the Dirac point, and is μ_e= 3005 cm^2/Vs for electrons and μ_h= 948 cm^2/Vs for holes. The values of the mobility are comparable to pristine graphene spin valves [8, 12].

We characterize the tunneling property of the 1 nm Al_2O_3 contact by a three terminal dV/dI measurement where we inject a current between contacts E2 and E1 and measure voltage between contacts E2 and E3. Figure 4.1(d) shows typical dV/dI curves

that exhibit a cusp-like behavior as a function of DC bias, and junctions with such a shape are found to exhibit little temperature dependence, consistent with tunneling behavior. It is worth noting that as we decrease the barrier thickness, the dV/dI curve transitions from a peak-like shape to a flat shape. Typically, devices with R_cA lower than 7 $k\Omega\mu m^2$ exhibit a flat shape dV/dI and an increase of the contact resistance with temperature, suggesting metallic pinhole interface in accordance with a recent TEM study of Al_2O_3 growth on graphene [33].

Spin transport measurements are carried out using a lock-in detection with an AC injection current of I_{INJ} = 1 μA rms at 11 Hz between contacts E1 and E2 (injector) (see Fig 4.2 (a) inset). Electron spin density injected at E2 diffuses toward electrode E3 (detector), which generates a non-local voltage V_{NL} measured between E3 and E4. Spin transport is identified by ramping an in-plane magnetic field to achieve parallel and antiparallel alignments of the injector and detector magnetizations. For Hanle spin precession measurements, an out of plane magnetic field is ramped while measuring V_{NL} with electrodes in the parallel and antiparallel magnetization states. For fitting the Hanle data using equation (2) or (4), both the diffusion constant and spin lifetime are fitting parameters. The spin measurements are performed near zero gate voltage (20 out of the 22 samples are measured at V_G = 0 V, while the others have $|V_G| \leq 3$ V).

We investigate spin transport in graphene spin valves with MgO and Al_2O_3 barriers. Figures 4.2 (a) and (d) show the room temperature nonlocal resistance ($R_{NL} = V_{NL}/I_{INJ}$) as an in-plane magnetic field is swept up and down for MgO and Al_2O_3 barriers, respectively.

The non-local resistance exhibits a sharp switching as the injector and detector transition from the parallel to antiparallel states, indicating spin transport in graphene.

The difference in the switching fields for the MgO and Al_2O_3 barriers (Fig 4.2 (a) and 2 (d)) is due to the different shapes of the Co electrodes. For the MgO device, the size of the nonlocal magnetoresistance (ΔR_{NL}) is ~25 Ω with the average R_CA of 1.13 kΩ μm^2. For the Al_2O_3 device, we measure ΔR_{NL} of 20 Ω with average R_CA of 58 kΩ μm^2.

In order to extract the spin lifetime and spin diffusion length, we perform Hanle spin precession measurements by applying an out-of-plane magnetic field. This causes the spins to precess in-plane as they diffuse between contacts E2 and E3, resulting in the so-called Hanle curves shown in Figure 4.2 (b) and (e) for MgO and Al_2O_3, respectively.

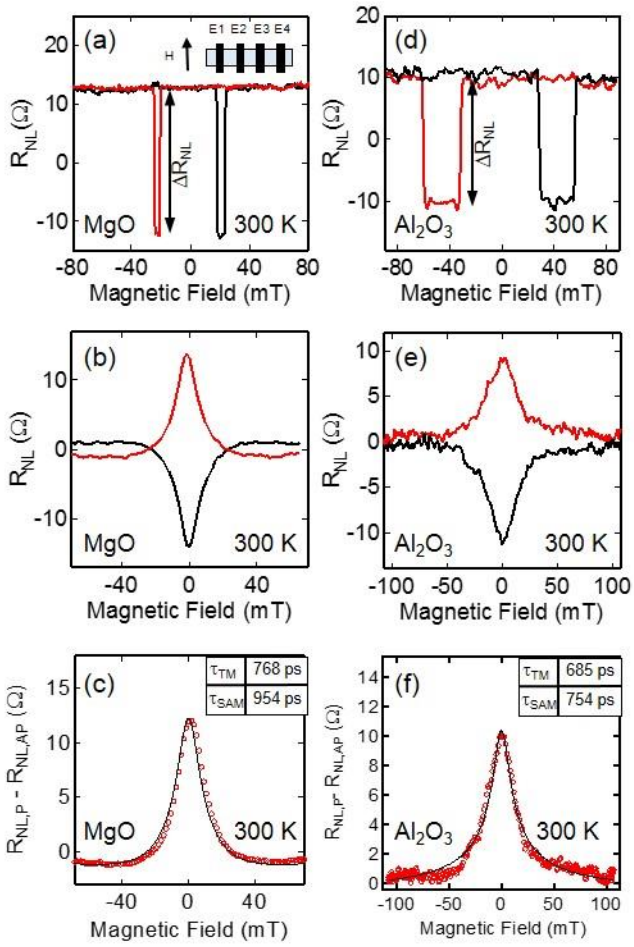

Figure 4.2. (a) Non-local MR of TiO_2/MgO graphene spin valve (b) Hanle measurement of TiO_2/MgO graphene spin valve (c) Hanle fitting using the traditional and spin absorption model (d) Non-local MR of Al_2O_3 graphene spin valve (b) Hanle measurement of Al_2O_3 graphene spin valve (c) Hanle fitting using the traditional and spin absorption model

The red (black) curves correspond to the spin precession with electrodes in the parallel (antiparallel) configuration. The spin lifetime is first extracted using the traditional model by fitting the difference of the parallel and antiparallel Hanle curves (shown in Figure 4.2 (c) and 4.2 (f)) using equation 2, yielding τ_{TM} = 768 ps for MgO and τ_{TM} = 685 ps for

Al_2O_3. Fitting the same data with the spin absorption model using equation 4 yields spin lifetimes of τ_{SAM} = 954 ps for MgO and τ_{SAM} = 754 ps for Al_2O_3. Because τ_{TM} includes the effects of both spin relaxation and spin absorption (equation 3), this results in lower effective spin lifetime compared to τ_{SAM} (equation 5).

In a previous study, Idzuchi *et al* reported an intrinsic spin lifetime in graphene independent of the type of the contact (transparent, pinhole or tunneling) when spin absorption is taken in account, suggesting the absence of the additional contact-induced spin dephasing term [30]. We investigate this further by performing more extensive studies of spin lifetime as a function of contact resistance area product for MgO and Al_2O_3 tunnel barriers.

In Figure 4. 3 (a) and (d), we present the extracted spin lifetime from experimental Hanle curves using the standard Bloch equation that does not separate out the effect of spin absorption (equation (2)). For the fit, τ_{TM}, D, and the overall amplitude are fitting parameters, while g = 2 and L and W are determined from measurements. The spin lifetime extracted from this fitting is an effective lifetime τ_{TM} that includes the bulk spin lifetime as well as the spin absorption and other contact induced effects following equation (3). Thus the fitted lifetime could be much lower than the bulk spin lifetime τ_s. The effective spin lifetime from this model shows a strong dependence on R_CA (the average resistance-area product of the injector and detector contacts). Specifically, low R_CA corresponds to short τ_{TM} while large R_CA corresponds to long τ_{TM}. This indicates the importance of contact induced spin relaxation, and the trend is consistent with the expected behavior of τ_{TM} with R_CA due to spin absorption effect. In order to test this quantitatively, we employ models

that separate out the effect explicitly such as the models proposed by van Wees, Aji and Otani [9, 28, 29].

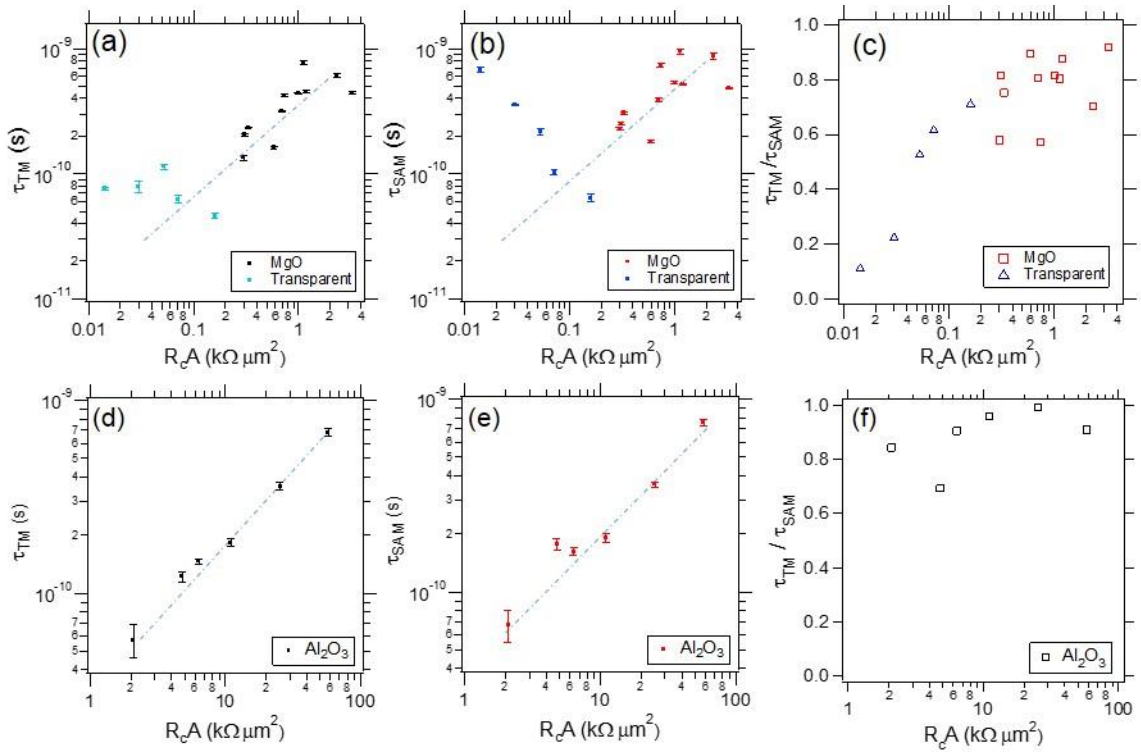

Figure 4.3. (a) τ_{TAM} dependence on R_cA for TiO_2/MgO spin valve (b) τ_{SAM} dependence on R_cA for $Al_2O_3TiO_2$/MgO spin valve (c) Ratio τ_{TAM}/τ_{SAM} for TiO_2/MgO (d) τ_{TAM} dependence on R_cA for spin valve for Al_2O_3 (b) τ_{SAM} dependence on R_cA for Al_2O_3 spin valve (c) Ratio τ_{TAM}/τ_{SAM} for Al_2O_3

In Figure 4. 3 (b) and (e), we fit the Hanle curves using the Aji's analytical solution of the van Wees model including the spin absorption effect (equation 4). For the fit, τ_{SAM}, D, and the overall amplitude are fitting parameters, while $g = 2$ and L and W are determined from measurements. We also use separate values for the measured contact resistances R_C^1 and R_C^2 of the spin injector and detector although we plot the data based on the average R_CA product. We observe that the extracted value of τ_{SAM} is larger than τ_{TM} from the

traditional fit for both the Al_2O_3 barrier and the MgO. Most strikingly, there is still a strong dependence on the R_CA product of the contacts, contrary to the trend reported in Idzuchi *et al* [30]. Because the value of τ_{SAM} does not converge to a universal value independent of R_CA, according to equation (5) this implies that other contact induced effects (Γ_{other}) are important in agreement with Volmer et al. [22, 23].

In Figure 4. 3(b) we plot the transparent contact data along with the MgO tunnel barrier data for comparison. It is worth noting, that the extracted spin lifetime τ_{SAM} is very sensitive to the value of the contact resistance of the injector and detector. Therefore, any uncertainty in the contact resistance value will lead to a significant variation in τ_{SAM}. This sensitivity is more prominent in case of transparent devices where the contact resistance measurement includes the Co/graphene junction resistance and the Co lead resistance. Due to the low contact resistance value of the interface, this leads to high uncertainty of the interface resistance and the extracted spin lifetime. In the case of tunnel barrier, the junction resistance is significantly higher than the lead resistance, resulting in a more accurate determination of the spin lifetime. For transparent devices without a tunnel barrier, we observe an increase of τ_{SAM} by almost two orders of magnitude up to 679 ps as compared to τ_{TM} = 76 ps for the lowest R_CA data point, consistent with the result in Idzuchi *et al*. [30] However, as R_CA increases, we observe a decrease in τ_{SAM} down to 64 ps. The higher values of R_CA for some transparent devices are likely due to resist residue at the interface of Co/graphene which leads to higher contact resistances. This results in a lower spin lifetime as the R_CA increases, mainly due to less correction from the spin absorption effect.

In Figure 4. 3 (c), we estimate the role of spin absorption compared to other spin relaxation mechanisms by plotting the τ_{TM}/τ_{SAM} ratio as a function of R_CA product for the MgO samples. The discrepancy between τ_{TM} and τ_{SAM} is the greatest for transparent contacts, where the τ_{TM}/τ_{SAM} ratio is as low as ~10%. As we introduce the MgO barrier, the τ_{TM}/τ_{SAM} ratio increases to the ~60 – 90% range (median value of ~80%). To further investigate this effect, we perform the same analysis for the Al_2O_3 samples, with the τ_{TM}/τ_{SAM} ratio shown in Figure 4. 3(f). Here, the agreement increases into the ~70% - 100% range (median value of ~90%). The relatively high values of τ_{TM}/τ_{SAM} for tunneling contacts indicates that there is reasonable agreement between the spin absorption model and traditional model in many cases. The relative importance of spin absorption compared to the overall spin relaxation is given by $\Gamma_{abs}/(\Gamma_{abs} + \Gamma_{other} + \Gamma_{bulk}) = 1 - \tau_{TM}/\tau_{SAM}$, which has a median value of ~20% for MgO and ~10% for Al_2O_3. Therefore, we conclude that spin absorption is not the dominant spin relaxation mechanism, in agreement with Maassen *et al.* [17] and Volmer et al [22, 23].

Finally, we perform simulations to provide a guideline for reasonable fitting procedures, considering the influence of the contact resistance and channel length on the Hanle curves. To compare the models, we follow a procedure where we generate Hanle curves using the spin absorption model (equation (4)) and fit these curves with the standard Bloch equation (2) [9]. In Figure 4.4, we show a 2D image plot of the ratio τ_{TM}/τ_{SAM} as function of R_c/R_s for different values of L/λ where R_c is the contact resistance, R_s is the spin resistance of the graphene, L is the channel length and λ is the spin diffusion length. The simulations are performed using D=0.01 m^2/s and τ_{SAM} = 1 ns. While τ_{TM}/τ_{SAM}

converges to 1 (blue region) at high R_c/R_s, we observe a striking decrease in τ_{TM}/τ_{SAM} for very low R_c/R_s (red region). The difference between τ_{TM} and τ_{SAM} is magnified as we decrease the channel length L between the injector and detector. First, we notice that Rc/Rs and L/λ have a strong influence on the obtained ratio and therefore dictate how well the standard and spin absorption model agree. This can be understood as follows: as we decrease the Rc/Rs ratio, more spins are absorbed into the ferromagnet due to the conductance mismatch. This results in an apparent low spin lifetime when the effect is not taken in account, which will increase the difference between τ_{TM} and τ_{SAM}. When L/λ becomes large, the τ_{TM}/τ_{SAM} converges to 1, largely independent of Rc/Rs, indicating agreement between the fitting procedures (see case L/λ=100). As we increase the channel length, most of the spin relaxation and diffusion occurs in the graphene channel without interference from the contact.

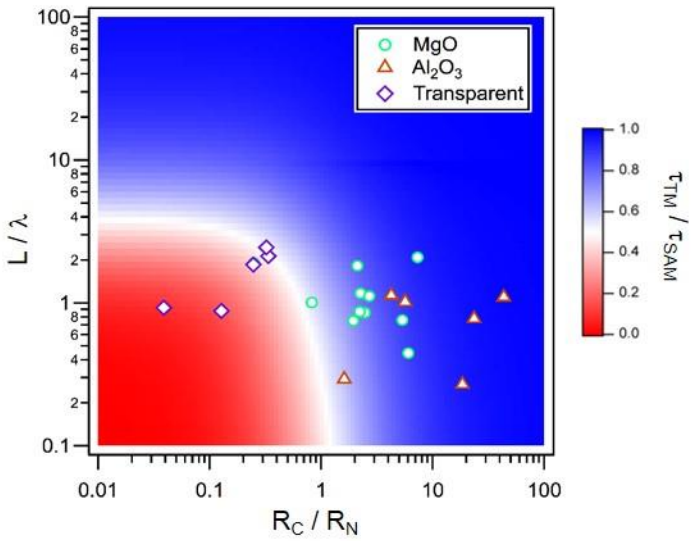

Figure 4.4. Simulations of Hanle curves using $\tau_{SAM} = 1\ ns$ and D = 0.01 m^2/s and fitting with the traditional model.

Therefore, performing Hanle measurements using long channel lengths and high contact resistance is recommended in order to minimize the spin absorption effect.

To compare with experimental data, we plot our experimental parameters as data points in the 2D graph with open circles for MgO, triangles for Al_2O_3 and diamond for transparent. We observe that for the Al_2O_3, most of the devices are located in the blue region consistent with the ratios plotted in Figure 4. 3(f). For MgO tunnel barrier, the devices are spread between the blue and red regions. The effect of spin absorption is more pronounced for the transparent devices as indicated by the points located in the red region.

4.4 Conclusion

We investigate the contact induced spin relaxation in a large set of graphene spin valve devices using two different types of tunnel barrier, MgO and Al_2O_3. We observe a strong dependence of τ_{SAM} with R_cA for both tunnel barriers. Our analysis suggests that spin relaxation rate from other contact induced effect Γ_{other} is significant. The spin absorption has a minor effect on the overall spin relaxation except in some cases with transparent contacts. Instead, other sources of contact-induced spin relaxation (e.g. fringe fields, etc.) are more important. Thus, further investigation of the tunnel barrier microstructure using TEM is needed to understand the role of the contact on the spin relaxation mechanism. For tunneling contacts, the τ_{TM}/τ_{SAM} ratio has a median value of ~80% for MgO barriers and ~90% for Al_2O_3 barriers, indicating that the two models have reasonable agreement in many cases. Nevertheless, the spin absorption models are more accurate and should be applied whenever accurate measurement of the contact resistance

can be obtained. Finally, we provide a guideline for estimating the relative importance of spin absorption in determining spin lifetimes through simulations.

References

1. D. Huertas-Hernando, F. Guinea, and A. Brataas, Phys. Rev. B **74**, 155426 (2006).

2. H. Min, J. E. Hill, N. A. Sinitsyn, B. R. Sahu, L. Kleinman, and A. H. MacDonald, Phys. Rev. B **74**, 165310 (2006).

3. Y. Yao, F. Ye, Y.-L. Qi, S.-C. Zhang, and Z. Fang, Phys. Rev. B **75**, 041401(R) (2007).

4. B. Trauzettel, D. V. Bulaev, D. Loss, and G. Burkard, Nature Physics **3**, 192 (2007).

5. D. Huertas-Hernando, F. Guinea, and A. Brataas, Phys. Rev. Lett. **103**, 146801 (2009).

6. W. Han, R. K. Kawakami, M. Gmitra, and J. Fabian, Nature Nano. **9**, 794 (2014).

7. N. Tombros, C. Jozsa, M. Popinciuc, H. T. Jonkman, and B. J. Van Wees, Nature **448**, 571 (2007).

8. C. Jozsa, T. Maassen, M. Popinciuc, P. J. Zomer, A. Veligura, H. T. Jonkman, and B. J. van Wees, Phys. Rev. B **80**, 241403(R) (2009).

9. M. Popinciuc, C. Jozsa, P. J. Zomer, N. Tombros, A. Veligura, H. T. Jonkman, and B. J. van Wees, Phys. Rev. B **80**, 214427 (2009).

10. M. Shiraishi, M. Ohishi, R. Nouchi, T. Nozaki, T. Shinjo, and Y. Suzuki, Adv. Func. Mater. **19**, 1 (2009).

11. K. Pi, W. Han, K. M. McCreary, A. G. Swartz, Y. Li, and R. K. Kawakami, Phys. Rev. Lett. **104**, 187201 (2010).

12. W. Han, K. Pi, K. M. McCreary, Y. Li, J. J. I. Wong, A. G. Swartz, and R. K. Kawakami, Phys. Rev. Lett. **105**, 167202 (2010).

13. W. Han and R. K. Kawakami, Phys. Rev. Lett. **107**, 047207 (2011).

14. W. Han, K. Pi, W. Bao, K. M. McCreary, Y. Li, W. H. Wang, C. N. Lau, and R. K. Kawakami, Appl. Phys. Lett. **94**, 222109 (2009).

15. T.-Y. Yang, J. Balakrishnan, F. Volmer, A. Avsar, M. Jaiswal, J. Samm, S. R. Ali, A. Pachoud, M. Zeng, M. Popinciuc, G. Guntherodt, B. Beschoten, and B. Ozyilmaz, Phys. Rev. Lett. **107**, 047206 (2011).
16. M. Johnson and R. H. Silsbee, Phys. Rev. Lett. **55**, 1790 (1985).

17. T. Maassen, I. J. Vera-Marun, M. H. D. Guimarães, and B. J. van Wees, Physical Review B **86**, 235408 (2012).

18. S. P. Dash, S. Sharma, J. C. Le Breton, J. Peiro, H. Jaffrès, J. M. George, A. Lemaître, and R. Jansen, Physical Review B **84**, 054410 (2011).

19. S. Garzon, I. Žutić, and R. A. Webb, Physical Review Letters **94**, 176601 (2005).

20. J.-H. Park and H.-J. Lee, Physical Review B **89**, 165417 (2014).

21. B. Li, L. Chen, and X. Pan, Applied Physics Letters **98**, 133111 (2011).

22. F. Volmer, M. Drögeler, E. Maynicke, N. von den Driesch, M. L. Boschen, G. Güntherodt, and B. Beschoten, Physical Review B **88**, 161405 (2013).

23. F. Volmer, M. Drögeler, E. Maynicke, N. von den Driesch, M. L. Boschen, G. Güntherodt, C. Stampfer, and B. Beschoten, Physical Review B **90**, 165403 (2014).

24. A. Varykhalov, D. Marchenko, J. Sánchez-Barriga, M. R. Scholz, B. Verberck, B. Trauzettel, T. O. Wehling, C. Carbone, and O. Rader, Physical Review X **2**, 041017 (2012).

25. A. Varykhalov and O. Rader, Physical Review B **80**, 035437 (2009).

26. T. Abtew, B.-C. Shih, S. Banerjee, and P. Zhang, Nanoscale **5**, 1902 (2013).

27. F. J. Jedema, H. B. Heersche, A. T. Filip, J. J. A. Baselmans, and B. J. van Wees, Nature **416**, 713 (2002).

28. H. Idzuchi, Y. Fukuma, S. Takahashi, S. Maekawa, and Y. Otani, Physical Review B **89**, 081308 (2014).

29. E. Sosenko, H. Wei, and V. Aji, Physical Review B **89**, 245436 (2014).

30. H. Idzuchi, A. Fert, and Y. Otani, Physical Review B **91**, 241407 (2015).

31. B. Dlubak, P. Seneor, A. Anane, C. Barraud, C. Deranlot, D. Deneuve, B. Servet, R. Mattana, F. Petroff, and A. Fert, Appl. Phys. Lett **97**, 092502 (2010).

32. B. Dlubak, M.-B. Martin, C. Deranlot, K. Bouzehouane, S. Fusil, R. Mattana, F. Petroff, A. Anane, P. Seneor, and A. Fert, Appl. Phys. Lett. **101**, 203104 (2012).
33. B. Canto, C. P. Gouvea, B. S. Archanjo, J. E. Schmidt, and D. L. Baptista, Scientific Reports **5**, 14332 (2015).

Chapter 5: Proximity induced ferromagnetism in $CoFe_2O_4$/Pt system

Abstract:

Spin manipulation using a nonmagnetic material without the application of magnetic field is considered as a very promising venue toward the realization of low energy consumption devices for storage and spin logic applications. In particular, Pt has been the nonmagnetic material of choice for generating and detecting pure spin current using the spin Hall effect (SHE) and the inverse spin Hall effect (ISHE) due it's high spin orbit coupling. Furthermore, inducing ferromagnetism in Pt is an important step toward the realization of nonvolatile all spin logic devices using pure spin current. Here, we report the observation of strong magnetic proximity effect of Pt deposited on top of a perpendicular magnetic anisotropy (PMA) inverse spinel material (CFO, $CoFe_2O_4$). The CFO was grown by MBE and its magnetization was characterized by vibrating sample magnetometry (VSM) demonstrating the strong out of plane magnetic anisotropy of this material. The anomalous Hall measurement of a Pt/CFO hall bar exhibits a strong non-linear background around the saturation of the out of plane CFO magnetization. After subtraction of the ordinary Hall effect (OHE), we extract a strong hysteretic anomalous Hall voltage that indicates that Pt acquired the magnetization properties of the CFO and has become ferromagnetic due to the proximity effect.

5.1 Introduction

Spin manipulation inside a nonmagnetic (NM) material using internal effective fields (spin orbit or exchange) is a very promising avenue toward the realization of next generation spintronic devices (spin transistors, magnetic gates, etc.) [1, 2]. In particular, magnetic proximity effect (MPE) at the interface of a NM spin channel and a ferromagnetic insulator (FMI) is of great importance. MPE is an exchange coupling between the magnetic moments of the FMI and the electronic states of the NM, leading to an effective magnetic exchange field (MEF) and induced ferromagnetism in the NM. Recently, spin manipulation by MPE has been realized in experiments that fully modulate spin currents in a graphene on YIG (yttrium iron garnet) [3, 4], and investigation of graphene on EuS observe MEF as high as 14 T [5]. In addition, out of plane MEF at the WSe_2/EuS interface has been realized using an external field of a few Tesla to bring the magnetization out of plane, leading to the control of the valley-dependent spin splitting in the WSe_2 layer [6].

Looking forward, there is a growing interest in developing systems for out of plane MEF in zero external field, which is motivated by efforts to realize proximity-induced quantum anomalous Hall Effect [7] and other topological states, as well as further studies of spin manipulation. Unfortunately, the easy magnetization axis in most known FMIs, such as ferromagnets EuO, EuS, EuSe, GdN, and ferrimagnet YIG, lies inside the thin film plane. Magnetic insulators with perpendicular magnetocrystalline anisotropy (PMA) are scarce. However, very recently a new magnetic insulator TIG (thulium iron garnet) with

PMA has been shown to induce magnetism into an adjacent Pt film through magnetotransport measurements [8, 9]. In addition, a class of cubic FMI based on the spinel ferrites ($CoFe_2O_4$, $NiFe_2O_4$, etc.) has been shown to exhibit a large PMA [10, 11]. Among these, cobalt ferrite ($CoFe_2O_4$, or CFO) is particularly attractive because it is a hard magnet with large coercivity [10], which makes it robust against external magnetic perturbations and will likely suppress fluctuating MEFs that produce spin dephasing. Furthermore, the magnetic properties of CFO can be readily tuned by strain or cation distribution on the A and B sites to produce square hysteresis loops in either out-of-plane or in-plane geometries, and the magnetization can be switched by electric fields [12, 13]. Finally, CFO exhibits spin filtering properties [10] and is readily integrated with typical spintronic materials (MgO, Fe, Cr), enabling the possibility for gate-tunable MPE and other novel device concepts. This has motivated studies to assess whether CFO could be used for MPE.

To test for MPE in NM/FMI systems, Pt is widely used as the NM material due to its closeness to fulfilling the Stoner criteria and thus allowing it to become ferromagnetically ordered at the interface with the FMI. Initial studies of Pt/CFO grown by pulsed laser deposition (PLD) utilized magnetotransport measurements observed no MPE in the Pt layer [14]. Subsequently, element-specific magnetization measurements by x-ray magnetic circular dichroism (XMCD) also found no evidence for induced ferromagnetism in the Pt layer [15]. These results were later confirmed by Wu et al, who did not detect any MPE in their Pt/CFO by either XMCD or magnetotransport measurements [16], and there has been a growing consensus that CFO cannot be used for MPE. On the other hand, MPE should be extremely sensitive to the interface quality, so

alternative growth methods with improved control of the interfaces could be important for realizing the MPE.

Here, we utilize molecular beam epitaxy (MBE) to synthesize Pt/CFO bilayers and observe the presence of MPE (i.e. induced ferromagnetism) in the Pt layer. This is revealed through low temperature (5 K) transport measurements in the Pt layer, which exhibit anomalous Hall Effect (AHE) and anisotropic magnetoresistance (AMR). Furthermore, the coercive field of the AHE signal differs from the underlying CFO film, indicating a modified magnetic state at the Pt/CFO interface. We also observe the presence of spin Hall magnetoresistance (SMR) and a related contribution to the AHE measurement, known as spin Hall AHE (SH-AHE), which are generated by interfacial scattering of spin currents (as reported previously in Pt/CFO). To separate the effects of MPE and spin Hall in the transport measurements, we perform a systematic study utilizing a Cu interlayer which should eliminate the MPE while preserving the effects from spin Hall currents. A comparison of AHE measurements and angle-dependent magnetoresistance scans (AMR and SMR) for Pt/CFO vs. Pt/Cu/CFO further confirms the presence of MPE in Pt/CFO and also provides evidence for MPE up to room temperature. These results demonstrate that the high quality of materials and interfaces produced by MBE is important for the observation of MPE in Pt/CFO, and establish the cubic spinel ferrites as a promising class of materials for generating proximity-induced exchange fields.

5.2 Experimental Methods

Samples are grown in a MBE chamber with base pressure of ~2×10^{-10} Torr. MgO (001) substrates (10 mm x 10 mm x 0.5 mm, double-sided polished from MTI) are rinsed

in de-ionized water, loaded into the MBE chamber, annealed at 600˚C for 30 minute, and smoothed by subsequent deposition of ~5 nm electron-beam evaporated MgO buffer layer grown at 350˚C at a rate of 1 Å/min. Growth temperatures are measured by a thermocouple placed near the substrate and deposition rates are measured by a quartz crystal monitor. CFO films are deposited at ~4 Å/min in an oxygen partial pressure of $5x10^{-7}$ torr by co-depositing elemental Co (99.99%, Alfa Aesar) and Fe (99.99%, Alfa Aesar) from thermal effusion cells. The substrate temperature is maintained at 200˚C during CFO growth and *in-situ* reflection high energy electron diffraction (RHEED) is used to monitor the sample surface throughout the growth and annealing process. CFO films are then cooled to room temperature and capped with either Pt, Pt/Cu or Cu. Pt films are deposited at ~0.06 Å/min using an electron beam source while Cu films were grown at 1 Å/min using a thermal effusion cell. The described heterostructures are deposited without breaking UHV conditions in order to preserve the quality of the Pt/CFO and Cu/CFO interface. Magnetization measurements are performed using a Quantum Design 14 Tesla Physical Properties Measurement System (PPMS) with a vibrating sample magnetometer (VSM) module. The samples are patterned into Hall bars (width W=100μm, length L = 800μm) for subsequent DC magnetoresistance and Hall measurements. DC transport measurements are obtained in the same PPMS using a resistivity module. Angle-dependent magnetoresistance (ADMR) measurements are done by placing Hall bars into a constant magnetic field of 10 Tesla and rotating the sample stage.

Structural characterization of a typical CFO film is illustrated in Figure 5.1. Figure 5.1(a) and 1(b) show the RHEED patterns of MgO(5 nm)/MgO(001) and CFO(40

nm)/MgO(5 nm)/MgO(001), respectively, taken along the [110] in-plane directions. Both images display streaky and sharp diffraction maxima, indicating flat and single crystal surfaces. This is confirmed by atomic force microscopy (AFM), which exhibits very smooth morphology over large areas (Figure 5.1c) with an rms roughness of 0.14 nm for a 40 nm CFO film on MgO buffer/MgO(001). The crystallinity is confirmed by θ-2θ x-ray diffraction scans on Pt (1.7 nm)/CFO(40 nm)/MgO(5 nm)/MgO(001), which exhibit clear MgO(002) and CFO(004) peaks and no other diffraction peaks in the scan range (2θ = 0 ° to 90 °) (Figure 5.2 (a)).

The presence of Laue oscillations around the CFO (004) peak indicates well-defined film thickness and sharp interfaces of the CFO film. Further, x-ray reflectivity (XRR) scans give CFO and Pt thicknesses of ~39 nm and ~2 nm, respectively, which are consistent with the designed thicknesses based on quartz deposition monitor (Figure 5.2b).

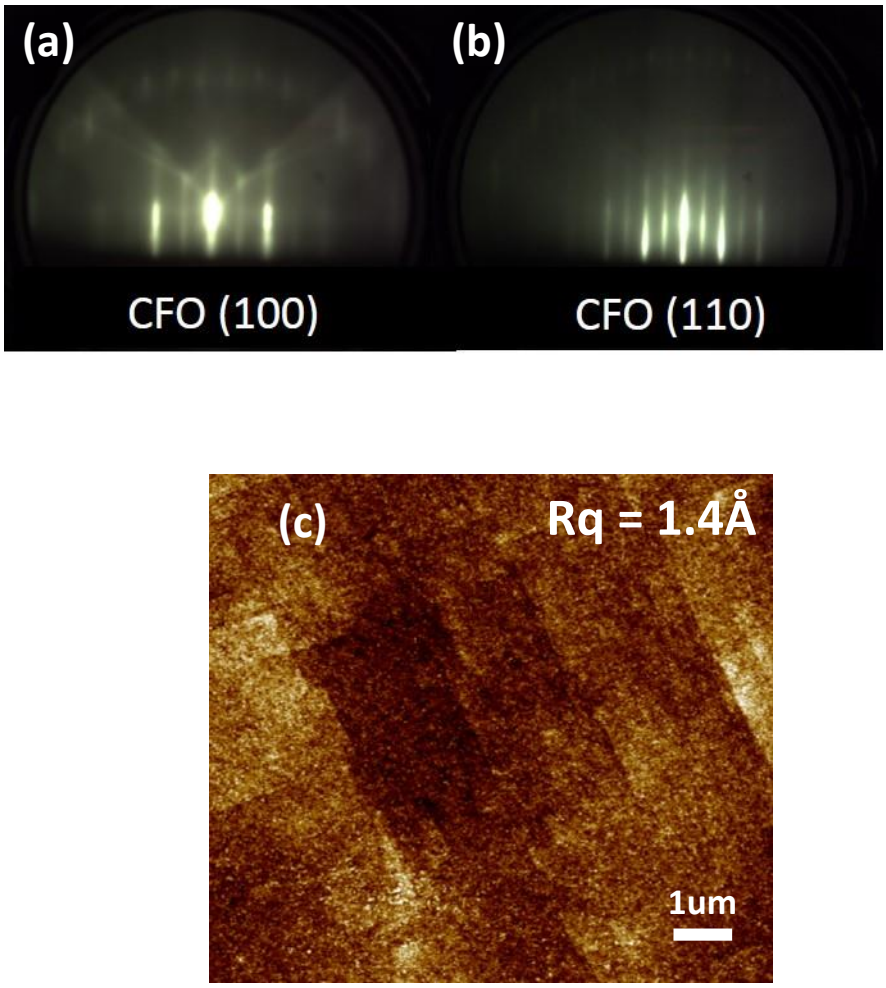

Figure 5.1 (a) RHEED image of $CoFe_2O_4$ in the (100) and (b) (110) directions (c) AFM image of the $CoFe_2O_4$ surface

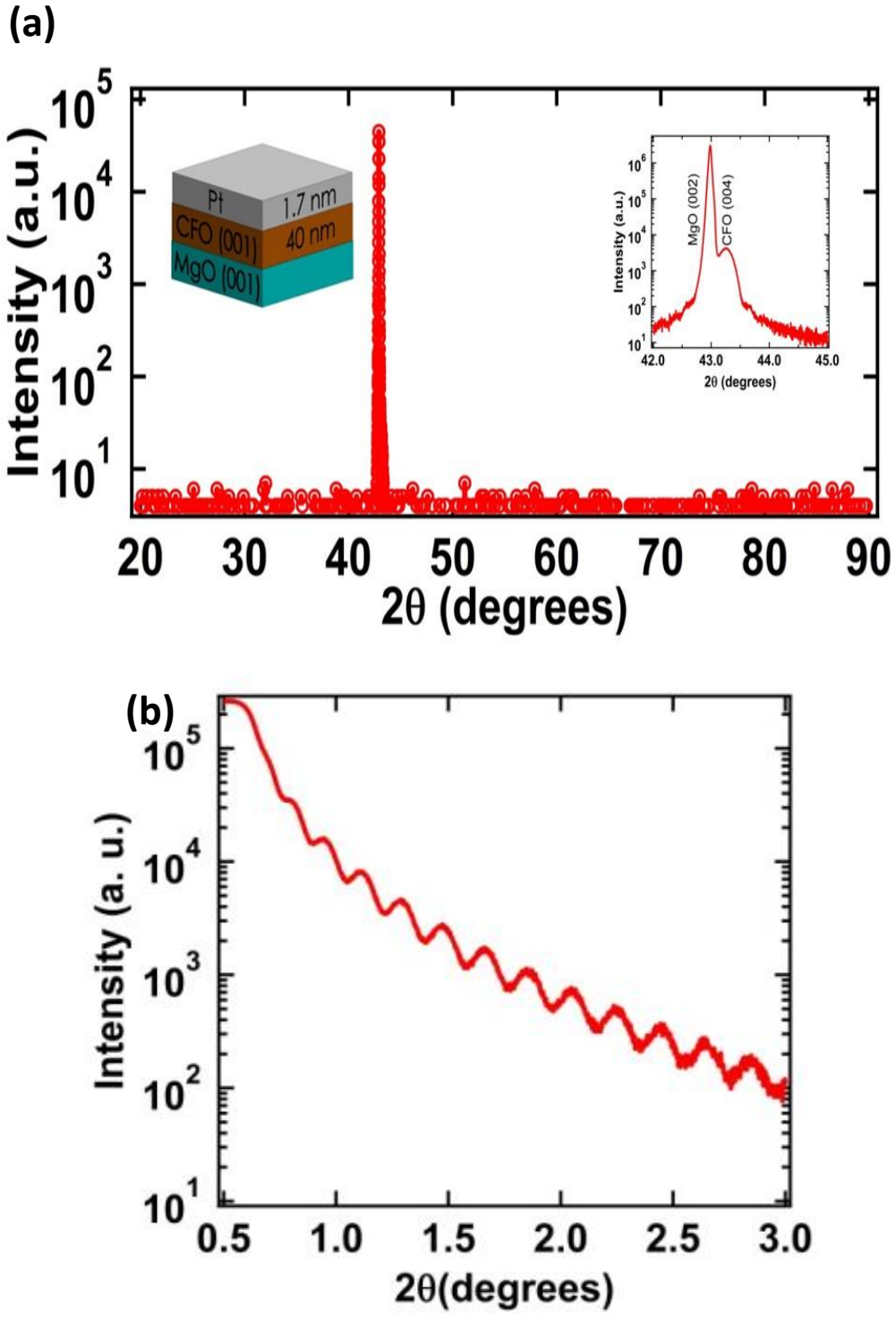

Figure 5.2 (a) X-Ray Diffraction (XRD) of $CoFe_2O_4$ (b) X-Ray Reflectivity (XRR) of $CoFe_2O_4$

Finally, cross-sectional high resolution transmission electron microscopy (HRTEM) has been performed on the sample. These results confirm the high crystallinity of the MBE-deposited CFO films with a smooth Pt/CFO interface (Figure 5.3). Henceforth, all sample are grown on MgO (5 nm)/MgO(001) templates unless otherwise noted.

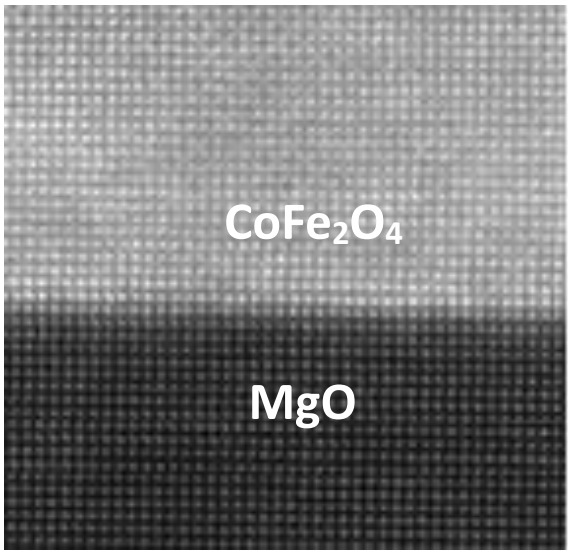

Figure 5.3 (a) TEM image of $CoFe_2O_4$

Figure 5.4 shows in-plane and out-of-plane magnetization loops of Pt (1.1 nm)/CFO(40 nm) samples measured at 5 K. The in-plane loop (red curve) has a coercivity H_C of 0.2 Tesla , saturation field of H_S of ~ 7 Tesla and a remanence ratio M_R/M_S of 0.25. The out-of-plane loop (black curve) has similar characteristics, coercivity H_C of 0.25 Tesla , saturation field of H_S of ~ 7 Tesla and a remanence ratio M_R/M_S of ~ 0.25. These properties indicate a magnetic easy axis which does not lie along the cube edges of the

CFO lattice, likely due to tensile stress applied by the MgO substrate as previously reported in this system [13].

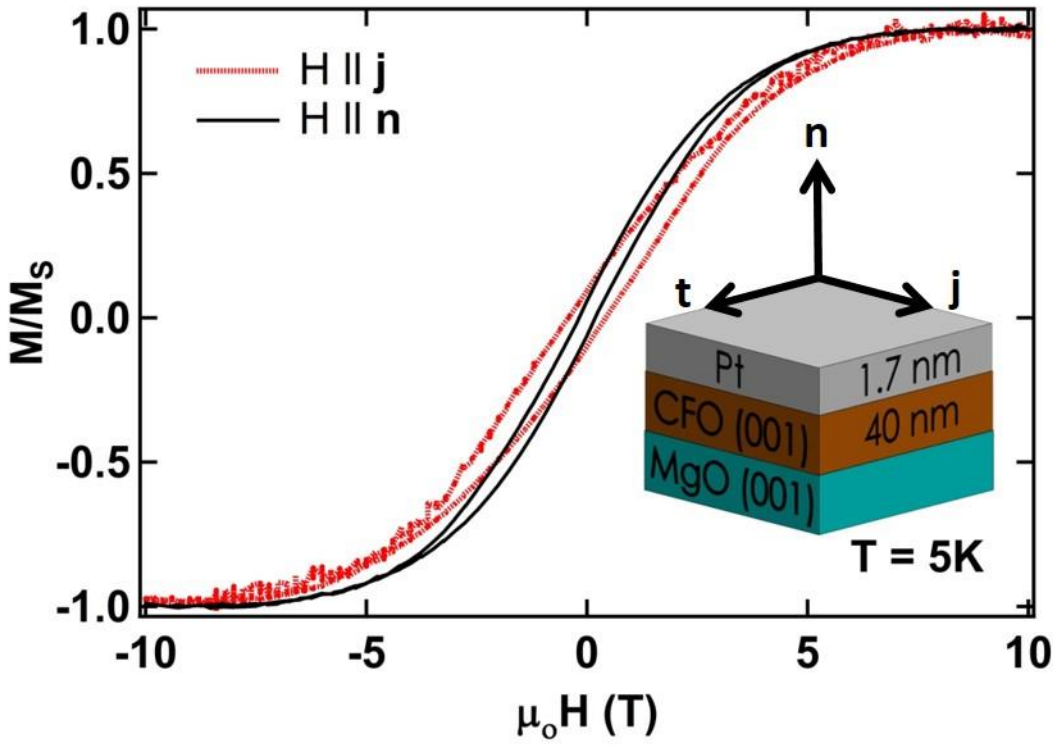

Figure 5.4 VSM in the j (in-plane) and n (perpendicular) direction of $CoFe_2O_4$

5.3 Magneto transport measurement in Pt/$CoFe_2O_4$

To detect MPE in Pt/CFO, our approach is to perform magnetotransport measurements that are sensitive to the presence of magnetization. In ferromagnets, two well-known phenomena are the anomalous Hall effect (AHE) which is sensitive to the out-of-plane magnetization, and the anisotropic magnetoresistance (AMR) which is sensitive to the orientation of magnetization relative to the current direction. With induced

magnetization in the Pt layer along unit vector $\mathbf{m_{Pt}}$, these appear in the longitudinal and transverse resistivities as:

$$\rho_{xx} = \rho_0 + \Delta\rho_{AMR} m^2_{Pt,\,j}\ ,\ \rho_{xy} = \Delta\rho_{AMR}\, m_{Pt,\,t} m_{Pt,\,j} + \rho_{AHE} m_{Pt,\,n} \quad (1)$$

where $m_{Pt,n}$, $m_{Pt,j}$ $m_{Pt,t}$ are the out-of-plane (n), in-plane along current (j), and in-plane transverse to current (t) components of the Pt magnetization unit vector (see Figure 5.4), ρ_0 is the zero-field resistivity of Pt, and $\Delta\rho_{AMR}$ and ρ_{AHE} are the MPE-induced AMR and AHE, respectively. In addition to AHE and AMR, a recently discovered pure spin current effect based on the Spin Hall Effect in Pt and interfacial spin scattering at the FMI interface generates additional contributions to ρ_{xx} and ρ_{xy} given by:

$$\rho_{xx} = \rho_0 + \Delta\rho_1 m^2_{CFO,t}\ ,\ \rho_{xy} = -\Delta\rho_1 m_{CFO,t} m_{CFO,j} + \Delta\rho_2 m_{CFO,n} \quad (2)$$

where $m_{CFO,j}$,$m_{CFO,t,}$ $m_{CFO,n}$ are components of the magnetization unit vector in the FMI, $\Delta\rho_1$ is known as the spin Hall magnetoresistance (SMR), and $\Delta\rho_2$ is known as the spin Hall anomalous Hall-like signal (SH-AHE). The SMR stems from the reflection of spin current generated by spin Hall Effect (SHE) at the FMI interface that is subsequently converted to a charge current through the inverse spin Hall effect (ISHE) [19]. The SH-AHE stems from reflection of the spin current at the FMI interface, where an out-of-plane component of FMI magnetization rotate the spin orientation of the spin current and generate a transverse voltage via ISHE. Finally, in addition to the AMR and SMR effects, one must also consider the ordinary magnetoresistance (OMR) and ordinary Hall effect (OHE) that occur due to the presence of Lorentz forces acting on charge carriers in a magnetic field [20]. This effect has been studied with the possibility of many different effects (OMR, AMR, SMR, OHE,

AHE, SH-AHE) contributing to ρ_{xx} and ρ_{xy}, a systematic approach is essential for identifying the presence of MPE.

We begin by measuring the Hall resistivity of Pt (1.7 nm)/CFO(40 nm) sample at 5 K, as shown in Figure 5.5. For the Hall measurement, we apply a DC current (I = 20 μA) and measure the transverse voltage V_{xy} as an out-of-plane magnetic field is swept. The Hall resistivity is given by $\rho_{xy} = (V_{xy} / I)(Wd/L)$, where W = 100 μm, L = 1 mm, and d = 1.7 nm are the width, length, and thickness of the Pt channel, respectively. Interestingly, for the Pt/CFO sample (green curve) we observe a nonlinear dependence of the Hall voltage with magnetic field superimposed to a linear background. The linear background is due to the OHE, while the nonlinear, hysteretic part of the signal is related to the magnetization of the CFO. To rule out potential artifacts by magnetic fringe field effects, we utilize a Cu (8 nm)/CFO (40 nm) control sample. Cu is a suitable material because its filled *d*-shell prevents induced ferromagnetism (making it insensitive to AHE), and its low spin-orbit coupling prevents spin Hall effects (making it insensitive to SH-AHE). Thus any nonlinear, hysteretic signals would be due to OHE in response to magnetic fringe fields. Figure 5.5 (black curve) shows that the Hall resistivity for the Cu/CFO sample is a linear function of the applied field, which rules out magnetic fringe fields as the origin of the nonlinear, hysteretic signal observed in Pt/CFO. For completeness, we also measure Hall resistivity for Pt/MgO and verify that only the linear contribution from OHE is present (blue curve). It is interesting to note that after the linear OHE contribution is subtracted out (Figure 5.5), the remaining Hall resistivity shows a hysteresis loop with a higher coercivity and

substantially larger remanence than the out-of-plane magnetization loop in Figure 5.4, which indicates that the interfacial magnetism is different from the bulk.

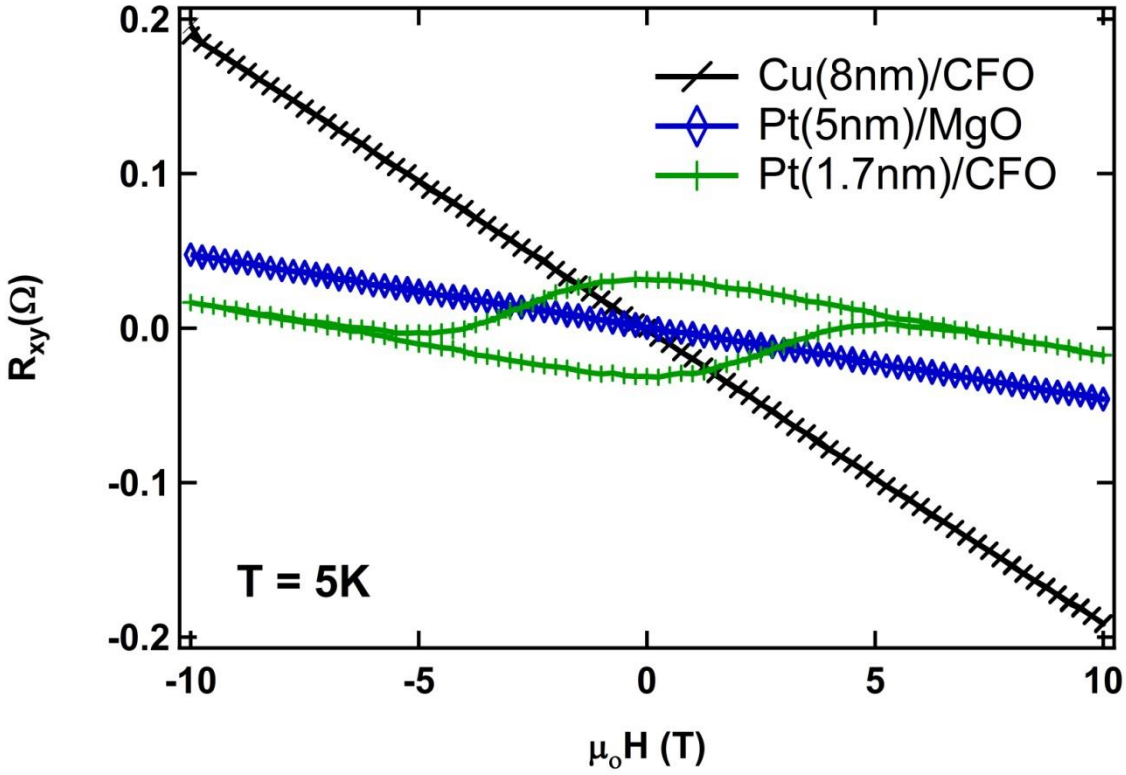

Figure 5.5 (a) Anomalous Hall measurement of Cu/CFO (black curve), Pt/MgO (blue curve) and Pt/CFO (green curve)

One could speculate that this is due to a novel magnetic state due to magnetic interactions between CFO and Pt, but it is still unclear whether the observed Hall signal is primarily from MPE-induced AHE or from SH-AHE.

To clarify this situation, we employ angle-dependent magnetoresistance (ADMR) to separate the contributions from AMR, SMR, and OMR. With a large magnitude of applied field (10 T), the magnetization direction aligns with the applied field. Considering that AMR depends on the *j*-component of magnetization (equation 1) and SMR depends

on the *t*-component of magnetization (equation 2), the two effects can be separated by rotating the magnetization within different planes. For AMR, the relevant angle scan is in the *n-j* plane, where γ is defined as the angle measured from the normal axis (*n*) (see Figure 5.6 a); SMR does not depend on γ. For SMR, the relevant angle scan is in the *n-t* plane, where β is defined as the angle measured from the normal axis (*n*) (see Figure 5.6 b); AMR does not depend on β. Finally, the contribution from OMR has the same functional form as AMR (i.e. depends on γ), but fortunately the OMR has been well studied. OMR in most materials has a larger resistance when the magnetic field is perpendicular to the current (γ = 0) as compared to parallel to the current (γ = 90), and we have verified this for our Pt films on MgO (001) substrates as well. To determine if the Pt/CFO system exhibits MPE, we therefore perform a γ-scan to look for the presence of AMR. Figure 5.6 a (blue curve) shows clearly the presence of angle-dependent MR with low resistivity for γ = 0 and high resistivity for γ = 90. Because this cannot be explained by OMR (and the γ-scan is insensitive to SMR), it is clear proof for AMR and induced ferromagnetism in the Pt layer. This is the strongest evidence for MPE in Pt/CFO in our study. Such an AMR signature has never been observed in previous studies of Pt/CFO, but it has been previously reported for Pt/YIG and is accepted as the most reliable test among transport measurements for MPE [21]. For the SMR, we perform the β-scan and observe SMR with similar magnitude as reported in previous studies (Figure 5.6 b blue curve).

To see if the MPE persist up to room temperature, we repeat the ADMR and Hall measurements at 300 K. The results are shown as the red curves in Figures 5.6 a, b and c. While the Hall resistivity still shows a nonlinear, hysteretic signal (Figure 5.6 c) and the

SMR has a similar magnitude (Figure 5.6 b), the most notable feature is the opposite polarity of the angle-dependence in the γ-scan. Because this has the same polarity as OMR, it is not possible to determine whether this signal is from MPE-induced AMR or from OMR. Thus, we cannot conclude that the MPE persists to room temperature from this data. We therefore turn to another method to characterize MPE in Pt/CFO. We again rely on the fact that Cu has low-spin orbit coupling, long spin diffusion length, and filled d-shell to prevent induced ferromagnetism. This means that inserting a Cu layer into the Pt/CFO interface will produce very different effects for MPE vs. signals generated by spin Hall effects. For spin currents, the Cu layer will be transparent, resulting in little to no change in the SMR and SH-AHE signals. On the other hand, the MPE is very interface sensitive and should be blocked by the presence of a Cu interlayer.

(a)

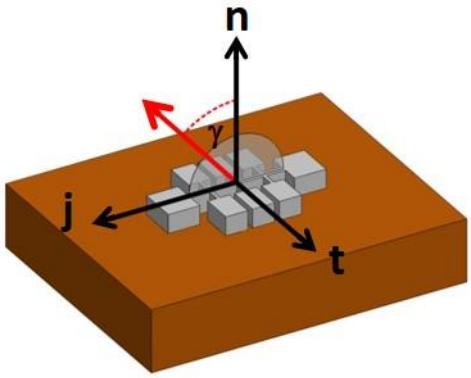

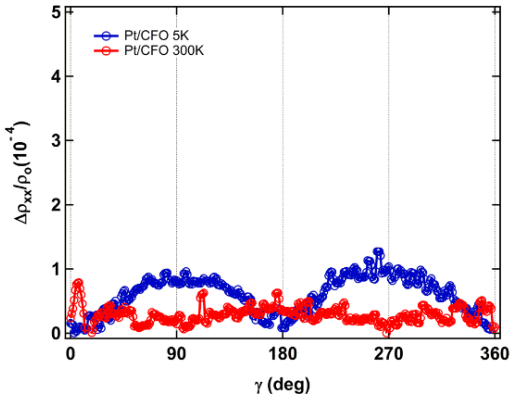

(b)

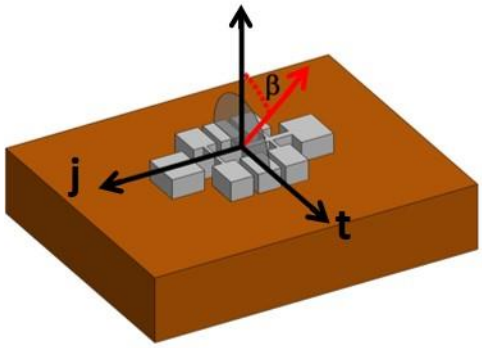

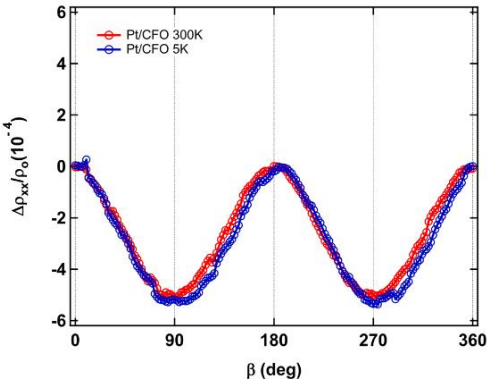

(c)

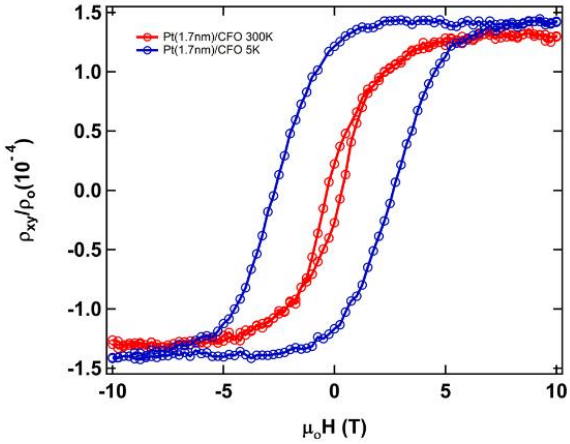

Figure 5.6 (a) Anisotropic magnetoresistance (AMR) (b) Spin Hall Magnetoresistance (SMR) and (c) Anomalous Hall Effect (AHE) of $Pt/CoFe_2O_4$ at 5K and 300 K

Consequently, the removal of MPE by the Cu interlayer should result in changes to ρ_{xx} and ρ_{xy}, thereby providing a method to detect the presence or absence of MPE. Figure 5.7 summarizes the results from this study. Figures 5.7 a, b and c compares the Hall resistivity scan, angle-dependent SMR scan (b-scan), and angle-dependent AMR scan (g-scan), respectively, for Pt(1.7 nm)/CFO(40 nm) vs. Pt(1.7 nm)/Cu(x nm)/CFO(40 nm) at 5 K. Figure 5.7 (a) plots the normalized AHE signal ρ_{xy}/ρ_0 of Pt/CFO and Pt/Cu/CFO. Interestingly, we observe the presence of an AHE signal for the Pt/Cu/CFO that is drastically different than the direct contact Pt/CFO. First, the magnitude ρ_{xy}/ρ_0 of the spacer sample at saturation is ~ 6 times smaller than the direct contact.

(a) (b)

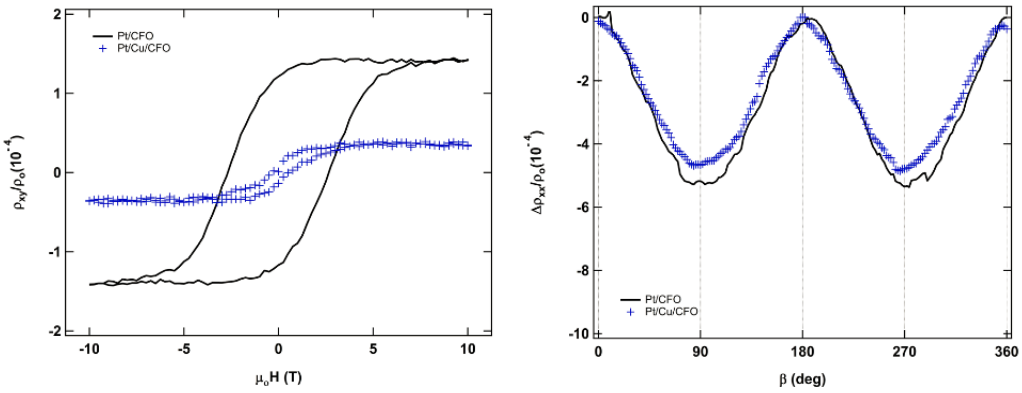

(c)

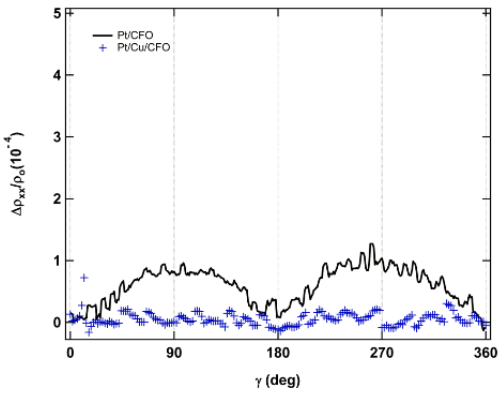

Figure 5.7 (a) AHE (b) SMR and (c) AMR of Pt/$CoFe_2O_4$ and Pt/Cu/CFO at 5K

Second, the coercive field AHE signal with a Cu spacer is H_c=0.3T, which is significantly lower than H_c=2.6 T for direct contact. While shunting through the Cu layer could be responsible of the decrease of the AHE signal, it cannot explain the drastic difference in the coercive fields.

To further ascertain that shunting does not play a significant role in interpreting the normalized Hall data, we measure ADSMR on the Pt/Cu/CFO sample. If shunting through the Cu layer is substantial, we would expect a similar decrease of the SMR signal for Pt/Cu/CFO as compared to the AHE from the Pt/Cu/CFO sample. Figure 5.7(b) shows a plot of the normalized resistivity ratio $\Delta\rho_1/\rho_0$ as a function of angle β for Pt/CFO and Pt/Cu/CFO at 5 K. Surprisingly, the ADMR signal yields the same modulation as the direct contact with the $\Delta\rho_1/\rho_0$ practically unchanged. This suggests that the shunting through the 2 nm Cu layer is properly accounted for in the resistivity ratio plot. Therefore, the substantial decrease of the $\Delta\rho_{xy}/\rho_0$ for the Pt/Cu (2nm)/CFO sample indicates that magnetic proximity effect is dominant in the direct contact Pt/CFO case and the observed $\Delta\rho_{xy}/\rho_0$ signal in the Cu spacer sample arises from the SH-AHE contribution of the SMR. Furthermore, the AHE loop for the Pt/Cu/CFO sample now resembles the magnetization loop extracted from VSM of CFO. This indicates that the intimate contact between the Pt and CFO alter the surface magnetization properties due to magnetic proximity effect. By introducing a Cu spacer, we decouple the Pt from the CFO layer allowing the recovery of the bulk magnetization property as probed by the SH-AHE signal. Overall, the measured AHE signal for the Pt/CFO given by $\rho_{xy} = \rho_{AHE} + \rho_{SH\text{-}AHE}$ where the MPE contribution is more dominant at 5K.

Furthermore, in Figure 5.7 c, we show the AMR signal in the Pt/Cu/CFO bilayer. Indeed, the Pt/Cu (2nm)/CFO sample does not show any modulation arising from the AMR. This further indicates that the Cu spacer suppresses the magnetic proximity effect by decoupling the Pt layer from CFO. The observed AMR for the direct contact Pt/CFO combined with the AHE signal prove undeniably the presence of induced magnetic proximity in our Pt/CFO interface at 5 K.

5.4 Conclusion

In conclusion, we report magnetoresistance and Hall measurements of thin Pt films on the $CoFe_2O_4$ FM insulator grown by Molecular Beam Epitaxy. We observe a sizable magnetic proximity effects (MPE) in Pt thin films revealed by presence of Anisotropic Magnetoresistance (AMR) and Anomalous Hall signals. The coercive field of the AHE signal differs from the $CoFe_2O_4$ substrate, indicating that the interface magnetism plays a very important role in the proximity effect. Through systematic study of the angular dependent Spin Hall Magnetoresistance (ADSMR) and ADAMR, we rule out the presence of artifacts that could produce an AHE-like signal. Furthermore, the AMR and AHE signal are strongly suppressed by introducing a Cu spacer between the Pt and CoFe2O4 allowing us to separate the static and non-equilibrium MPE contributions.

References

1. Håvard Haugen, Daniel Huertas-Hernando, and Arne BrataasPhys. Rev. B 77, 115406 9 (2008)

2. H. X. Yang, A. Hallal, D. Terrade, X. Waintal, S. Roche, and M. Chshiev, Phys. Rev. Lett. 110, 046603 (2013).

3. S. Singh, J. Katoch, T. Zhu, K. Meng, T. Liu, J. T. Brangham, F. Y. Yang, M. Flatte and R. K. Kawakami, arXiv: 1610. 08017 (2016)

4. J. C. Leutenantsmeyer, A. A. Kaverzin, M. Wojtaszek and B. J. van Wees, 2D Materials, 4. 014001 (2016).

5. P. Wei et al., Nature Materials. 10, 1038 (2016).

6. C. Zhao, T. Norden, P. Zhao, Y. Cheng, P. Zhang, F. Sun, A. Taheri, J. Wang, Y. Yang, T. Scrace, K. Kang, S.Yang , G. Miao, R. Sabirianov, G. Kioseoglou, A. Petrou and H. Zeng, arXiv: 1610.04878 (2016).

7. W. Tse, Z. Qiao, Y. Yao, A. H. MacDonald and Qian Niu, Phys. Rev. B 83, 155447 (2011)

8. C. Tang, P. Sellappan, Y. Liu, Y. Xu, J. E. Garay and Jing Shi, Phys. Rev. B 94, 140403 (R) (2016).

9. A. Quindeau, C. O. Avci, W. Liu, C. Sun, M. Mann, A. S. Tang, M. C. Onbasli, D. Bono, P. M. Voyles, Y. Xu, J. Robinson, G. S. D. Beach and C. A. Ross, Adv. Electron. Mater 3, 1600376 (2017)

10. A. V. Ramos, Ph.D Thesis. Universite Pierre et Marie Curie - Paris VI (2008).

11. U. Lüders, A. Barthélémy, M. Bibes, K. Bouzehouane, S. Fusil, E. Jacquet,J. Contour, J. Bobo, J. Fontcuberta and Albert Fert, Adv. Mater, 18, 1733-1736 (2006).

12. X. Chen, X. Zhu, W. Xiao, G. Liu, Y. P. Feng, J. Ding and R. Li, ACS Nano 9, pp 4210-4218 (2015).

13. G. Hu, J. H. Choi, C. B. Eom, V. G. Harris and Y. Suzuki, Phys. Rev. B 62, R779 (R) (2000).

14. M. Isasa, A. Bedoya-Pinto, S. Vélez, F. Golmar, F. Sánchez, L. E. Hueso, J. Fontcuberta, and Fèlix Casanova, Applied Physics Letters 105, 142402 (2014).

15. M. Valvidares, N. Dix, M. Isasa, K. Ollefs, F. Wilhelm, A. Rogalev, F. Sánchez, E. Pellegrin, A. Bedoya-Pinto, P. Gargiani, L. E. Hueso, F. Casanova, and J. Fontcuberta, Phys. Rev. B 93, 214415 (2016).

16. H. Wu, Q. Zhang, C. Wan, S. S. Ali, Z. Yuan, L. You, J. Wang, Y. Choi, and X. Han,IEEE Trans. Magn.51, 4100104 (2015).

17. J.-B. Moussy, S. Gota, A. Bataille, M.-J. Guittet, M. Gautier-Soyer, F. Delille, B. Dieny, F. Ott, T. D. Doan, P. Warin, P. Bayle-Guillemaud, C. Gatel, and E. Snoeck, Phys. Rev. B 70, 174448 (2004).

18. W. Eerenstein, T. T. M. Palstra, T. Hibma, and S. Celotto, Phys. Rev. B 68, 014428 (2003)

19. Y. Chen, S. Takahashi, H. Nakayama, M. Althammer, S. T. B. Goennenwein, E. Saitoh and G. E. W. Bauer, Phys. Rev. B 87, 144411 (2013).

20. Miren Isasa, Saül Vélez, Edurne Sagasta, Amilcar Bedoya-Pinto, Nico Dix, Florencio Sánchez, Luis E. Hueso, Josep Fontcuberta, and Fèlix Casanova, Phys. Rev. Applied **6**, 034007

21. S. Y. Huang, X. Fan, D. Qu, Y. P. Chen, W. G. Wang, J. Wu, T. Y. Chen, J. Q. Xiao, and C. L. Chien, Phys. Rev. Lett. 109, 107204 (2012).

Chapter 6: Large Area Epitaxial Germanane for Electronic Devices

Abstract

We report the synthesis and transfer of epitaxial Germanane (GeH) onto arbitrary substrates by electrochemical delamination and investigate its optoelectronic properties. GeH films with thickness ranging from 1 nm to 600 nm (2-1000 layers) and areas up to ~1 cm^2 have been reliably transferred and characterized by photoluminescence, x-ray diffraction, and energy-dispersive X-ray spectroscopy. Wavelength dependent photoconductivity measurements on few-layer GeH exhibit an absorption edge and provide a sensitive characterization tool for ultrathin germanane materials. The transfer process also enables the possibility of integrating germanane into vertically stacked heterostructures.

6.1 Introduction

Graphene, a single atomic sheet of carbon, has been a revolutionary material with unique properties for electronics, spintronics, and surface science [1-5]. Recently there has been intense interest in two-dimensional (2D) materials beyond graphene that have a native band gap and stronger spin-orbit coupling [6-9]. Germanane, the germanium analog of graphane (i.e. hydrogen-terminated graphene), is a new 2D material with a direct band gap that can be tuned via surface covalent functionalization [9-11]. Additionally, germanane is air stable and has a high predicted mobility of 18,000 cm^2/Vs at room temperature, making it extremely promising for electronic and optoelectronic applications [9]. Specifically, the combination of high mobility, non-zero bandgap, and low dimensionality are advantageous for short channel field effect transistors (FETs) with high on-off ratios and low quiescent currents [7]. Furthermore, germanane's large spin orbit coupling makes it possible to explore novel physical phenomena such as quantum spin Hall effect at room temperature [12-14].

It is worthwhile to compare the general band structure characteristics of germanane (with hydrogen termination) and germanene (without hydrogen termination) [15-18] . Germanene has a band structure similar to graphene, with Dirac cones at the ±K points of the Brillouin zone and conduction electron Bloch states composed primarily of p_z orbitals. The main difference is the larger spin-orbit coupling due to the larger mass of Ge compared to C, producing a spin orbit gap of ~24 meV at the ±K points (compared to 24-50 μeV for graphene) [19]. When a germanene sheet is modified by covalently bonding hydrogen atoms to both sides, one obtains germanane (GeH). The covalent bonding involves the p_z

orbitals of the Ge atom and causes a substantial gap to open at the ±K points, so the electron transport properties are no longer determined by the Bloch states involving the p_z orbitals. Instead, transport is determined by the Bloch states near the Γ point, with a conduction band derived from s-orbitals and a valence band derived from the p_x and p_y orbitals [9]. The direct gap band structure is rather similar to conventional semiconductors such as GaAs with an *s*-orbital conduction band and *p*-orbital valence bands, except that the p_z orbital is removed by the covalent bonding with the hydrogen. Thus, numerous properties of conventional direct gap semiconductors will translate to germanane, including spin-selective optical selection rules, contact hyperfine coupling in the conduction band, and spin-orbit splitting in the valence band [20].

Recently, large area germanane films have been synthesized by growing Zintl-phase $CaGe_2$ thin films on Ge(111) wafers by molecular beam epitaxy (MBE) [21] or substrate reaction [22,23], followed by chemical processing in acid solution to convert the $CaGe_2$ into hydrogen-terminated germanane (GeH). In order to utilize this material for electronic devices, it is necessary to transfer the GeH film to an insulating substrate to prevent parallel conduction paths. In addition, a transfer process will allow the integration of GeH into vertically stacked heterostructures with other 2D materials. In this paper, we report the synthesis and transfer of large area epitaxial GeH by electrochemical delamination (i.e. "bubble transfer") and demonstrate electron transport and photoconductivity. We are able to reliably transfer films up to ~1 cm^2, which is limited by the size of our sample holder. The photoluminescence (PL) spectra and the x-ray diffraction scans (XRD) remain largely unchanged by the transfer process, indicating that the optical

and bulk structural properties are maintained. Furthermore, energy-dispersive X-ray spectroscopy (EDS) shows no residual electrolyte (within measurement sensitivity) remaining from the transfer process. We investigate electron transport and photoconductivity by transferring to insulating substrates and depositing metallic electrodes through shadow masks. In particular, photoconductivity of few-layer GeH exhibits an absorption edge as a function of wavelength as expected for a semiconductor. Because most other techniques for characterizing germanane have required thick films or bulk crystals, the demonstration of photoconductivity measurements on few layer GeH is very important for the further optimization and development of ultrathin germanane materials.

6.2 Growth of epitaxial Germanane films

The first step is to deposit Zintl-phase $CaGe_2$ films on Ge(111) substrates by molecular beam epitaxy (MBE) in an ultrahigh vacuum (UHV) chamber (base pressure of $2x10^{-10}$ torr) [21]. Elemental germanium and calcium are evaporated from thermal effusion cells with high purity germanium (99.9999% from Alfa Aesar) and calcium (99.99% from Sigma Aldrich) source materials. Growth rates are determined by a quartz deposition monitor. All films are grown on p-type Ge (111) single-side polished wafer with thickness of ~0.350 mm and orientation tolerance of 0.5° (University Wafer). The starting 2" diameter wafer is cleaved into smaller pieces (up to 10 mm) which then undergo chemical etching to remove surface oxides and metal contaminants. Etching involves a sequence of steps beginning with immersion in a solution of H_2O:NH_4OH (10:1) for 60 sec, followed by H_2O:H_2SO_4 (10:1) for 60 sec. Finally the substrate is submerged into 30% H_2O_2 aqueous

solution for 60 sec to produce a thin protective oxide layer. The wafers are then rinsed with de-ionized water, blown dry with nitrogen gas, and inserted into the UHV chamber where a 30 min anneal at 650° C removes the protective oxide layer.

The MBE growth of $CaGe_2$ is performed at 750° C in an adsorption-limited growth regime. The typical Ca:Ge flux ratio is held slightly above 0.5 for slightly Ca-rich conditions. Excess Ca atoms are either re-evaporated or possibly reacted into the Ge substrate. Assuming that the growth rate is determined by the Ge flux, typical growth rates for the $CaGe_2$ are ~ 3 Å/min for films thinner than 200 nm and ~15 Å/min for films thicker than 200 nm. In both cases, sharp and streaky reflection high energy electron diffraction (RHEED) patterns are obtained [21]. These patterns indicate that the $CaGe_2$ film maintains epitaxial orientation with the Ge (111) substrate.

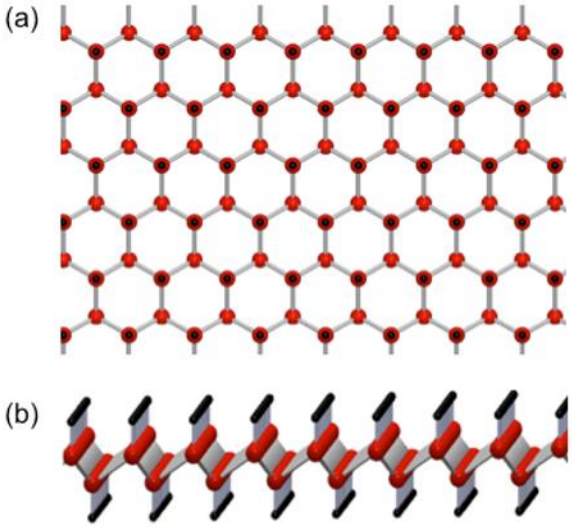

Figure 6.1. (a) Top view of GeH, (b) Side view of GeH.

Subsequently, the $CaGe_2$/Ge(111) is removed from vacuum and submerged in a 37% solution of HCl for 24 to 48 h at -40° C depending on sample thickness. This de-intercalates the calcium atoms and replaces them with covalently bonded hydrogen atoms to produce 2D stacked layers of GeH [9,21,22]. As shown in Figure 6. 1, the Ge atoms form a buckled honeycomb structure and each of the Ge atoms is bonded to a hydrogen atom for sp^3 hybridization. The (001) lattice parameter is expanded during the de-intercalation of $CaGe_2$ to GeH by 7% [9], leading to slightly thicker GeH films. Unless otherwise noted, the reported thicknesses are those of the final GeH film. For films less than 50 nm, thicknesses were determined by AFM, whereas for thicker films, the reported values are based on growth rates. Details of the MBE growth and chemical processing are provided in ref [21].

The morphology of the resulting GeH film depends on the sample thickness. Samples thinner than 10 nm (~18 layers) have relatively smooth surfaces with island or terrace formation due to the substrate miscut [21], while samples thicker than 50 nm (~88 layers) display the formation of cracks (Figure 6.3 ©). These cracks form during the growth of the $CaGe_2$ film and are probably related to the 1% lattice mismatch with the Ge(111) substrate [23], where defects and dislocations form beyond a critical thickness in order to relax substrate-induced strain. While there is considerable room to improve the quality of the films, we note that the large area transfer has worked reliably in spite of these imperfections.

6.3 Large area transfer

To realize germanane-based electronic devices, it is necessary to transfer the GeH film to an insulating substrate. Our initial attempts at transferring the GeH film included mechanical exfoliation using various tapes and polydimethylsiloxane (PDMS) stamping procedures. However, these methods resulted in low yield and small flake size (< 10 μm). A popular method for transferring large area 2D films is to support the film with polymer and etch away the underlying substrate, which is commonly used to remove copper foil from CVD graphene [24].

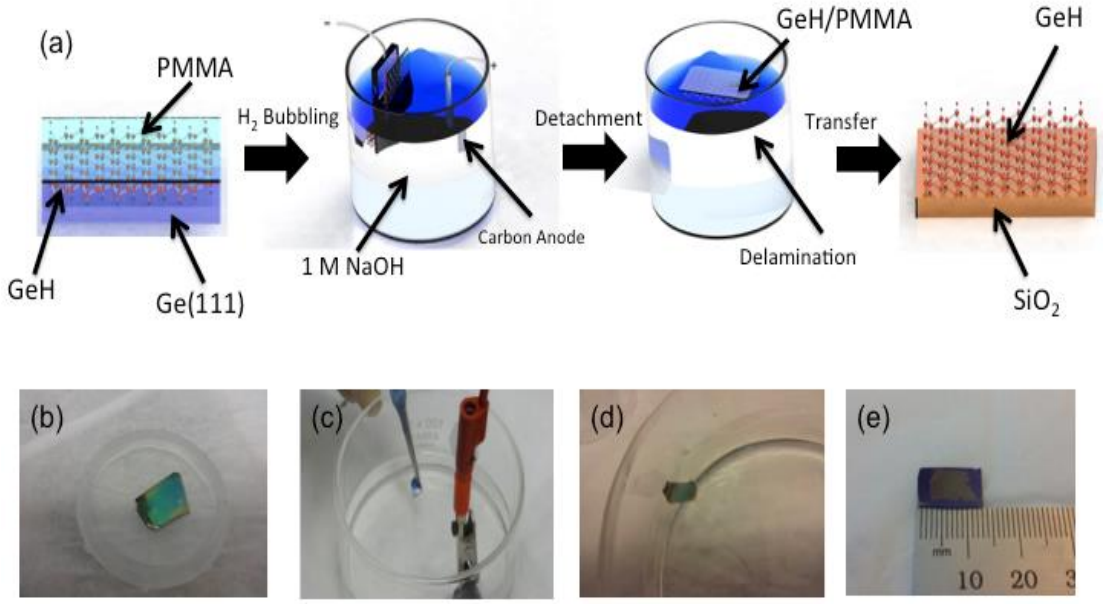

Figure 6.2. (a) Schematic of the transfer process, (b) Optical image of PMMA/GeH/Ge(111), (c) Optical image of the electrochemical cell, (d) Optical image of the floating PMMA/GeH film (e) Optical image of GeH transferred to SiO_2.

However, we are not aware of a selective etch that differentiates between GeH and Ge. Therefore, we focus our attention to electrochemical delamination based on water

electrolysis, i.e. bubble transfer [25,26], which has been effective for transferring other 2D materials.

Figure 6.2 (a) illustrates the main steps for the transfer and Figures 6. 2b-2e are photographs taken during the process. Beginning with a GeH film on a p-type Ge (111) substrate (Figure 6. 2 (b)), we spin coat the sample with polymethylmethacrylate (PMMA) at 2000 rpm for 45 sec and then bake at 50°C for 2 hr. The PMMA coating of GeH provides structural support during the delamination process. To facilitate detachment during the water electrolysis, the PMMA on the edge of the substrate is removed with acetone. Then, we dip the PMMA/GeH/Ge(111) cathode and a graphite anode into a 1M NaOH aqueous solution and slowly increase the current at a typical rate of ~0.01 A/sec (Figure 2c) until the PMMA/GeH starts to detach. The current produces H_2 bubbles at the interface between the PMMA/GeH and the Ge(111) due to water reduction ($2H_2O + 2e^- \rightarrow H_2$ (g) + $2OH^-$ (aq)). The hydrogen bubbling time necessary to detach the PMMA/GeH layer from the Ge substrate depends on the size of the film and the current applied. Typically, after approximately 10 s of bubbling, the PMMA/GeH layer floats to the top of the NaOH solution (Figure 6.2 (d)). The corresponding electrolyte voltage is approximately 5 V with a current of ~0.06 A for a 1 cm^2 sample. The PMMA/GeH is then moved to a bath of de-ionized (DI) water for 15 min to remove the remaining electrolytes from the sample. After cleaning, we transfer the PMMA/GeH layer to the desired substrate and bake on a hot plate at 50° C for 10 min to help remove the interfacial water layer. The residual PMMA is removed by immersing the transferred sample in acetone at 50° C for 30 min, followed by

an isopropanol rinse for one minute to remove the acetone. Finally, we dry the sample with nitrogen gas. Figure 6.2 (e) shows a transferred film with a size of several mm.

We have successfully transferred GeH films between 1 nm (2-3 layers) and 600 nm (~1000 layers) thicknesses to arbitrary substrates. Figure 6.3 shows optical and scanning electron microscope (SEM) images of 5 nm (~9 layers) GeH films transferred to a SiO_2(300 nm)/Si substrate.

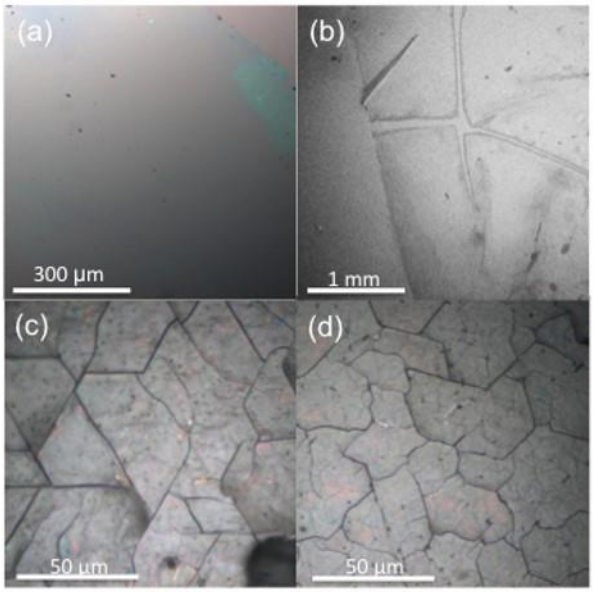

Figure 6.3. (a) Optical micrograph of 5 (~9 layers) nm GeH transferred to SiO_2, (b) SEM image of 5 nm (~9 layers) GeH transferred to SiO_2, (b) Optical micrograph of 600 nm (~1000 layers) as grown GeH on Ge(111), (d) Optical micrograph of 600 nm (~1000 layers) GeH transferred to SiO_2.

The optical image (Figure 6. 3 (a)) shows a continuous large area of GeH. The upper right corner of the image shows the edge of the film, which is visible due to color contrast with the bare substrate. The SEM image (Figure 6.3 (b)) shows continuous regions

larger than ~1 mm and separated by tears, which produce enhanced contrast between the substrate and film. The continuous regions are typically larger and exhibit fewer features (Supplementary Figure 6.S4).

For the thicker GeH, we observe similar cracking before transfer (Figure 6. 3 (c)) and after transfer (Figure 6. 3 (d)), which shows that the morphology is conserved.

To determine the effect of the transfer on the quality of GeH films, we perform a series of characterization measurements before and after transferring. To minimize substrate-related effects, we transfer the GeH film from its original Ge (111) substrate to another Ge (111) substrate. The out-of-plane lattice spacing was analyzed using XRD on a 600 nm (~1000 layers) GeH film. Before transfer, we observe a peak at $2\theta = 15.8°$ which corresponds to the GeH layer spacing of 5.7 Å. This is in agreement with XRD characterizations of bulk GeH crystals, where synchrotron-based measurements of the pair distribution function have confirmed the buckled honeycomb structure of the GeH layers [10]. As shown in Figure 6. 4d, the position and line width of the GeH peak are preserved after transfer, indicating that the transfer does not produce major changes to the crystal structure.

To investigate the effect of transfer on optical properties, we perform PL spectroscopy at low temperatures (10 K). PL is performed using a 532 nm laser excitation (1 mW, 20 μm spot size) and the spectra are captured using a 0.5 meter Czerny-Turner spectrometer with a liquid nitrogen cooled CCD camera (Princeton Instruments). A white light source (tungsten lamp modeled as a blackbody) is used to calibrate and correct for the wavelength dependence of the detector efficiency. The PL spectrum before transfer

exhibits a peak at ~1.45 eV, (Figure 6. 4 (c)) which is consistent with previous reports of PL on epitaxial GeH [22]. After transfer, the PL spectrum again exhibits a peak at ~1.45 eV and the intensity is not degraded (Figure 6. 4d). Notably, we did not observe photoluminescence at ~1.9 eV, which is reported to occur in the presence of oxidation [22]. This suggests that the transfer of GeH does not promote oxidation and preserves the optical quality.

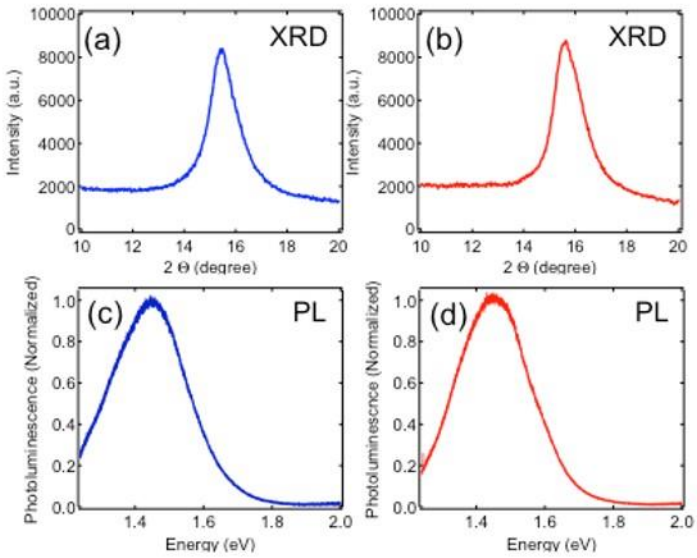

Figure 6.4. (a) XRD of as-grown 600 nm (~1000 layers) GeH film, (b) XRD of transferred 600 nm (~1000 layers) GeH film, (c) PL of as-grown 600 nm (~1000 layers) GeH film, (d) PL of transferred 600 nm (~1000 layers) GeH film.

Finally, we have examined the possible contamination of a 600 nm thick sample during the transfer using EDS spectroscopy (Oxford Instruments) in an SEM at 20 kV (1000 nm penetration depth). The spectrum before transfer shows a strong Ge signal and no observable Ca and O signals (Supplementary Figure 6. S1). In addition, we performed

low energy 10 kV (340 nm penetration depth) EDS and observed some surface oxidation (Supplementary Figure 6. S2). The Cl remaining in the material after deintercalation is about 7%, similar to what has been reported previously [10,22]. After transfer, the 20 kV EDS spectra was free of Na and O signals (Supplementary Figure 6. S1). This confirms that the transfer introduces little or no contamination (below detection limits) to the GeH film.

Electron transport and photoconductivity

To investigate the electrical and photoconductive properties of GeH films on the SiO_2(300 nm)/Si substrate, we deposit metallic electrodes through shadow masks. For thicker films (>50 nm), we utilize a shadow mask with fine features in order to have a continuous conduction channel in between the cracks. Figure 6.5a is an optical microscope image of a 600 nm (~1000 layers) GeH film with Au/Ti electrodes separated by 20 μm. DC photoconductivity is measured by applying a voltage between the drain and source and measuring the current under illumination by a 635 nm laser. A factor 50 increase in current from dark is observed when illuminated by 0.014 W/cm^2 635 nm light (Supplementary Figure 6. S3).

Wavelength dependent AC photoconductivity measurements are performed using pulsed laser excitation (150 fs, 76 MHz repetition rate) from a Ti:sapphire oscillator (700 nm – 960 nm wavelength range) or optical parametric oscillator (520 nm – 740 nm wavelength range). The laser beam is maintained at a power of 1.0 mW and has a beam diameter of ~2 mm.

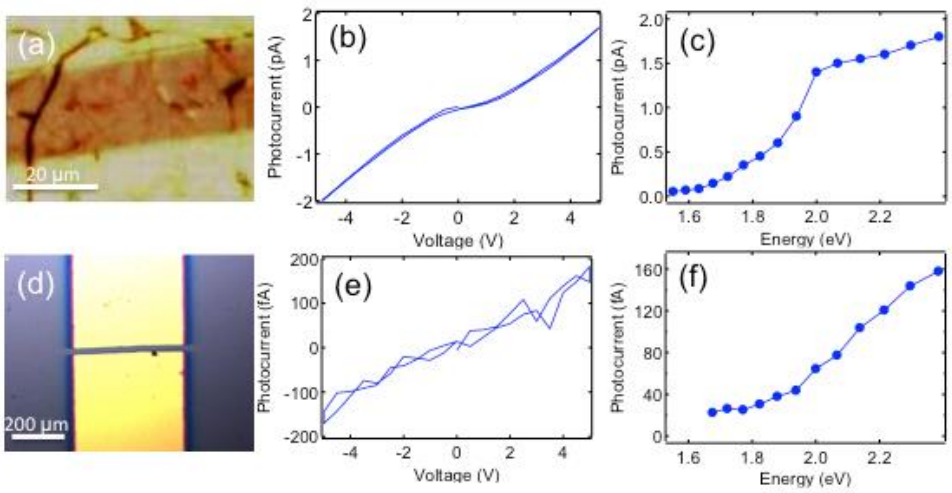

Figure 6.5. (a) Optical micrograph of a 600 nm (~1000 layers) GeH device, (b) Bias dependence of photocurrent for the 600 nm (~1000 layers) GeH device illuminated by 540 nm light, (c) Wavelength dependence of photocurrent at 5 V bias for the 600 nm (~1000 layers) GeH device, (d) Optical micrograph of a 5 nm (~9 layers) GeH device, (e) Bias dependence of photocurrent for the 5 nm (~9 layers) GeH device illuminated by 540 nm light, (f) Wavelength dependence of photocurrent at 5 V bias for the 5 nm (~9 layers) GeH device.

The beam is incident on the device without a focusing lens, thereby producing a broad illumination with an intensity of ~0.03 W/cm^2. The beam is chopped at a frequency of 493 Hz and the resulting photocurrent is pre-amplified and measured by lock-in detection. All photocurrent measurements are performed at room temperature.

Figure 6.5 (b) shows the photocurrent of a 600 nm (~1000 layers) GeH device as a function of bias voltage for a laser wavelength of 540 nm. The bias voltage is ramped from 0 V to +5 V to -5 V to 0 V to detect possible hysteretic effects as a function of bias voltage. The photocurrent vs. voltage curve exhibits no hysteresis and is slightly nonlinear. We investigate the wavelength dependence of the photocurrent by adjusting the laser wavelength and repeating this measurement every 20 nm. Figure 6.5 (c) summarizes the

wavelength dependence by plotting the photocurrent at +5 V bias. At low photon energies, there is little photocurrent because the photon energy is below the band gap. As the photon energy is increased, more photons are absorbed and the photocurrent increases. This behavior is typical of a semiconductor, where the absorption rapidly increases as the photon energy exceeds the band gap and is similar to recent measurements on bulk germanane crystals [27]. We note that this photocurrent spectrum is also similar to previous optical reflectance spectroscopy performed on epitaxial GeH/Ge(111) [28].

To develop few-layer germanane devices, we next focus our attention on the characterization of thin GeH films (~5 nm). However, initial studies on thin GeH failed to produce consistent results, and we hypothesized that the problem was oxidation of the $CaGe_2$ film due to air exposure prior to de-intercalation. To prevent such difficulties, we added an extra step in the synthesis procedure, in which we grew 5 nm Ca followed by 10 nm Fe to cap the $CaGe_2$ film prior to de-intercalation. This minimizes the potential oxidation of the $CaGe_2$ layer as the sample is transferred in air from the MBE chamber to the HCl solution [22]. Once inside the HCl solution, the Fe and Ca layers are dissolved, and then the underlying $CaGe_2$ film is de-intercalated to produce GeH. After de-intercalation, we performed EDS to ensure that the capping layer is completely removed (below detection limit) and the $CaGe_2$ is converted to GeH (Supplementary Figure 6. S7). Because these films are continuous, we deposit larger metallic electrodes of width 400 μm and separated by a 20 μm gap. Figure 6.5 (d) is an optical microscope image of such a device with GeH film thickness of 5 nm (~9 layers). Figure 6.5 (e) shows the photocurrent of this device as a function of bias voltage under laser illumination at 540 nm. There is an

order of magnitude less photocurrent for this device compared to the thick GeH and the signal is approaching the level of the noise. Compared to the thicker films which exhibit non-linear IV (Figure 6.5 (b)), the thinner films have more linear IV characteristics and the photoconductivity can be quantified by a linear fit. The linear IV may be associated with improved contacts due to the Fe capping procedure (i.e. reduced oxidation as confirmed by EDS in Supplementary Figure 6.S7), but systematic studies have not yet been performed. The photocurrent spectrum shown in Figure 5f displays the expected behavior for a semiconductor, with low photocurrent at low photon energies and an increase of photocurrent with increasing photon energy. Although the absorption edge appears to have shifted to slightly higher energies compared to the thick device (Figure 6.5 (c)), the overall features of the photoconductivity spectra are similar. We have also observed photoconductive signals in 1 nm (2-3 layers) GeH films (see Supplementary Materials).

The ability to measure these weak photoconductivity signals is very important for the optimization of few-layer germanane films. Up until now, the most important materials characterizations such as XRD and PL could only be applied to thick GeH films due to the lack of measurable signal in the thinner films. Now with the photoconductivity measurement, we have a means of characterizing the electronic and optical properties of few-layer germanane and can use this information to optimize the material synthesis procedures.

Conclusion

We developed the synthesis and transfer of GeH onto arbitrary substrates. This is an important advance, as the transfer of GeH enables the fabrication of electronic devices on insulating substrates, optical studies on transparent substrates, as well as the creation of vertically stacked 2D heterostructures. We verified that the structural and optical properties of thick GeH films are largely unchanged by the transfer process with PL and XRD. Additionally, the transfer process does not contaminate the thick GeH films with residual electrolytes (within measurement sensitivity), verified with EDS spectroscopy. Once transferred, GeH films were fabricated into two-terminal devices to allow transport measurements and photoconductivity measurements. The photoconductivity of both thick and few-layer GeH indicates an absorption edge as a function of wavelength, as expected for a semiconducting material. The photoconductivity measurements on few-layer GeH are particularly important for the further optimization and development of ultrathin germanane materials due to its high sensitivity. These results represent a major advance toward the realization of electronic and optoelectronic applications in this emerging 2D material.

Supplementary information:

Energy dispersive x-ray spectroscopy (EDS) is performed using an Oxford Instruments INCA EDS platform under SEM (Figure S1a). The electron acceleration voltage is 20 kV (1000 nm penetration depth). Elemental analysis of the as-grown sample shows a chlorine residue of 7.23% and a germanium composition of 92.77% (Figure S1b). The transferred sample shows similar amounts of Cl and Ge (Figures S1c). We did not

observe any residues from the electrolysis process (below detection limit). In addition, we perform EDS analysis at 10 kV (340 nm penetration depth) to probe the as-grown GeH (Figure S2) and observe oxidation of 17.24%.

(a)

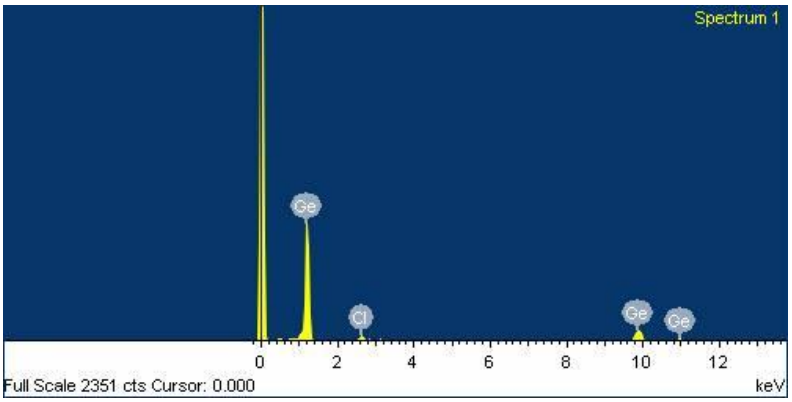

(b)

Element	App Conc.	Intensity Corrn.	Weight%	Weight% Sigma	Atomic%
Cl K	2.01	0.6671	3.67	0.75	7.23
Ge K	78.39	0.9924	96.33	0.75	92.77
Totals			100.00		

(c)

Element	App Conc.	Intensity Corrn.	Weight%	Weight% Sigma	Atomic%
Cl K	1.95	0.6671	3.64	0.75	7.18
Ge K	76.76	0.9925	96.36	0.75	92.82
Totals			100.00		

Supplementary Figure 6.S1: (a) EDS spectrum of as-grown 600 nm (~1000 layers) GeH at 20 kV, (b) Elemental analysis of the as-grown GeH at 20 kV, (c) Elemental analysis of the transferred GeH at 20 kV

Element	App Conc.	Intensity Corrn.	Weight%	Weight% Sigma	Atomic%
O K	0.93	2.0717	4.70	2.46	17.24
Cl K	0.62	0.9666	6.74	1.64	11.16
Ge L	8.04	0.9538	88.56	2.79	71.60
Totals			100.00		

Supplementary Figure 6.S2: EDS elemental analysis of the 600 nm (~1000 layers) as-grown GeH sample at 10 k

Photoconductivity Measurement

DC I-V measurements are performed with a Keithley 6514 Electrometer (Figure S3). A DC voltage is swept between drain and source, and the current is measured. The wait time between each data point is about 3 min to reach a steady state. The DC photoconductivity measurement is carried out with a red laser (635 nm, ~3 mm diameter spot).

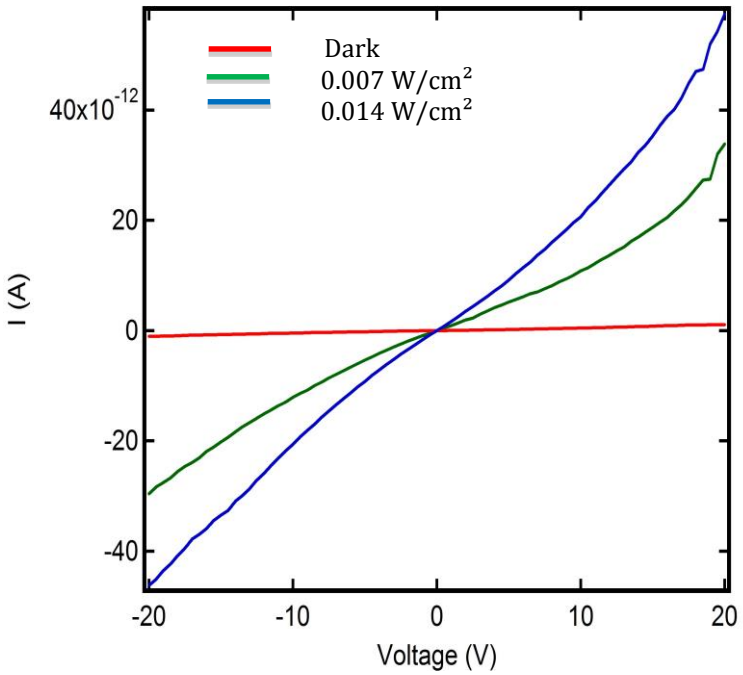

Supplementary Figure 6.S3: IV measurement for different laser powers

SEM images of 2 nm (3-4 layers) GeH on SiO_2 are taken with a Leo SUPRA 55 at 5 kV energy (Figure S4). Large areas without tears are typically observed. The dark black dots on top of the large area GeH are most likely PMMA residue due to the bubble transfer process.

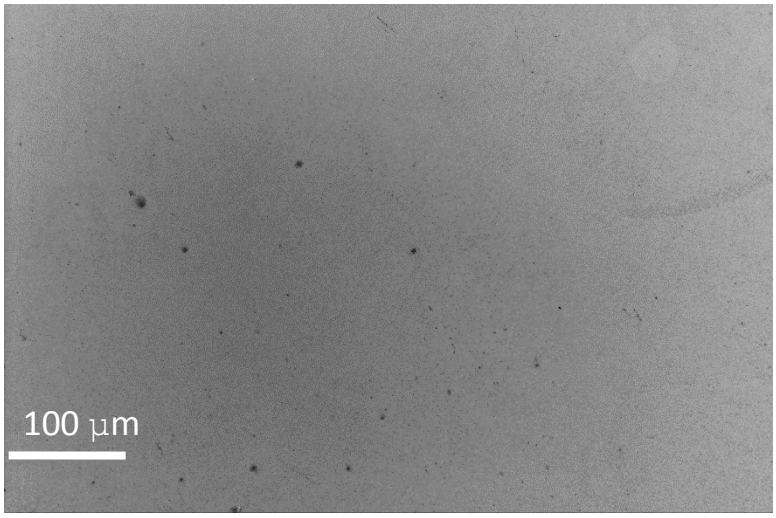

Supplementary Figure 6.S4: SEM image of 5 nm (~9 layers) GeH on SiO_2

Below is an optical microscope image of 1 nm (2-3 layers) GeH transferred to SiO_2/Si substrate under 10x magnification. The light blue area corresponds to the 1 nm (2-3 layers) GeH and the top left area is SiO_2. The thickness is characterized by AFM.

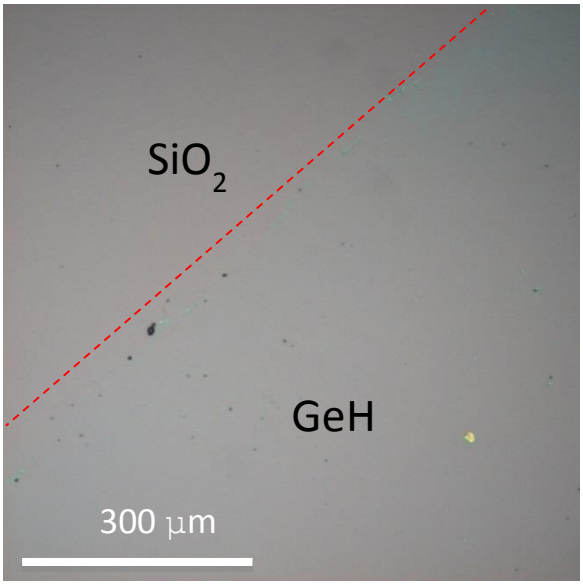

Supplementary Figure 6. S5: Optical image of 1 nm (2-3 layers) GeH on SiO_2.

Photocurrent of 1 nm (2-3 layers) GeH under 200 □W laser illumination (633 nm, ~3 mm diameter spot) and 15 V source-drain bias. The laser is modulated at 1 kHz and the photocurrent is measured by lock-in detection. The beam is blocked ("OFF") and unblocked ("ON") to show the photoconductive response.

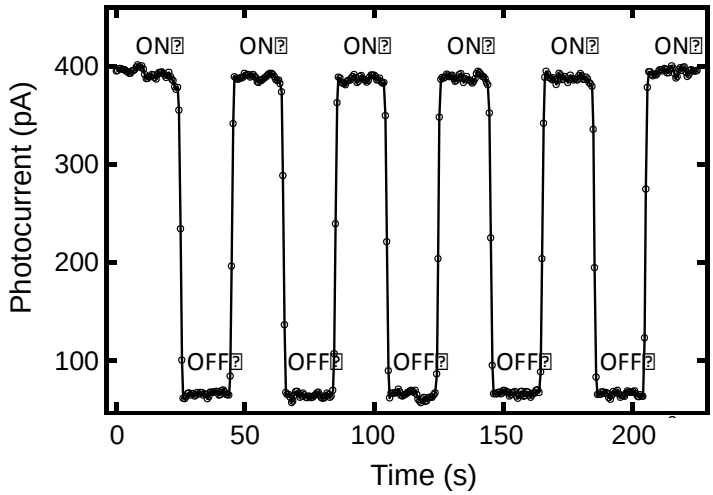

Supplementary Figure 6. S6: ON/OFF photocurrent of 1 nm (2-3) layers GeH

Fe Capping

In order to prevent oxidation of thin $CaGe_2$ films, we developed an Fe capping layer to protect the films during exposure to air. We deposit 5 nm of Ca prior to depositing the Fe cap to avoid Fe interacting directly with the Ge. To test how efficiently the Fe dissolves in HCl, we grew 5 nm Ca followed by 20 nm Fe at room temperature immediately after the growth of a $CaGe_2$ film. We then performed EDS at different beam energies of 2, 5, 10 and 20 kV corresponding to penetration depths of 25, 100, 340 and 1000 nm, respectively,

to determine the Fe concentration in the film. The EDS spectra and elemental analysis are listed below:

(a)

Element	App	Intensity	Weight%	Weight%	Atomic%
	Conc.	Corrn.		Sigma	
O K	28.76	5.3853	5.66	1.47	21.56
Fe L	-2.90	1.0631	-2.90	5.86	-3.16
Ge L	88.52	0.9653	97.23	5.71	81.60
Totals			100.00		

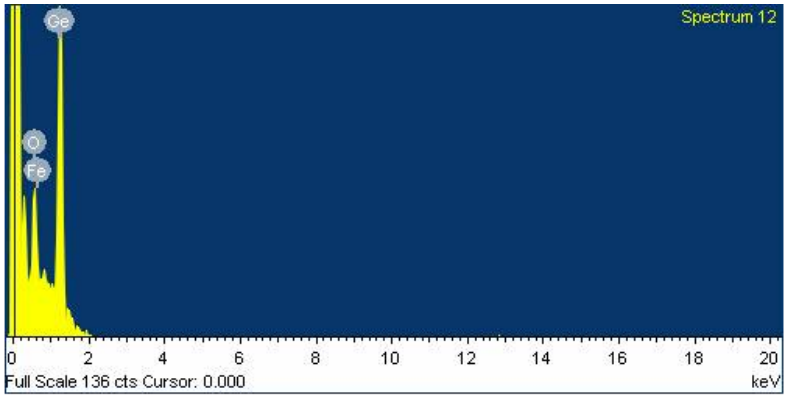

(b)

Element	App	Intensity	Weight%	Weight%	Atomic%
	Conc.	Corrn.		Sigma	
Cl K	6.58	1.1562	11.11	1.93	20.45
Fe L	-0.64	0.9989	-1.25	3.13	-1.47
Ge L	44.89	0.9729	90.14	3.38	81.01
Totals			100.00		

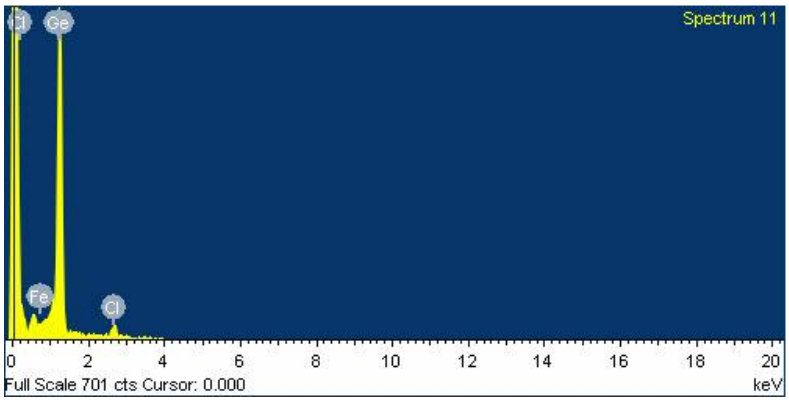

(c)

Element	App Conc.	Intensity Corrn.	Weight%	Weight% Sigma	Atomic%
Cl K	0.03	0.9757	7.34	0.91	13.98
Fe L	0.00	0.9135	-0.52	3.44	-0.63
Ge L	0.37	0.9808	93.18	3.31	86.66
Totals			100.00		

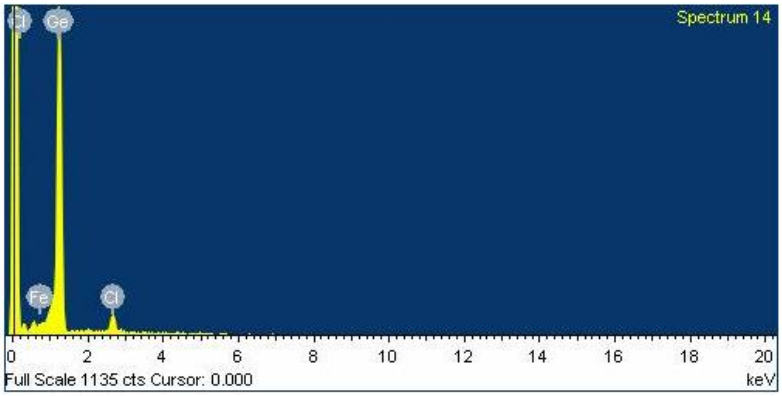

(d)

Element	App	Intensity	Weight%	Weight%	Atomic%
	Conc.	Corrn.		Sigma	
Cl K	1.13	0.6661	3.20	0.53	6.34
Fe K	-0.01	1.1801	-0.01	0.49	-0.01
Ge K	51.01	0.9934	96.81	0.71	93.67
Totals			100.00		

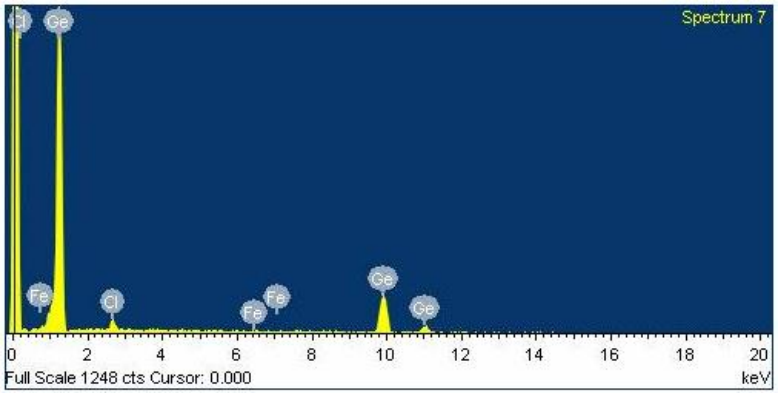

Supplementary Figure 6.S7: EDS of as-grown 150 nm (~260 layers) GeH at (a) 2 kV, (b) 5 kV, (c) 10 kV and (d) 20 kV

We did not observe (below detection limit) the presence of Fe residues on the deintercalated GeH sample for any of the beam energies. Furthermore, the EDS spectrum at 10 kV (Figure S7 c) of the Fe capped sample showed a significantly lower (below detection limit) oxygen composition as compared to the uncapped sample (Figure S2). The absence of oxygen for the 5, 10, and 20 kV scans along with the presence of oxygen in the 2 kV scan indicates a small amount of surface oxidation.

References

1. Novoselov K S, Geim A K, Morozov S V, Jiang D, Katsnelson M I, Grigorieva I V, Dubonos S V, Firsov A A 2005 Two-dimensional gas of massless Dirac fermions in graphene *Nature* **438** 197-200

2. Zhang Y, Tan Y W, Stormer H L, Kim P 2005 Experimental observation of the quantum Hall effect and Berry's phase in graphene *Nature* **438**

3. Du X, Skachko I, Duerr F, Luican A, Andrei E Y 2009 Fractional quantum Hall effect and insulating phase of Dirac electrons in graphene *Nature* **462** 192-195

4. Tombros N, Jozsa C, Popinciuc M, Jonkman H T, van Wees B J 2007 Electronic spin transport and spin precession in single graphene layers at room temperature *Nature* **448** 571-574

5. McCreary K M, Swartz A G, Han W, Fabian J, Kawakami R K 2012 Magnetic Moment Formation in Graphene Detected by Scattering of Pure Spin Currents *Physical Review Letters* **109** 186604

6. Mak K F, Lee C, Hone J, Shan J, Heinz T F 2010 Atomically Thin MoS_2: A New Direct-Gap Semiconductor *Physical Review Letters* **105** 136805

7. Radisavljevic B, Radenovic A, Brivio J, Giacometti V, Kis A 2011 Single-layer MoS_2 transistors *Nature Nanotechnology* **6** 147-150

8 Liu H, Neal A T, Zhu Z, Luo Z, Xu X, Tomanek D, Ye P D 2014 Phosphorene: An Unexplored 2D Semiconductor with a High Hole Mobility *ACS Nano* **8** 4033-4041

9. Bianco E, Butler S, Jiang S, Restrepo O D, Windl W, Goldberger J E 2013 Stability and Exfoliation of Germanane: A Germanium Graphane Analogue *ACS Nano* **7** 4414-4421

10. Jiang S, Bianco E, Goldberger J E 2014 The structure and amorphization of germanane *Journal of Materials Chemistry C* **2** 3185-3188

11. Restrepo O D, Krymowski K E, Goldberger J E, Windl W 2014 A first principles method to simulate electron mobilities in 2D materials *New Journal of Physics* **16** 105009

12 Xu Y, Yan B H, Zhang H J, Wang J, Xu G, Tang P Z, Duan W H, Zhang S C 2013 Large-Gap Quantum Spin Hall Insulators in Tin Films *Physical Review Letters* **111** 136804

13. Si C, Liu J W, Xu Y, Wu J, Gu B L, Duan W H 2014 Strain-induced quantum spin Hall effect in methyl-substituted germanane $GeCH_3$ *Scientific Reports* **4** 7297

14. Si C, Liu J W, Xu Y, Wu J, Gu B L, Duan W H 2014 Functionalized germanene as a prototype of large-gap two-dimensional topological insulators *Physical Review B* **89** 115429

15. Li L, Lu S Z, Pan J, Qin Z, Wang Y Q, Wang Y, Cao G Y, Du S, Gao H J 2014 Buckled Germanene Formation on Pt(111) *Advanced Materials* **26** 4820-4824

16. Davila M E, Xian L, Cahangirov S, Rubio A, Le Lay G 2014 Germanene: a novel two-dimensional germanium allotrope akin to graphene and silicene *New Journal of Physics* **16** 095002

17. Bampoulis P, Zhang L, Safaei A, van Gastel R, Poelsema B, Zandvliet H J W 2014 Germanene termination of Ge_2Pt crystals on Ge(110) *Journal of Physics: Condensed Matter* **26** 442001

18. Derivaz M, Dentel D, Stephan R, Hanf M C, Mehdaoui A, Sonnet P, Pirri C 2015 Continuous Germanene Layer on Au(111) *Nano Letters* **15** 2510-2516

19. Han W, Kawakami R K, Gmitra M, Fabian J 2014 Graphene Spintronics *Nature Nanotechnology* **9** 794-807

20. Meier F, Zachachrenya B P. *Optical Orientation, Modern Problems in Condensed Matter Science*. Vol. 8 (North-Holland, Amsterdam, 1984).

21. Pinchuk I V, Odenthal P M, Ahmed A S, Amamou W, Goldberger J E, Kawakami R K 2014 Epitaxial co-deposition growth of $CaGe_2$ films by molecular beam epitaxy for large area germanane *Journal of Materials Research* **29** 410-416

22. Vogg G, Brandt M S, Stutzmann M 2000 Polygermyne—A Prototype System for Layered Germanium Polymers *Advanced materials* **12** 1278-1281

23. Vogg G, Brandt M S, Stutzmann M, Genchev I, Bergmaier A, Gorgens L, Dollinger G 2000 Epitaxial $CaGe_2$ films on germanium *Journal of Crystal Growth* **212** 148-154

24. Li X, Cai W, An J, Kim S, Nah J, Yang D, Piner R, Velamakanni A, Jung I, Tutuc E, Banerjee S K, Colombo L, Ruoff R S 2009 Large-Area Synthesis of High-Quality and Uniform Graphene Films on Copper Foils *Science* **324** 1312-1314

25. Wang Y, Zheng Y, Xu X, Dubuisson E, Bao Q, Lu J, Loh K P 2011 Electrochemical Delamination of CVD-Grown Graphene Film: Toward the Recyclable Use of Copper Catalyst *Nature Nanotechnology* **5** 9927-9933

26. Gao L, Ren W, Xu H, Jin L, Wang Z, Ma T, Ma L P, Zhang Z, Fu Q, Peng L M, Bao X, Cheng H M 2012 Repeated growth and bubbling transfer of graphene with millimetre-size single-crystal grains using platinum *Nature Communications* **3** 699

27. Arguilla M Q, Jiang S, Chitara B, Goldberger J E 2014 Synthesis and Stability of Two-Dimensional Ge/Sn Graphane Alloys *Chemistry of Materials* **26** 6941-6946

28. Hajnal Z, Vogg G, Meyer L J P, Szucs B, Brandt M S, Frauenheim T 2001 Band structure and optical properties of germanium sheet polymers *Physical Review B* **64** 033311